Engineering Microfluidic Systems to Recapitulate Human Physiology

Ishahak, Matthew

UNIVERSITY OF MIAMI

ENGINEERING MICROFLUIDIC SYSTEMS TO RECAPITULATE HUMAN PHYSIOLOGY

By

Matthew Ishahak

A DISSERTATION

Submitted to the Faculty
of the University of Miami
in partial fulfillment of the requirements for
the degree of Doctor of Philosophy

Coral Gables, Florida

May 2020

UNIVERSITY OF MIAMI

A dissertation submitted in partial fulfillment of
the requirements for the degree of
Doctor of Philosophy

ENGINEERING MICROFLUIDIC SYSTEMS TO RECAPITULATE HUMAN PHYSIOLOGY

Matthew Ishahak

Approved:

_____ Ashutosh Agarwal, Ph.D. Assistant Professor of Biomedical Engineering	_____ Alice Tomei, Ph.D. Assistant Professor of Biomedical Engineering
_____ Suhrud Rajguru, Ph.D. Associate Professor of Biomedical Engineering	_____ Cherie Stabler, Ph.D. Professor of Biomedical Engineering
_____ Alessia Fornoni, M.D., Ph.D. Professor of Medicine	_____ Guillermo Prado, Ph.D. Dean of the Graduate School

ISHAHAK, MATTHEW (Ph.D., Biomedical Engineering)
Engineering Microfluidic Systems to Recapitulate Human Physiology (May 2020)

Abstract of a dissertation at the University of Miami.

Dissertation supervised by Professor Ashutosh Agarwal.
No. of pages in text. (138)

The overarching goal of this dissertation is to engineer cell culture platforms that recapitulate dynamic *in vivo* microenvironments and enable functional readouts that mimic organ-level physiology. Specifically, efforts were focused on developing novel dynamic cell culture devices, known as organs-on-chips, and integrated platforms to facilitate their use. Despite the potential of organs-on-chips to address challenging problems in biomedical research, the high technical skill required to fabricate and operate these devices has hindered their widespread adoption. An iterative design, build, test methodology was applied to the research and development of microfluidic devices and automated platforms. The dynamics of glucose stimulated insulin secretion function of pancreatic islets informed the initial design of the microfluidic device for organoids. A microfluidic device to recreate biologic barrier functions was originally inspired by the pressure driven filtration that occurs within the kidney glomeruli. These devices were built through subtractive rapid prototyping of noncytotoxic plastic. Human cells were incorporated into the devices. Microfluidic pumps were utilized to generate dynamic flow. The organs-on-chips were then tested to validate cell viability under dynamic culture conditions and the ability to model organ-level functional readouts. Finally, an integrated platform was developed to automate dynamic culture and functional assessments. Together, this research demonstrates that dynamic physiological processes can be modeled *in vitro* through the development organ-on-chip technology.

ACKNOWLEDGMENTS

First and foremost, I want to thank my mentor, Dr. Ashutosh Agarwal, who has had a significant impact on my personal and professional development. Directly and indirectly, his candor and intelligence has guided me throughout my scientific endeavors. I would also like to thank Dr. Alessia Fornoni and her lab members for their help in expanding my scientific horizons. Furthermore, I would like to express my sincere gratitude to Dr. Cherie Stabler, who has been a significant influence on my academic and scientific development since I was an undergraduate student. Additionally, I would like to thank Drs. Alice Tomei and Suhrud Rajguru for their commitment to my research throughout my undergraduate and graduate studies.

Next, I would like to thank the current and past members of the Physiomimetic Microsystems Laboratory. Specifically, I would like to thank Sid Rawal, Giovanni Lenguito, Ahmad Alassaf, Rachel Besser, Vera Mayo, and Dennis McDuffie all of whom have contributed significantly to my research and personal development throughout my PhD. I would also like to thank the undergraduate students who I have mentored and have helpws contribute to my various projects: Ellery Jones, Roger Charles, Isa Claure, Danny Carbonero, Jordan Hill, Qurat Amin, Adiel Hernandez, Carlos Aguila, Ismael Ortiz, Laura Wubker, and Liev Birman. I am also thankful to the University of Miami College of Engineering for providing an environment for me to pursue my research. Specifically, I would like to thank the BME department including the chair, Dr. Fabrice Manns, and the administrative team.

Additionally, I want to give a special thanks to the various people with whom I've developed collaborative relationships. Specifically, Smit Patel from the Stabler Lab at the

University of Florida, Heather Nelson and Jack Walker from the Powers and Brissova Group at Vanderbilt University, and the members of the Humphreys Lab at Washington University in St. Louis.

I would also like the acknowledge my family who has always been there for me with love and support. I would especially like to thank my mother and father whose sacrifices made all this possible. I would also like to thank Erin Purdy for her patience, support, and love which has made this process easier.

Lastly, I would like to thank the various funding agencies that have supported my work. The work relating to the islet microfluidic device was funded by the NIH NIDDK Human Islet Research Network (U01DK104162 and UC4DK104208). The glomerulus work was funded by a Ruth L. Kirschstein Predoctoral Individual National Research Service Award by the NIH NIDDK (F31DK118860). Platform development was supported by funding from the Wallace H. Coulter Foundation. Additional support was provided the John T. Macdonald Foundation and Mallinckrodt. I would also like to acknowledge the families of those who donated organs for this study.

TABLE OF CONTENTS

Page

LIST OF FIGURES

LIST OF TABLES

CHAPTER 1

Introduction and Rationale

1.1 Introduction

Scientific discovery is reliant on the tools available to answer questions posed by curious minds. The invention of the telescope and subsequent improvements made by Galileo, Kepler, and Newton opened the cosmos for observation. Optical tools allowed scientists to not only explore the vast universe, but also to closely examine the world around us. Around the same time Newton was observing celestial bodies with his improved telescope, Robert Hooke had modified existing microscopes to magnify objects up to 50 times. In 1665, Hooke published *Micrographia* in which he described the smallest unit of living organisms, the cell (*1*). This discovery opened the door to a whole new world of scientific questions and discoveries which would become the foundations of biomedical research.

Since Hooke's first observation of cells, scientific tools have been rapidly advancing and enabling a deeper understanding of how living things function. As new knowledge was acquired, it was applied to the field of medicine to combat diseases and improve human health. Biomedical research has led to discoveries that have eradicated diseases, such as smallpox, and improved the prognosis of patients with deadly diseases, such as cancer. Advancements in biomedical research are due, in no small part, to the innovative tools developed and used in laboratories. As Thomas Kuhn described, "research…owes its success to the ability of scientists regularly to select problems that can be solved with conceptual and instrumental techniques close to those already in existence" (*2*). Despite the advances in modern medicine, there will always be a need to improve the "conceptual and instrumental techniques" employed in biomedical research.

For much of the last century, *in vitro* cell culture has been performed in static, two-dimensional (2D) systems. Despite the numerous biomedical discoveries made using these systems, they are unable to faithfully model the complex physiological and pathophysiological responses that occur in humans. As a result, it has become increasingly difficult to translate basic science discoveries into safe and effective treatments. From 1963 to 2008, expenditures on research and development (R&D) of new pharmaceutical therapies grew exponentially, while the number of new drugs approved remained relatively stagnant (*3*). This has led to a steady decline in the number of drugs approved per billion US dollars spent in R&D (*4*). The increasing cost of pharmaceutical R&D has gone hand in hand with a rise in the cost of healthcare, especially in the United States. This highlights the need for new tools to not only reduce the cost of pharmaceutical drug development, but also improve the efficiency of the development process. To solve the current problems facing biomedical science, emerging approaches and technologies from interdisciplinary fields must be adopted.

The overarching goal of this dissertation is to engineer cell culture platforms that recapitulate dynamic *in vivo* microenvironments and enable functional readouts that mimic organ-level physiology. Specifically, efforts were focused on developing novel dynamic cell culture devices, known as organs-on-chips, and integrated platforms to facilitate their use. Organs-on-chips utilize microfabrication and microfluidics to recreate the minimal functional unit of human organs (*5*). Despite the potential of organs-on-chips address challenging problems in biomedical research, the high technical skill required to fabricate and operate these devices has hindered their widespread adoption. Therefore, there is a need to develop methods and platforms that make organs-on-chips easier to use.

An iterative design, build, test methodology was applied to the research and development of devices and platforms for the purpose of improving organ-on-chip technology. The design of microfluidic devices was inspired by the dynamic physiological processes that occur at the minimal functional unit of an organs of interest. The dynamics of glucose stimulated insulin secretion function of pancreatic islets informed the initial design of the microfluidic device for organoids. A microfluidic device to recreate biologic barrier functions was originally inspired by the pressure driven filtration that occurs within the kidney glomeruli. These devices were built through the subtractive rapid prototyping of bioinert plastic. Human cells, from immortalized lines or isolated from cadaveric donors, were incorporated into the devices. Microfluidic pumps were utilized to generate dynamic culture conditions. The organs-on-chips were then tested to validate cell viability under dynamic conditions and the ability to model organ-level functional readouts. Finally, an integrated platform was developed to automate dynamic culture and functional assessments. Together, this research demonstrates that organ-on-chip technology can not only model dynamic physiological processes *in vitro*, but also be translated to the broader biomedical research community to facilitate novel discoveries.

1.2 Rationale

This dissertation consists five distinct engineering challenges and applications presented in CHAPTERS 3-7. Some of the content in these chapters represents a modified version of a published article or work included in articles submitted for publication. Each chapter contains a brief overview, methods, results, and a discussion. CHAPTER 2 highlights the current roadblocks and limitations of microfluidic organs-on-chips that we will aim to address throughout this dissertation.

To engineer microfluidic devices to model human physiology, an interdisciplinary set of design specifications had to be developed. Throughout the design, build, test process, design specifications were continuously modified to either model specific *in vivo* physiology or incorporate assays to answer specific scientific questions. Despite the constant alterations in the design specifications, subtractive rapid prototyping facilitated efficient fabrication of the various design iterations. The development of novel organ-on-chip devices in the Physiomimetic Microsystems Laboratory began with the development of fluidic platform for the interrogation of pancreatic islets (*6*). CHAPTER 3 discusses the characterization of the fluid shear stress as function of flow rate within this fluidic platform and how understanding of the fluid dynamics can be applied to improve the vascularization and maturation of kidney organoids, which were cultured and assessed in the Humphreys Lab at Washington University in St. Louis.

The design was further optimized through computational modeling of fluid dynamics and islet physiology (*7-11*). CHAPTER 4 discusses the process of optimizing the microfluidic platform for high resolution imaging to elucidate intra-islet signaling in a pseudoislet system. Portions of this work was produced in collaboration with the Powers and Brissova Group at Vanderbilt University.

In CHAPTER 5, we address the challenge of maintaining islets *in vitro* during continuous perifusion culture through the addition of oxygen permeability, in collaboration with Smit Patel from the Stabler Lab at the University of Florida. Isolated pancreatic islets have a limited *in vitro* lifespan due to a decline in cell viability and function over time (*12*). Therefore, we provide an approach to evaluate the function of primary islets over time within our platform.

The design and fabrication of a microfluidic device to recreate biologic barrier is described in CHAPTER 6. One of the proposed advantages of organ-on-chip technology is the ability to reverse engineer the systemic pathophysiology *in vitro* by linking multiple organ-on-chip devices (*13*). However, multiple organs-on-chips must be developed and validated before this can be achieved. The disease most associated with pancreatic islets is diabetes. While the primary symptom of diabetes is the inability to maintain glucose homeostasis, diabetic patients often experience several secondary symptoms. Diabetic nephropathy affects up to 40% of people with diabetes and is one of primary causes of end-stage renal failure (*14*). The clinical hallmark of diabetic nephropathy is albuminuria, which is caused by dysfunction at the glomerular filtration barrier (*15*). Therefore, to build on the results of the previous chapters, the focus of this dissertation shifts to the development and assessment of a microfluidic device to recapitulate the function of the glomerular filtration barrier. The primary role of the glomerulus is to filter waste from the blood for excretion through the urine. This is achieved through hydrostatic and oncotic pressure gradients maintained by the glomerular filtration barrier, which is comprised of endothelial cells, a basement membrane, and specialized epithelial cells, podocytes.

The final topic of this dissertation is the development of an integrated platform for operating and interrogating organs-on-chips. As a relatively new technology, the fabrication and operation of organs-on-chips require a specialized set of skills and equipment. CHAPTER 7 discusses the integration of microfluidic control and sample collection within a single user interface to facilitate cell culture and assessment on organ-on-chip devices.

The implications of the organ-on-chip platforms described in this dissertation and their applications in future research are discussed in CHAPTER 8. Specifically, the steps required for commercialization of organs-on-chips and potential studies incorporating emerging cellular technologies, such as CRISPR and stem cell-derived organoids, are described.

CHAPTER 2

Roadblocks Confronting Widespread Dissemination of Organs-on-Chips

2.1 Overview

Organ-on-chip platforms hold significant promise as alternatives to traditional animal models or cell cultures, both of which poorly recapitulate human pathophysiology and human level responses. This decade has witnessed seminal scientific developments from academic laboratories, a flurry of startups that seek to translate those platforms, and a genuine interest from pharmaceutical industry as well as regulatory authorities to develop this technology. The individual and collaborative efforts of these important stakeholders will undoubtedly continue to refine and mature organ-on-chip platforms. It is imperative, therefore, to identify any fundamental design features that might ultimately prevent widespread dissemination and deployment of these systems. Here, we examine several such design barriers. First, we highlight the complications associated with polydimethylsiloxane (PDMS), the most commonly used material for organ-on-chip fabrication. Second, we discuss the lack of real-time bioanalytical assays that can be integrated within these typically low-volume devices. Finally, we describe the engineering challenges in operating these devices as they relate to fluid handling, temperature control, and maintenance of bubble-free and sterile conditions. We submit that rectification of those barriers is especially timely, as these technologies are beginning to be tested and validated by the intended end-users: pharmaceutical industry, regulatory authorities, and disease biologists.

2.2 The Translational Landscape of Organ-on-Chip Technology

Over the last decade, organ-on-chip technology has been one of the fast-growing areas in biotechnology. The foundation of organs-on-chips can be attributed the convergence of advances in the areas of microfluidics and tissue engineering. However, the major driving force has been the interest of pharmaceutical companies to apply this technology to drug development. The landscape for new drug development is one of the most daunting of any product development pipeline. The estimated cost for pharmaceutical companies to bring a new drug to market is approximately 2 billion dollars and the process can take upwards of 15 years (*16, 17*). Despite this huge investment of time and money, the clinical success rate is just under 14% (*18*). This problem, however, is not new. The high attrition rate and overall decline in pharmaceutical research and development efficiency has been well document for over 30 years (*4, 19-22*). A recurring culprit has been animal models, which are not sufficiently predictive of the safety nor efficacy of therapeutic compounds (*23, 24*).

As a result, an abundance of new biotechnology companies has emerged to help move organs-on-chips out of academic research labs and into the drug discovery space. In the US, startup companies have been spun out of academic institutions primarily focused on providing research services that utilize unique organ-on-chip models. In Europe, the expansion of organ-on-chip technology is being driven by microfluidic companies looking to add organ-on-chip applications to their portfolio. The value proposition for many of these startups focuses on providing better data for lead optimization. However, the regulatory impact of utilizing organs-on-chips for pre-clinical studies remains unclear. The United States Food and Drug Administration (FDA), Center for Drug Evaluation and

Research currently requires data from animal studies, such as safe starting doses and potential toxicity levels, to ensure that human clinical trials can be safely conducted. An alternative model, such as an organ-on-chip would need to provide this information as well as genetic toxicity, pharmacokinetics, ADME (absorption, distribution, metabolism, and excretion), reproductive toxicity, and carcinogenicity. By targeting large pharmaceutical companies without significant validation, current organ-on-chip companies are in a precarious position where they must prove the utility of their platform or risk being considered nonviable by pharmaceutical companies and regulatory agencies.

An alternative end-user for organ-on-chip technology is the biomedical researcher without traditional engineering skills or microfluidics experience. The needs for these users vary greatly from pharmaceutical end-users. Where pharmaceutical companies value high-throughput, highly reproducible data from organs-on-chips, the research end-user values the ability to gather data previously unattainable. Additionally, the high level of automated demanded for drug development necessitates easy-to-use, less complex microfluidic platforms. In a research setting, system complexity is less of a concern, if the system is operable after some training. Ultimately, innovation is the most valuable outcome that can arise from providing organs-on-chips to the researchers. The research questions pursued within academia may not always be the most clinically relevant (or profitable), but the demands of novel research can help push organ-on-chip technology to its full potential.

2.3 PDMS Alternatives for Organs-on-Chips

2.3.1 History and limitations of PDMS for organs-on-chips

The generation of PDMS-based microfluidic devices was pioneered by the Whitesides Research Group at Harvard University (*25, 26*). Their approach utilized a

combination of photolithography and soft lithography to generate enclosed microfluidic channels using polydimethylsiloxane (PDMS). Just over a decade later, this method was adapted to develop one of the first organs-on-chips, a lung-on-chip, published by researchers at the Wyss Institute for Biologically Inspired Engineering at Harvard University (*27*).

The first step of the fabrication of PDMS-based organs-on-chips begins with photolithography to generate a master mold of a microscale 3D pattern. Briefly, an SU-8 silicon master is fabricated by pouring SU-8 2100 photoresist on a clean silicon wafer. Next, the wafer is covered with a photomask and exposed to UV light to crosslink the SU-8. The wafer is then placed in a developer solution to fully cure the crosslinked SU-8. The result is hardened microscale features patterned on the silicon wafer.

Next, the microscale channels for fluidics and cell culture can be generated using soft lithography. Briefly, the previously fabricated master silicon wafer is attached to the bottom a petri dish using double sided tape. Then a PDMS mixture is poured onto the master. The PDMS is cured at 60°C then cut away from the silicon wafer. In the method originally described by the Whitesides group, the PDMS replica is bonded to a flat slab of PDMS. However, for organs-on-chips, different geometries of microfluidic channels or porous structures can be layered to create more complex devices. Plasma bonding is one of the commonly used methods for bonding PDMS.

PDMS has become the material of choice for organs-on-chips due properties that make it suitable for biological applications, such as low cytotoxicity, optical transparency, gas permeability, and established fabrication methods (*28*). Despite the adoption of PDMS as the standard material for organs-on-chips, many limitations have been described (*29,*

30). Of these drawbacks, the adsorption of hydrophobic compounds and leaching of uncrosslinked oligomers have provided the greatest hinderance to the adoption of PDMS-based organs-on-chips for drug discovery assays. Additionally, the channels in PDMS-based microfluidic devices have a maximum height of approximately 200 µm, due to the limitations of the photolithographic fabrication method (*31*). As a result, there is a need to develop organs-on-chips from alternative materials.

2.3.2 Subtractive rapid prototyping of organs-on-chips

Due to the long history of microfluidic technology, there is extensive literature on the fabrication and use of plastic microfluidic devices, which may serve as an alternative to PDMS for organs-on-chips (*32, 33*). In this dissertation, subtractive rapid prototyping is the primary method for fabrication of microfluidic devices. Subtractive rapid prototyping relies on the removal of features to generate microscale features; in contrast to additive fabrication methods, such as 3D printing where material is deposited. Specifically, micromilling is utilized to fabricate microfluidic devices from bioinert plastic (*34*).

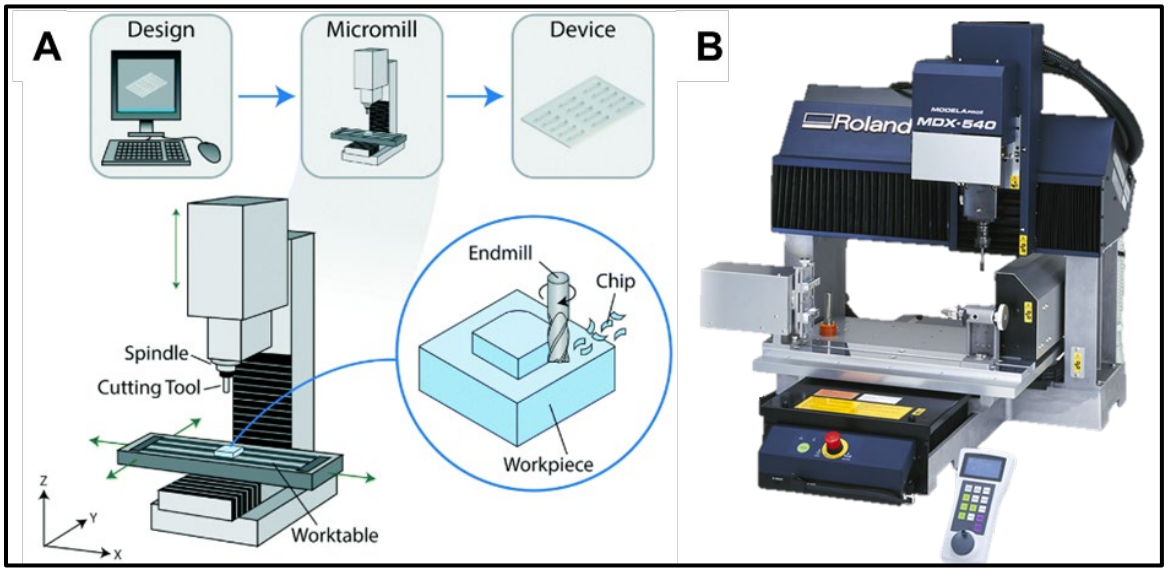

Figure 2.1 (A) Schematic of the basic components of a CNC mill, which can use computer-aided design (CAD) models to produce finished devices (*Adapted from 34*) (B) Roland MDX-540 milling machine with rotary axis used in the Physiomimetic Microsystems Laboratory

Milling machines consist of three main components: 1) a worktable, 2) a cutting tool, and 3) a spindle (Figure 2.1A). The worktable is set on a high-precision XY-stage that allows the workpiece to be positioned. The cutting tool, most commonly an endmill, is rotated at high speeds by the spindle and shaves away material from the workpiece. The spindle housing is adjustable in the z-direction. The milling machine used throughout this work, the MDX-540, can be equipped with a rotary axis, enabling 4-axis milling (Figure 2.1B). The MDX-540, along with many modern milling machines, employ computer numerical control (CNC). This automated method, which replaces manual control of the worktable and spindle, greatly increases the precision and accuracy of the milling process. Appendix A1 outlines the setup protocol implemented in the Physiomimetic Microsystems Laboratory for precision within 100 μm. Additionally, 3D computer-aided design (CAD) models can be directly converted to the CNC milling commands using software developed by the Roland Corporation. In comparison to other fabrication methods for plastics, CNC milling provides numerous advantages for in-house prototyping (Figure 2.2).

Plastic microfluidic devices, fabricated through subtractive rapid prototyping, hold potential to be a viable alternative to PDMS for organs-on-chips. However, significant engineering is needed to develop complete microfluidic systems that are applicable to a wide range of biologic experiments. To this end, this dissertation is focused not only on the design and fabrication of PDMS-free microfluidic devices, but also on the development and optimization of platforms that enable novel experiments. A vital component of this approach is the translation of devices and methodologies to external laboratories, especially labs without significant prior experience with microfluidics.

A. Technical Capabilities

Categories	Milling	Embossing	Stereolithography	Injection Molding
Material Capabilities				
Thermoplastics	●●●	●●●	●●○*	●●●
Thermosets	●●○*	●●○*	●●○*	●●●
Elastomers	●○○	●●○†	●●○*	●●●
Metals	●●●	●○○‡	●○○†	●○○*
Glass/Ceramics	●○○†	●○○§	●○○†	○○○*
Wax	●●●	●●●	○○○	●●●
Feature Capabilities				
Additional Heights	No added complexity	Additional layer per height	No added complexity	No added complexity
Aspect Ratio	8:1	2:1	Method-dependent	8:1
Contoured 3D Features	Continuous	Layered	Layered	Continuous
Sharp Corners	External Only	Internal / External	Internal / External	Internal / External
Undercuts	Special tooling	Impractical	Yes	Special tooling
Results				
Surface Roughness	0.4 - 2 µm	Replicates mold roughness	0.4 - 6 µm	Replicates mold roughness
Autofluorescence	Not affected	Increased by processing	Material-dependent	Not affected
Legend	* *Only cured thermosets* † *Poor consistency and characterization*	* *Only uncured thermosets* † *Only thermoplastic elastomers* ‡ *Limited to specific features and thin sheets* § *Layered mix with polymer*	* *Uses resins that, when cured, have similar properties to desired polymer* † *Requires polymer/wax additive*	* *Requires polymer/wax additive*

●●● Excellent
●●○ Most conditions
●○○ Specific conditions
○○○ Impractical

B. Cost Comparison

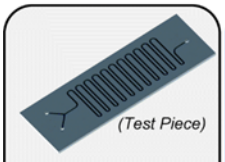

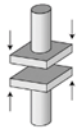

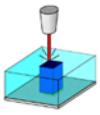

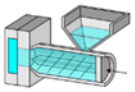

	Milling				Embossing		Stereolithography		Injection Molding	
Setup Costs	*(On-site)*		*(Outsourced)*		*(On-site)*		*(Outsourced)*		*(Outsourced)*	
Equipment	$15k <		*N/A*		$15k <		*N/A*		*N/A*	
Tooling / Supplies	$500		*N/A*		$50		*N/A*		*N/A*	
Process Times and Costs										
Outsourced Expenses	Time	Cost	Time	Cost	Time	Cost	Time	Cost	Time	Cost
Mold / Tooling	*N/A*	*N/A*	*N/A*	*N/A*	4 - 15 d	$ 55 - 321	*N/A*	*N/A*	*N/A*	$ 2255
Device Fabrication	*N/A*	*N/A*	11 - 15 d	$ 137	*N/A*	*N/A*	4 - 6 d	$ 33	11 - 15 d	$ 2
On-site Expenses										
Machine Setup	10 m	*N/A*	*N/A*	*N/A*	5 m	*N/A*	*N/A*	*N/A*	*N/A*	*N/A*
Material Setup	< 5 m	$ 1	*N/A*	*N/A*	< 5 m	$ 1	*N/A*	*N/A*	*N/A*	*N/A*
Device Fabrication	10 m	*N/A*	*N/A*	*N/A*	30 m	*N/A*	*N/A*	*N/A*	*N/A*	*N/A*
Subtotal:	25 m	$ 1	*N/A*	*N/A*	40 m	$ 1	*N/A*	*N/A*	*N/A*	*N/A*
Expenses (per device)										
1 Devices	< 1 h	$ 1	11 - 15 d	$ 137	4 - 15 d	$ 56 - 322	4 - 6 d	$ 33	11 - 15 d	$ 2257
25 Devices	1 d	$ 1	11 - 15 d	$ 137	6 - 17 d	$ 3 - 14	4 - 6 d	$ 33	11 - 15 d	$ 92
50 Devices	3 d	$ 1	11 - 15 d	$ 137	8 - 19 d	$ 2 - 7	4 - 6 d	$ 33	11 - 15 d	$ 47

Figure 2.2 Comparison between micromilling and other fabrication methods in terms of: (A) Technical capabilities and (B) Cost (*Adapted from 34*).

2.4 Platform Development for Organ-on-Chip Operation

2.4.1 Expanding design criteria beyond the chip

In this section, we discuss the other necessary components for a complete organ-on-chip platform. In the organ-on-chip community, platform almost exclusively refers to the microfluidic chip that houses the cellular components. For example, a novel chip design

that allows for a unique arrangement of cells is often described as some type of organ-on-chip. Ultimately, bioengineers are utilizing the technology of microfluidics to expand the ways we culture cells. This approach is derivative of the tissue engineering mindset when it comes to developing organs on chip, where the focus is on recapitulating the minimal functional unit of an *in vivo* organ. With this "reverse engineering" design approach, potential end-user needs are often overlooked in the design process. Instead the design is based on observable biologic features, such as cell types, biophysical forces, and a target endpoint, for example demonstrating drug toxicity or recreating a dynamic biological process. This view dramatically oversimplifies the design requirements and fails to consider the mechanical components that are needed for a complete organ-on-chip platform.

From a broader perspective, a complete organ-on-chip system requires additional components, such as electronic components and interface software. Without the development of complete platforms, organ-on-chip technology will fall into the "valley of death" that plagues healthcare innovation (*35*). Therefore, a Systems Engineering approach is necessary to design and manage the various components required for an organ-on-chip platform. Specifically, the application of a bio-mechatronic design methodology can lead to the development of practical organ-on-chip platforms.

2.4.2 Bio-mechatronic design methodology

The biomechatronic design methodology is an alternative approach for the design and development of organ-on-chip platforms which comes from a device engineering viewpoint with the addition of biologic considerations. The idea stems from the mechatronic design theory and focuses on product development with a significant

consideration of the functions of the end-product. Mechatronic design is defined as the integrated design of a mechanical system and its embedded control system (*36*). In today's world this often means a multidisciplinary approach that combines mechanical electrical, and computer engineering. As a result, higher-level systems engineering is also required to manage the complex devices being developed. Biomechatronic design builds upon this multidisciplinary approach by adding in the unique considerations of developing living biologic systems. By now it should seem obvious that engineering organs-on-chips requires a multidisciplinary team. However, organ-on-chip technology as we understand it is barely a decade old. In the current adolescence of organs-on-chips we are starting to see the development of more complete platforms. Early organ-on-chip startup companies, like Emulate and Nortis, have spent a considerable amount of time and money developing these platforms, which are only just becoming commercially available.

Bio-mechatronic design, which is based on the mechatronic design used by mechanical and electrical engineers, uses an iterative working procedure based on charts and tables to structure the design process of complex systems that include biologic components (*37*). The first step of the process is to define the goal and constraints of the design. For an organ-on-chip platform this means defining the organ(s) that will be modeled and essential functional readouts. Since no *in vitro* system can be a perfect model

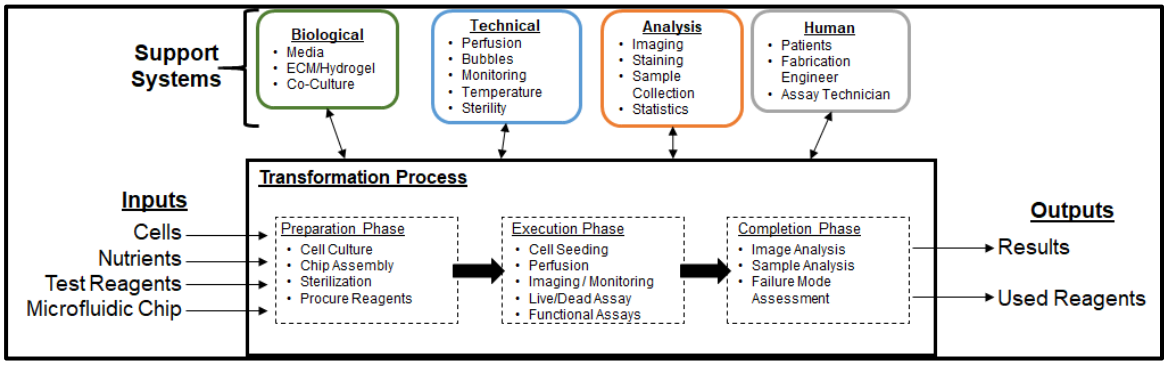

Figure 2.3 Simplified Hubka-Eder map depicting the inputs, transformation process, support systems, and outputs of an organ-on-chip platform (*Adapted from 37*).

of *in vivo* phenomenon, constraints must also be defined to ensure a feasible design is developed. Next, user needs and target specifications for the components of the system must be defined as quantitative or qualitative values. These needs and specifications should cover as many components of the system as possible, including cell source, microenvironmental features, microfluidic hardware, compatible assays, cost, etc.

Based on the user needs and design constraints, the workflow, or transformation process, from input to output of the system can be mapped (Figure 2.3). Before fabricating and assembling the system, basic functional elements will be conceptualized and arranged to develop the platform configuration. Next, functional elements are identified and grouped to determine the most vital components of the platform. Organization elements at this stage can help identify key features of the design and decrease time required address potential failure modes. Overall, careful planning and understanding of the processes involved in operation of organs-on-chips is vital for the development of useful devices and systems.

2.5 Outlook

The rapid development of organs-on-chips, primarily driven by interested from pharmaceutical companies, as led to a need for industry standards for the field. However, standardization cannot stifle innovation. Properly addressing the translational barriers for various applications is key for organs-on-chips to reach their ultimate potential. While the resolution of these barriers should diminish the trepidation of slow adopters, dialogue with industry partners will help in defining important milestones such as throughput, cost per data point, and demonstration of value proposition in terms of cost and time savings. However, significant care should be taken to avoid narrowing the scope of organ-on-chip

technology solely to drug discovery and high-throughput applications desired by pharmaceutical companies.

Organ-on-chip technology still holds a lot of promise as a tool to elucidate complex biologic and pathophysiological process. As a result, there is a need to develop microfluidic devices and platforms that meet the needs of academic researchers. Therefore, the main application of the microfluidic platforms described throughout this dissertation represent the translation of organ-on-chip technology to novel research applications. By focusing on more basic science applications for organs-on-chips, the goal is to demonstrate that organs-on-chips can be implemented at multiple stages of drug discovery and development. A recognition that this highly interdisciplinary effort is not only scientifically fertile, but also ushering in a new framework for scientific endeavor where engineers, scientists, industry, funding agencies, investors, and regulatory bodies are all contributing in the development of these high-impact systems.

CHAPTER 3

Characterization of Fluid Shear Stress and its Effect on Kidney Organoids

3.1 Overview

Pluripotent stem cells and isolated organ progenitor cells can develop into complex, multicellular constructs resembling whole organs, called organoids. Organoids have the potential to recapitulate human organogenesis, model complex pathophysiology, and assess the efficacy of novel drugs. Formation of organoids relies heavily on the self-organization of cells into complex structures with the help of growth factors and hydrogels to promote differentiation. However, in a static culture conditions, development of vasculature can be stunted, resulting in immature organoids. Recently, it has been shown that high shear stress can improve vascularization and maturation of kidney organoids, established by the Humphreys Lab at Washington University. Previously, our group has developed a PDMS-free organ-on-chip platform to interrogate pancreatic islets. In this study shear stress within our organ-on-chip platform is characterized as a function of flow rate. Ultimately, developing organoids under optimized shear stress conditions may enable new *in vitro* applications.

3.2 Materials and Methods

3.2.1 Microfluidic device design and fabrication

The microfluidic device is based on a previously published fluidic platform, with minor modifications (*6*). Briefly, three-dimensional computer-aided designs were developed using SolidWorks 2018 (Dassault Systèmes). Microfluidic devices were machined, according to the specifications of the CAD models, from poly(methyl methacrylate) workpieces using a computer numerical controlled milling machine (MDX-

540, Roland). A CO_2 laser machine (Legend Helix, Epilog Laser) was used to cut the final form factor of the microfluidic device from the workpiece. Fluidic connections were introduced to the microfluidic device using a commercially available microfluidic chip holder (Fluidic Connect PRO with 4515 Inserts, Micronit Microfluidics). Custom gaskets were fabricated using a two-part silicone epoxy (Duraseal 1533, Cotronics Corp) to ensure leak-free assembly. To minimize gasket failure and improve ease of operation, the gaskets were bonded into the top component of the microfluidic device using a specialized polyester adhesive (PS-1340, Polymer Science).

3.2.2 Confocal microparticle image velocimetry

Confocal microparticle image velocimetry (μPIV) was used to characterize the flow profile within the microfluidic device (Figure 3.1). Briefly, green fluorescent polystyrene beads with a 1 μm diameter (Fluoro-Max Dyed Green Aqueous Fluorescent Particles, ThermoFisher Scientific) were diluted in deionized water and perfused through the fluidic chip at 30 μL/min using a peristaltic pump (REGLO ICC Digital, Ismatec). Bead flow was

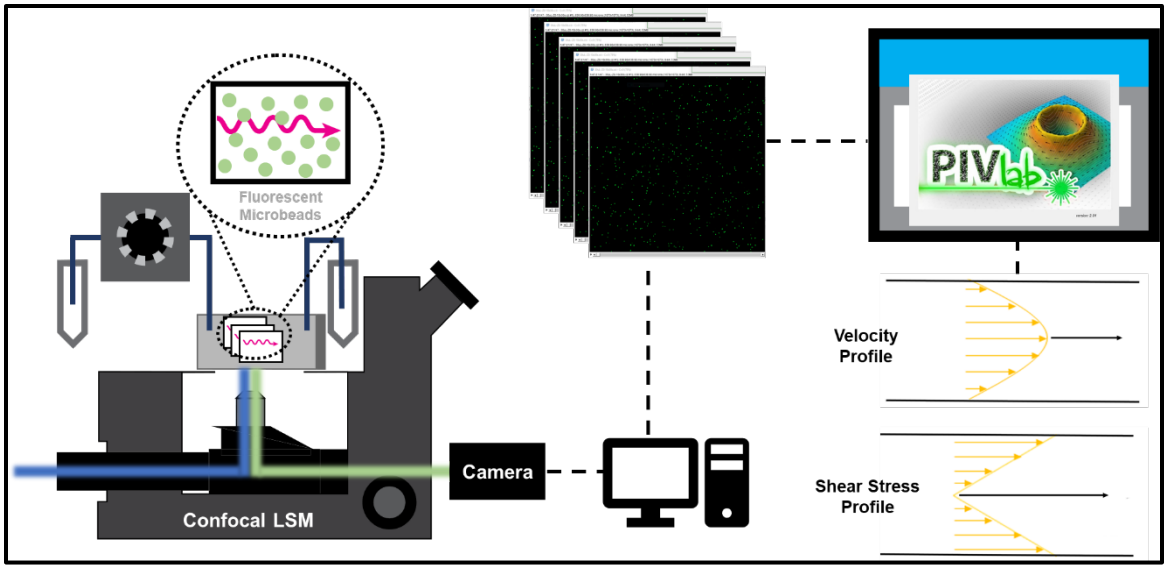

Figure 3.1 μPIV Workflow. The flow of fluorescent microbeads was observed using a confocal microscope. Video recordings of the flow was split into individual frames and processed in using the PIVLab add-on for MatLab. The resulting data was post processed to determine the velocity and shear stress profiles.

recorded for 30 seconds at multiple focal planes using a ZEISS LSM 800 laser-scanning confocal microscope at 10x magnification. Flow velocity was analyzed in MATLAB R2018a using the PIVLab add-on (*38*). A detailed protocol of the μPIV analysis process can be found in Appendix A2.

3.2.3 Computational fluid dynamics

Three-dimensional computational fluid dynamics simulations were performed in COMSOL Multiphysics Modeling Software (Release Version 5.0). Finite element method analysis was performed using the Single-Phase Laminar Flow module to determine the velocity profile within the microfluidic channel geometry. The module solved the Navier-Stokes equation for incompressible Newtonian flow of water with a no slip boundary condition at the walls. The 3D geometry of the microfluidic device was imported from SolidWorks and a physics-controlled mesh was implemented.

3.2.4 Culture and assessment of kidney organoids

Kidney organoids were generated from human pluripotent stem cells, following the Little Protocol (*39*). On Day 12 of the differentiation protocol, the kidney organoids were transferred to the microfluidic device and cultured under continuous perifusion. Immunofluorescent imaging was performed after 7 and 14 days to assess the formation of nephron tubules, podocytes, and vasculature. Maturation of kidney organoids was assessed by qPCR after 14 days of continuous perifusion. Culture and assessment of kidney organoids was performed in Dr. Benjamin Humphreys' Lab at Washington University in St. Louis by Kohei Uchimura.

3.3 Results

3.3.1 µPIV characterization of flow profile

Although microfluidic flow can be described theoretically using the Navier-Stokes equation, it is often useful to confirm these results empirically. µPIV is a measurement technique that utilizes flow tracing particles to measure fluid motion with a resolution ranging from 10^{-4} to 10^{-7} m (*40*). In general, fluid velocity can be determined by tracking a particle's motion across successive images with a known time delay. Confocal microscopy dramatically improves the resolution of imaging systems through the use of a pinhole to block light that is out of focus. The application of confocal microscopy to µPIV can enable true depth-wise resolved µPIV vector field mapping (*41*).

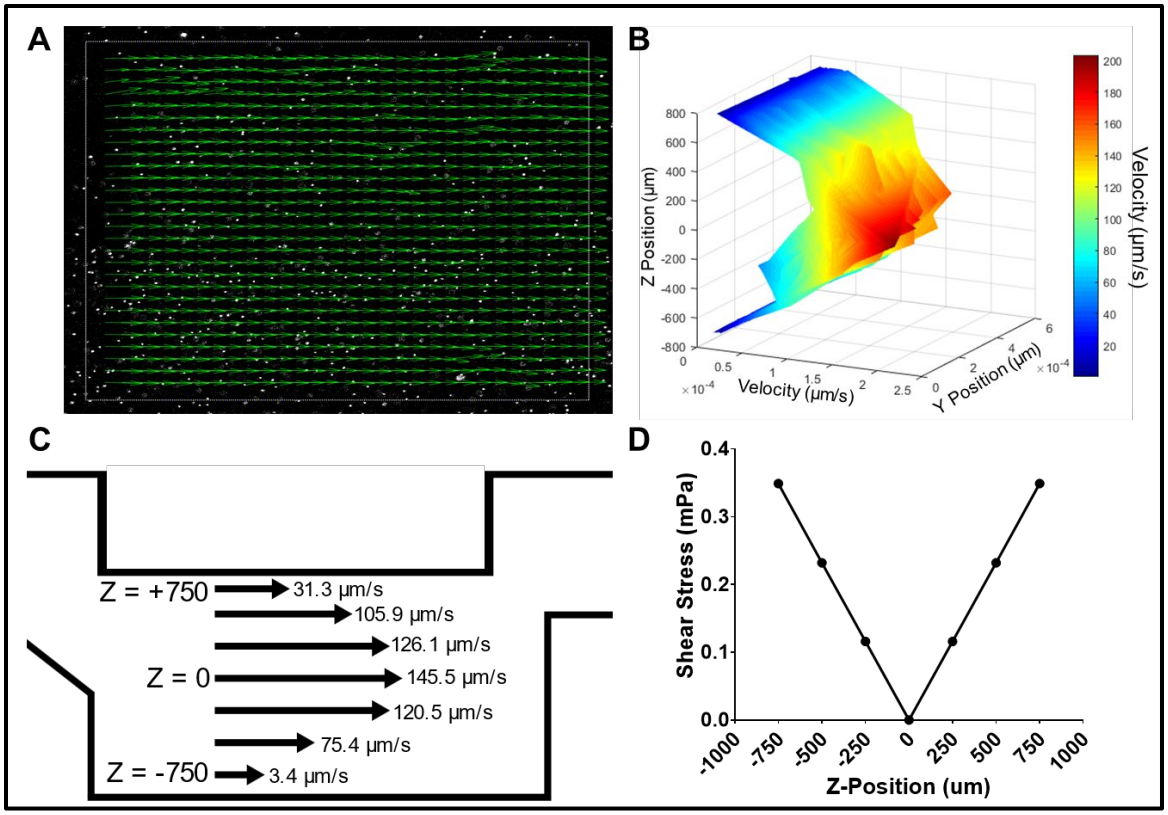

Figure 3.2 Flow profile in microfluidic device observed by µPIV. (A) Laminar flow profile visualized by streamlines generated from recording the flow of fluorescent beads by PIVLab. (B) Visualization of the parabolic flow profile using a 3D plot of the velocity calculated by PIVLab. (C) Average velocity measured at each focal plane further demonstrates the laminar parabolic flow profile.

Recording the flow of fluorescent particles at 30 µL/min revealed smooth streamlines, indicated a laminar flow profile (Figure 3.2A). Recording and analysis of the flow at focal planes ranging from the bottom to the top of the culture well further demonstrated a parabolic flow profile within the microfluidic device (Figure 3.2B-C). With the velocity profile characterized, the shear stress throughout the well could be calculated. Since parabolic flow was confirmed, the velocity profile can be written as:

$$\frac{V}{V_{max}} = 1 - \left(\frac{2z}{h}\right)^2$$

Where V is the velocity as a function of z, the position in the well, V_{max} is the maximum velocity, and h is 1.5mm to the total height of the culture well. According to Newton's law of viscosity, shear stress (τ) is given by:

$$\tau = \mu \frac{\partial V}{\partial z}$$

Where µ is the fluid viscosity and $\frac{\partial V}{\partial z}$ is the strain rate, in other words the derivative of velocity with respect to height. As expected, the fluid shear stress is greatest closes to the walls and zero at the center of the flow profile (Figure 3.2D).

3.3.2. Computational modeling of fluid shear stress

While confocal µPIV enables empirical characterization of the profile within the microfluidic device at a given flow rate, characterization of a range of flow rates can be very time consuming. Further, tracking particle flow at higher flow rates becomes very difficult due to the large distance the particles can travel between frames. Therefore, a 3D computational fluid dynamic model was developed to characterize the shear stress across a wide range of flow rates. This was achieved by importing the 3D geometry of the fluidic

channel of the microfluidic device into COMSOL (Figure 3.3A). A fine triangular mesh was implemented to define the finite elements for calculation (Figure 3.3B). With this mesh, comprised of 59224 elements and 531537 degrees of freedoms, the stationary solver was used to solve for the steady state velocity field. A parametric sweep was added to solve the velocity field as a function of different input flow rates. With these settings, the solution time was 421 seconds. A parabolic flow profile can be observed within the culture well, as shown in the resulting 3D velocity field plot solved for an inlet flow rate of 30 µL/min (Figure 3.3C). To compare the simulated velocity field to the µPIV results, a 3D cut line was placed at the center of the culture well geometry and the velocity along the line was plotted (Figure 3.3D). The computational model accurately described the scale and shape of the velocity profile.

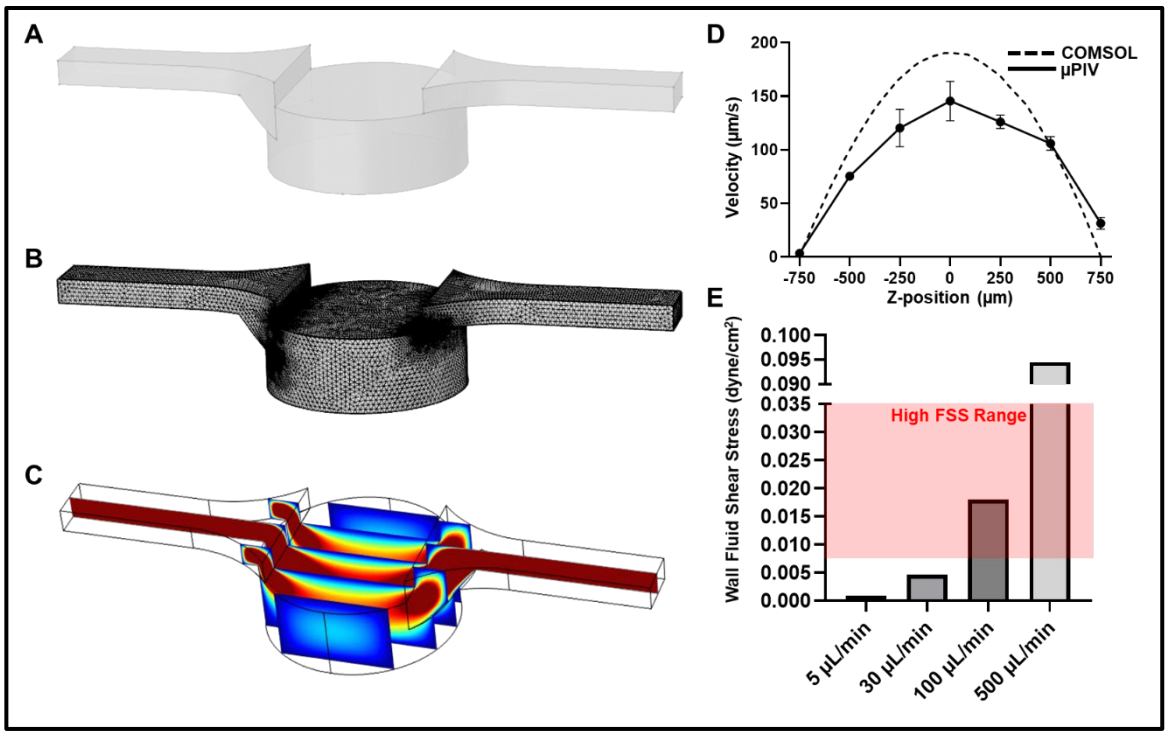

Figure 3.3 3D computational fluid dynamics modeling. (A) 3D geometry of the microfluidic channel imported into COMSOL from SolidWorks (B) Triangular mesh implemented to divide the geometry into finite elements for analysis. (C) Representative velocity profile at 30 µL/min obtained by the laminar flow module implemented in COMSOL.

The slight differences can be attributed to two factors. First, the computational model provides and idealized depiction of fluid flow. As a result, the velocity is slightly higher in the model due to the assumption of Newtonian flow and no slip boundary condition. Further, the velocity determined by μPIV is an average across a field of view at manually determined focal planes. Therefore, calculated velocity may be slightly lower due to the slower velocity of the parabolic flow profile at the edges of the field of view. Additionally, manual error in setting the focal plane, either not exactly at the center of the culture well or in z-direction positioning, may result in misalignment of the μPIV data and the COMSOL data. Despite these factors, the simulated velocity profile provides a reasonable approximation of the fluid flow within the microfluidic device. Thus, a parametric study of flow velocity with respect to input flow rate can be used to determine the fluid shear stress.

To determine the flow rate for optimal shear stress within the culture well, computational fluid dynamic simulations were performed with inlet flow rates of 5 μL/min, 30 μL/min, 100 μL/min, and 500 μL/min. Wall fluid shear stress was calculated as the maximum value of the shear stress calculated using Newton's Law of Viscosity. It has previously been reported that kidney organoids vascularization and maturation can be enhanced by applying wall fluid shear stress ranging from 0.008 – 0.035 dyne/cm^2 (*42*). Interestingly, the calculated wall fluid shear stress at 100 μL/min, 0.018 dyne/cm^2, was near the middle of this high shear stress range (Figure 3.3E). Therefore, kidney organoids were cultured under continuous perifusion at this flow rate in the following studies.

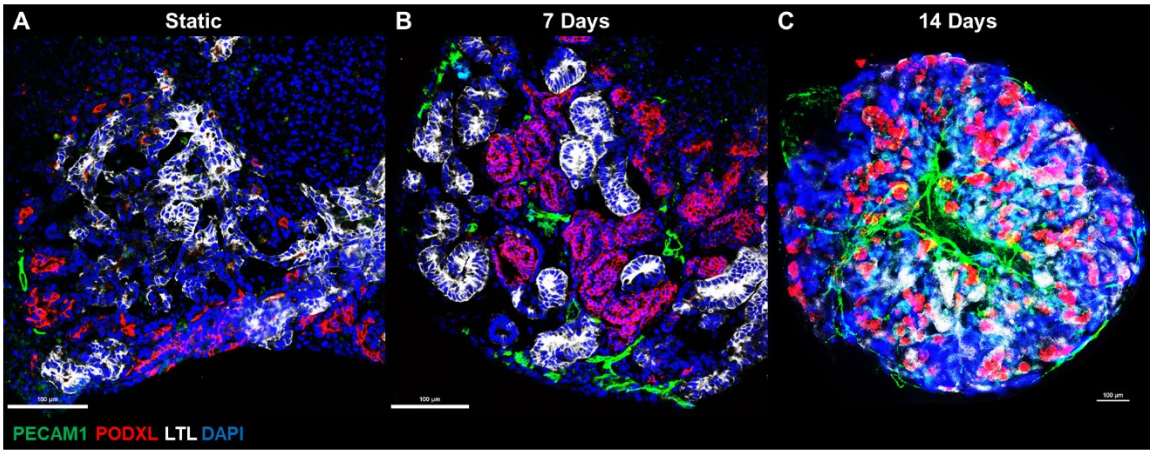

Figure 3.4 Immunofluorescence staining of kidney organoids. (A) Representative staining of a kidney organoid section after completing the differentiation protocol under static conditions. (B) Representative staining of a kidney organoids section after 7 days of continuous perfusion during the final step of the differentiation protocol. (C) Representative staining of a kidney organoid after completing the final step of the differentiation protocol under continuous perifusion in the microfluidic device. Scale bars = 100 µm; PECAM1 – vascular marker, PODXL – glomerular marker, LTL – tubule marker, DAPI – nuclei. *Imaging performed by Kohei Uchimura from the Humphreys Lab at Washington University.*

3.2.3 Shear stress promotes vascularization and maturation of kidney organoids

The primary function of the kidneys is to filter waste products from the blood (*43*). As a result, kidney cells are exposed to significant fluid shear stress. However, the static culture protocols for kidney organoids results in immature organoids with limited vascular networks (*44-46*). Additionally, Fluid shear stress has been shown to be beneficial for endothelial cells and promote vascularization of organoids (*42, 47*). Therefore, we sought to expose kidney organoids to fluid shear stress during the differentiation protocol.

Kidney organoids were generated following the previously described Little Protocol (*39*). On day 12 of the protocol organoids were either transferred to the microfluidic device for continuous perifusion culture or maintained in static culture. Compared to organoids that completed the differentiation protocol under static conditions, organoids exposed to shear stress for 7 days within the microfluidic device demonstrated increased staining for the endothelial marker, PECAM1 (*48*) (Figure 3.4A-B). At the completion of the differentiation protocol (i.e. 14 days of continuous perifusion culture in

the microfluidic device), further vascularization can be observed (Figure 3.4C). Interestingly, glomerular and tubular structures appeared more well defined and organized in the kidney organoids exposed to shear stress, as indicated by staining for the podocyte marker, podcalyxn (PODXL) (*49*), and the proximal tubule marker, lotus tetragonolobus lectin (LTL) (*50*), respectively. Of note, continuous perifusion at 500 µL/min was also attempted, but the high shear stress destroyed the 3D structure of the developing organoids (data not shown). To characterize the efficiency of the differentiation protocol and maturation of the kidney organoids, qPCR was performed to quantify the expression of various markers (Appendix A3).

3.4 Discussion

Organs-on-chips have emerged as an exciting new technology to recapitulate human physiology. Here, we have adapted our previously developed fluidic platform for the differentiation and maturation of kidney organoids. A thorough analysis of the fluid dynamics within the microfluidic device was performed. Using confocal µPIV, we were able to characterize the flow profile. Computational modeling was used to not only model the flow profile, but also to perform a parametric study of flow rate and shear stress within the device. Based on this characterization, the optimal shear stress for vascularization and maturation of kidney organoids was determined. Further, we demonstrated that kidney organoids could be cultured on the microfluidic device for up two weeks under continuous perifusion. During this exposure to shear stress, kidney organoids showed enhanced vascularization. Additionally, at the end of the differentiation protocol, kidney organoids exposed to shear stress demonstrated enhanced expression of renal markers.

Although these results have been previously shown, the confirmation of previous findings within our platform highlights the value of dynamic culture for organoid development. Additionally, the adaptation of our platform for kidney organoids, with minimal design modifications, provides promising evidence that the platform could be widely applicable for other organoid models. Further analysis using single cell PCR will be completed to better characterize the cellular populations and pathways affected by shear stress. Future work with the kidney organoids on our platform will focus on functional assessments (e.g. vitamin D metabolism).

CHAPTER 4

Engineered Microfluidic Platform for Simultaneous Interrogation of Hormone Secretion and Intracellular Signaling using a Pseudoislet System

4.1 Overview

Pancreatic islets of Langerhans are small collections of specialized endocrine cells, interspersed throughout the pancreas, that maintain glucose homeostasis. Islets primarily consist of α, β, and δ endocrine cells, but other supporting cells can also be found, such as endothelial cells, nerve fibers, and immune cells. Insulin, secreted from the β cells, lowers blood glucose by stimulating glucose uptake in peripheral tissues. Glucagon, on the other hand, is secreted from α cells and raises blood glucose through its actions in the liver. Importantly, dysfunction of β and/or α cells is a key feature in all forms of diabetes mellitus (*51-61*). Thus, an improved understanding of the pathways governing the coordinated hormone secretion in human islets may provide insight into the pathogenesis of diabetes.

In β cells, the central pathway of insulin secretion involves glucose entry via glucose transporters. The metabolism of glucose results in an increased ATP:ADP ratio. This shift causes ATP-sensitive potassium channels to close and results in depolarization of the cell membrane. Voltage-dependent calcium channels then open and the influx of calcium triggers exocytosis of insulin granules (*62*). In α cells, the pathway of glucose inhibition through glucagon secretion is not clearly defined, with both intrinsic and paracrine mechanisms proposed (*63-65*). Further, gap junctional coupling and paracrine signaling between endocrine cells within the 3D islet architecture are critical for islet function, as individual α or β cells do not show the same coordinated secretion pattern seen in intact islets (*66-70*).

The 3D islet architecture, while essential for function, presents experimental challenges for mechanistic studies of intracellular signaling pathways in primary islet cells. Additionally, human islets have been shown to differ from rodent islets in many ways, including the arrangement of endocrine cell populations, glucose set-point, and both basal and stimulated insulin and glucagon secretion profiles. As a result, studying signaling pathways in primary human cells is vital for understanding dysfunction in disease (*71-74*).

To study signaling pathways in primary human islet cells within the context of their 3D arrangement, we developed an integrated approach that consists of: 1) human pseudoislets, established by the Powers and Brissova Group at Vanderbilt University, which closely mimic native human islet biology and allow for efficient genetic manipulation; and 2) a microfluidic system, developed in the Physiomimetic Microsystems Laboratory, with the ability to perform synchronous assessment of intracellular signaling dynamics and both insulin and glucagon secretion. Using this experimental approach, we demonstrate synchronous interrogation of intracellular signaling and hormone secretion.

4.2 Materials and Methods

4.2.1 Human islet isolation

Human islets were obtained through partnerships with the Integrated Islet Distribution Program (IIDP, http://iidp.coh.org/), Alberta Diabetes Institute (ADI) IsletCore (https://www.epicore.ualberta.ca/IsletCore/), Human Pancreas Analysis Program (https://hpap.pmacs.upenn.edu/), or isolated at the Institute of Cellular Therapeutics of the Allegheny Health Network (Pittsburgh, PA). Assessment of human islet function was performed by islet macroperifusion assay on the day of arrival at Vanderbilt University, as

previously described (*75*). Primary human islets were cultured in CMRL 1066 media (5.5 mM glucose, 10% FBS, 1% Pen/Strep, 2 mM L-glutamine) in 5% CO_2 at 37°C for <24 hours prior to beginning studies. The Vanderbilt University Institutional Review Board does not classify de-identified human pancreatic specimens as human subject research.

4.2.2 Pseudoislet formation and adenovirus transduction

Pseudoislet formation and adenovirus transduction was performed at Vanderbilt University by the Powers and Brissova Group. Briefly, human islets were handpicked to purity and then dispersed with HyClone trypsin (Thermo Scientific). Islet cells were counted and then seeded at 2000 cells per well in CellCarrier Spheroid Ultra-low attachment microplates (PerkinElmer) or 2500 cells per drop in GravityPLUSTM Hanging Drop System (InSphero) in enriched Vanderbilt pseudoislet media. Cells were allowed to reaggregate for 6 days before being harvested and studied.

An adenoviral vector, CMV-hM3Dq-mCherry (VB160707-1172csx), was constructed by VectorBuilder Inc (Chicago, IL) and a prepared, amplified, and purified by the Human Islet and Adenovirus Core of the Einstein-Sinai Diabetes Research Center (New York, NY) or at Welgen Inc (Worcester, MA). Titers were determined by plaque assay. Ad-CMV-GCaMP6f was purchased from Vector Biolabs (Catalog #1910, Malvern, PA). Dispersed human islets were incubated with adenovirus at a multiplicity of infection of 500 for 2 hours in Vanderbilt pseudoislet media before being spun, washed, and plated.

4.2.3 Design and fabrication of microperifusion platform

The microperifusion platform is based on a previously published microfluidic device with modifications (*6*). Design modifications were incorporated using SolidWorks 2018 3D computer-aided design (CAD) software. Microfluidic devices were machined,

according to the CAD models, using a computer numerical controlled milling machine (MDX-540, Roland) from poly(methyl methacrylate) (PMMA) workpieces. To reduce the optical working distance, through-holes were milled into the culture wells and a #1.5 glass coverslip was bonded to the bottom component of the microfluidic device using a silicone adhesive (7615A21, McMaster-Carr). Custom gaskets were fabricated using a two-part silicone epoxy (Duraseal 1533, Cotronics Corp) and bonded into the top component of the device using a specialized polyester adhesive (PS-1340, Polymer Science). The two components of the microfluidic device are assembled in a commercially available device holder (Fluidic Connect PRO with 4515 Inserts, Micronit Microfluidics), which creates a sealed system and introduces fluidic connections to a peristaltic pump (Instech, P720) through 0.01" FEP tubing (IDEX, 1527L) and a low volume bubble trap (Omnifit, 006BT) placed in the fluid line just before the device inlet to prevent bubbles from entering the system.

4.2.4 Macroperifusion assessment

Function of native islets and pseudoislets was studied in a dynamic cell perifusion system at a perifusate flow rate of 1 mL/min as described in (*51, 75*) using approximately 250 IEQs/chamber. The effluent was collected at 3-minute intervals using an automatic fraction collector. Insulin and glucagon concentrations in each perifusion fraction and islet extracts were measured by radioimmunoassay (insulin: RI-13K, glucagon: GL-32K, Millipore, Burlington, MA). Macroperifusion assessment was performed at Vanderbilt University.

4.2.5 Microperifusion assessment

The microperifusion apparatus was contained in a temperature-controlled incubator (37°C) fitted to a Zeiss LSM 880 laser-scanning confocal microscope (Zeiss Microscopy Ltd, Jena, Germany). Pseudoislets (approximately 25 IEQs/chamber) were loaded in a pre-wetted well, imaged with a stereomicroscope to determine loaded IEQ, and perifused at 100 µL/min flow rate with Krebs-Ringer buffer containing 125 mM NaCl, 5.9 mM KCl, 2.56 mM CaCl2, 1 mM MgCl2, 25 mM HEPES, 0.1% BSA, pH 7.4 at 37°C. Perifusion fractions were collected at 2-minute intervals following a 20-minute equilibration period in 2 mM glucose using a fraction collector (Bio-Rad, Model 2110) and analyzed for insulin and glucagon concentration by radioimmunoassay (insulin – RI-13K, glucagon – GL-32K, Millipore). The GCaMP6f biosensor was excited at 488 nm and fluorescence emission detected at 493 – 574 nm. Images were acquired at 15-µm depth every 5 seconds using a 20x/0.80 Plan-Apochromat objective. Image analysis was performed with MetaMorph v7.1 software (Molecular Devices, San Jose, CA). Pseudoislets in the field of view (3-7 pseudoislets/field) were annotated using the region of interest tool. The GCaMP6f fluorescence intensity recorded for each time point was measured across annotated pseudoislet regions and normalized to the baseline fluorescence intensity acquired over the 60 seconds in 2 mM glucose prior to stimulation. The calcium, insulin, and glucagon traces were averaged from 5 microperifusion experiments from 3 independent donors. Synchronous assessment of hormone secretion and calcium signaling was performed at Vanderbilt University in collaboration with Heather Nelson, who performed the data analysis.

4.2.6 Computational modeling of fluid dynamics and mass transport

Two-dimensional (2D) finite element method (FEM) models, which incorporate fluid dynamics, mass transport, and islet physiology, were developed for the macroperifusion and microperifusion platforms and implemented in COMSOL Multiphysics Modeling Software (Release Version 5.0). Fluid dynamics were governed by the Navier-Stokes equation for incompressible Newtonian fluid flow. Convective and diffusive transport of oxygen, glucose, and insulin were governed by the generic equation for transport of a diluted species in the chemical species transport module. Islet physiology was based on Hill (generalized Michaelis-Menten) kinetics using local concentrations of glucose and oxygen, as previously described (*7, 11*).

4.2.7 Statistical methods

Data were expressed as mean ± standard error of mean. A p-value less than 0.05 was considered significant. Analyses of area under the curve and statistical comparisons (Mann-Whitney test, Wilcoxon matched-pairs signed rank test, and one- and two-way ANOVA) were performed using Prism v8 software (GraphPad, San Diego, CA). Statistical details of experiments are described in the Figure Legends and Results.

4.3 Results

4.3.1 Optimization of microfluidic platform

The microfluidic platform is comprised of bio-inert and non-absorbent microfluidic device with a fluidic geometry for optimized design for nutrient delivery, synchronous islet imaging via confocal microscopy, and collection of effluent fractions for analysis of insulin and glucagon secretion (Figure 4.1A). The microfluidic device was modified to improve the imaging resolution within the culture well. In the original microfluidic device, approximately 1.5 mm of PMMA was present below the culture well (Figure 4.1B). This results in a large working distance for standard microscope objectives. Additionally, the refractive index of PMMA is slightly higher than the refractive index of glass, which can

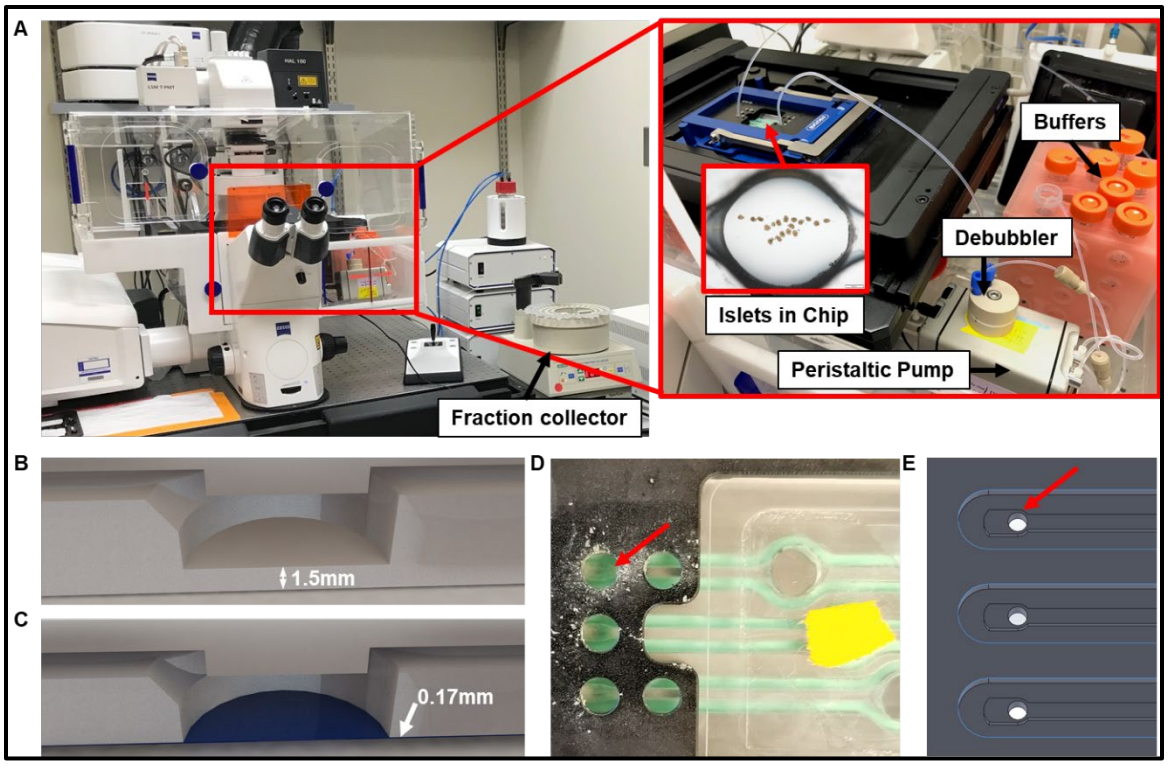

Figure 4.1Microperifusion system and device optimization. (A) Experimental setup of the microfluidic device on the confocal microscope stage within the incubator chamber including fraction collector, peristaltic pump, debubbler, and perifusion buffers. (B) Original microfluidic device with 1.5 mm thick PMMA below the culture well. (C) Modified microfluidic device where the PMMA has been replaced by a glass coverslip that is approximately 0.17 mm thick. (D) Occlusion of the fluidic ports by gaskets after repeated use. (E) 3D CAD design of modified ports that include a wall to prevent occlusion by the gaskets.

Table 4.1 Key experimental parameters of macroperifusion and microperifusion system

Perifusion parameters	Macro	Micro
Chamber volume (μL)	1500	65
Flow rate (μL/min)	3000	100
Fraction time (mins)	3	2
Stimulus time (mins)	21	8
Islet equivalents	~250	~25

hinder high resolution imaging. To address this issue, the PMMA below the culture was milled away and replaced with a #1.5 glass coverslip (~0.1 mm thick) (Figure 4.1C).

During initial testing of the microfluidic platform, an unanticipated failure mode was observed. Although the microfluidic device was designed to be resealed and reused, the repeated compression caused wear and tear of the silicone gaskets used to seal the device. As a result, the gaskets became softer and can occluded the ports of the microfluidic device (Figure 4.1D). Partial occlusion of the ports can increase the fluidic resistance of the microfluidic device. While large pumps can often overcome this, the small peristaltic pump implemented in the microperifusion could not and flow was impeded. To resolve this failure mode, the device was further modified to include thin walls around the fluidic ports (Figure 4.1E). Following this design modification, the flow through the microfluidic was consistent at the desired flow rate.

4.3.2 Comparison of macro- and micro-perifusion assessments

The microperifusion system uses smaller volumes, slower flow rates, and fewer islets than our conventional macroperifusion system. Therefore, finite element modeling of fluid dynamics and mass transport was utilized to compare the two systems and experimental parameters. The geometry of the macroperifusion platform was modeled as the 2D cross-section of a cylindrical tube with fluid flowing from bottom to top (Figure

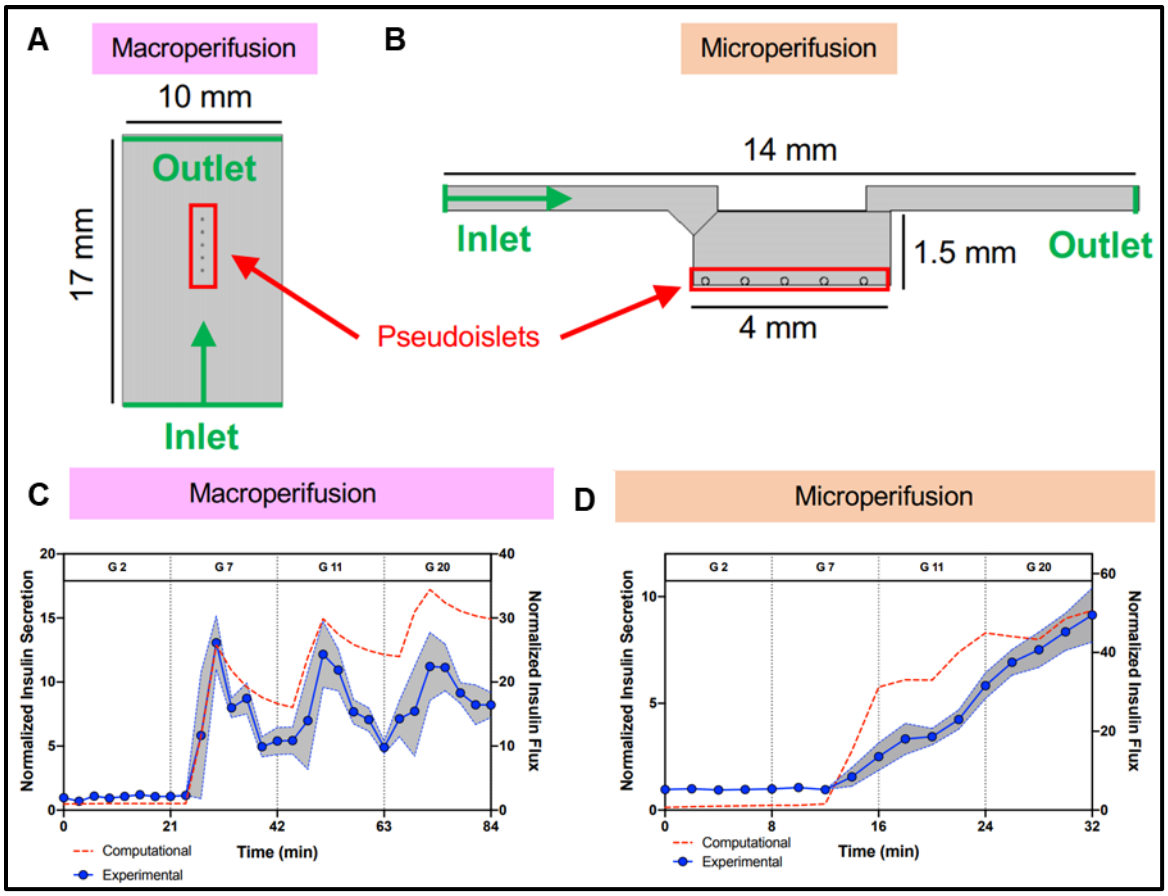

Figure 4.2 Computational model of the macro- and micro-perifusion systems. (A-B) Schematic of the macroperifusion (A) and microperifusion chamber (B) showing the path of fluid flow. (C-D) Comparison of normalized insulin secretion acquired experimentally versus predicted by modeling in macroperifusion (C) and microperifusion (D). Experimental insulin data was normalized to average value in 2 mM glucose. The gray region demonstrates the SEM comparing experimental insulin secretion data and insulin flux from COMSOL computational modeling in the macroperifusion system (C) and microperifusion system (D); G 2 – 2 mM, G 7 – 7 mM, G 1 – 11 mM, G 20 – 20 mM glucose.

4.2A). The geometry of the microperifusion platform was modeled as a 2D cross-section of the microfluidic device with fluid flow from left to right (Figure 4.2B). In both the macroperifusion and microperifusion models, 5 islets with a diameter of 150 µm (5 IEQs) were placed in the flow path. FEM models were solved as a time-dependent problem, allowing for intermediate time-steps that corresponded with the fraction collection time during macro- and micro-perifusion. For initial validation, the experimental parameters for both systems were modeled (Table 4.1). This modeling accurately predicted the overall shape of each insulin secretory trace, with the macroperifusion showing a “saw-tooth”

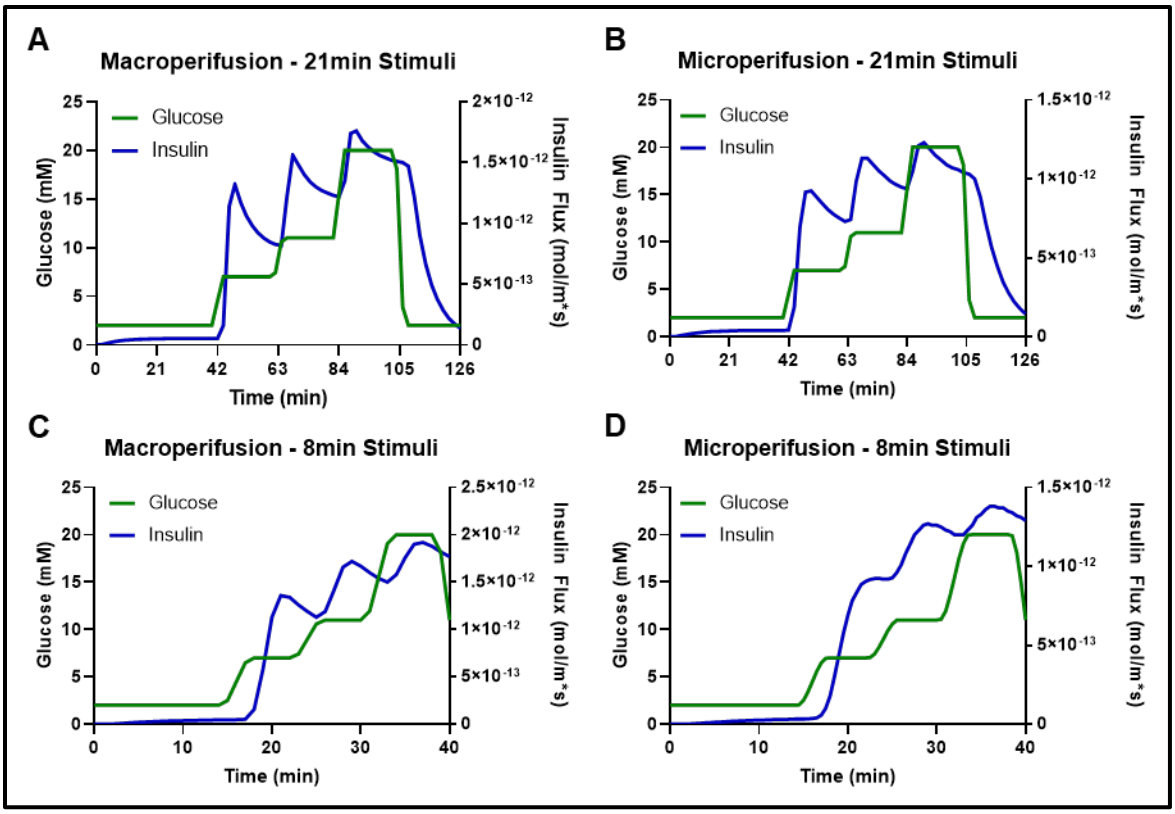

Figure 4.3 Comparison of experimental parameters in macro- and micro-perifusion systems. (A-B) Simulation of glucose stimulus and insulin secretion in both systems using the macroperifusion experimental parameters. (C-D) Simulation of glucose stimulus and insulin secretion in both systems using the microperifusion experimental parameters.

pattern (Figure 4.2C) while the microperifusion had a more progressive increase (Figure 4.2D).

Next, we sought to characterize if the difference in insulin secretion was due to the inherent geometrical differences in the two systems or the differences in the experimental parameters. To do this, insulin secretion was simulated in both systems while holding the experimental parameters (flow rate, fraction time, and stimulus time) constant (Figure 4.3). Interestingly, using the macroperifusion experimental parameters, the saw-tooth pattern appears in the insulin secretion profile of the microperifusion system (Figure 4.3A-B). Additionally, with the microperifusion experimental parameters, the insulin secretion response is blunted in the macroperifusion system (Figure 4.3C-D). In all the simulations,

the glucose stimulus profile is very similar. Using this approach, we found that differences in the insulin secretory profiles were primarily due to the different fluid dynamics and experimental parameters between the two perifusion systems, especially the experimental

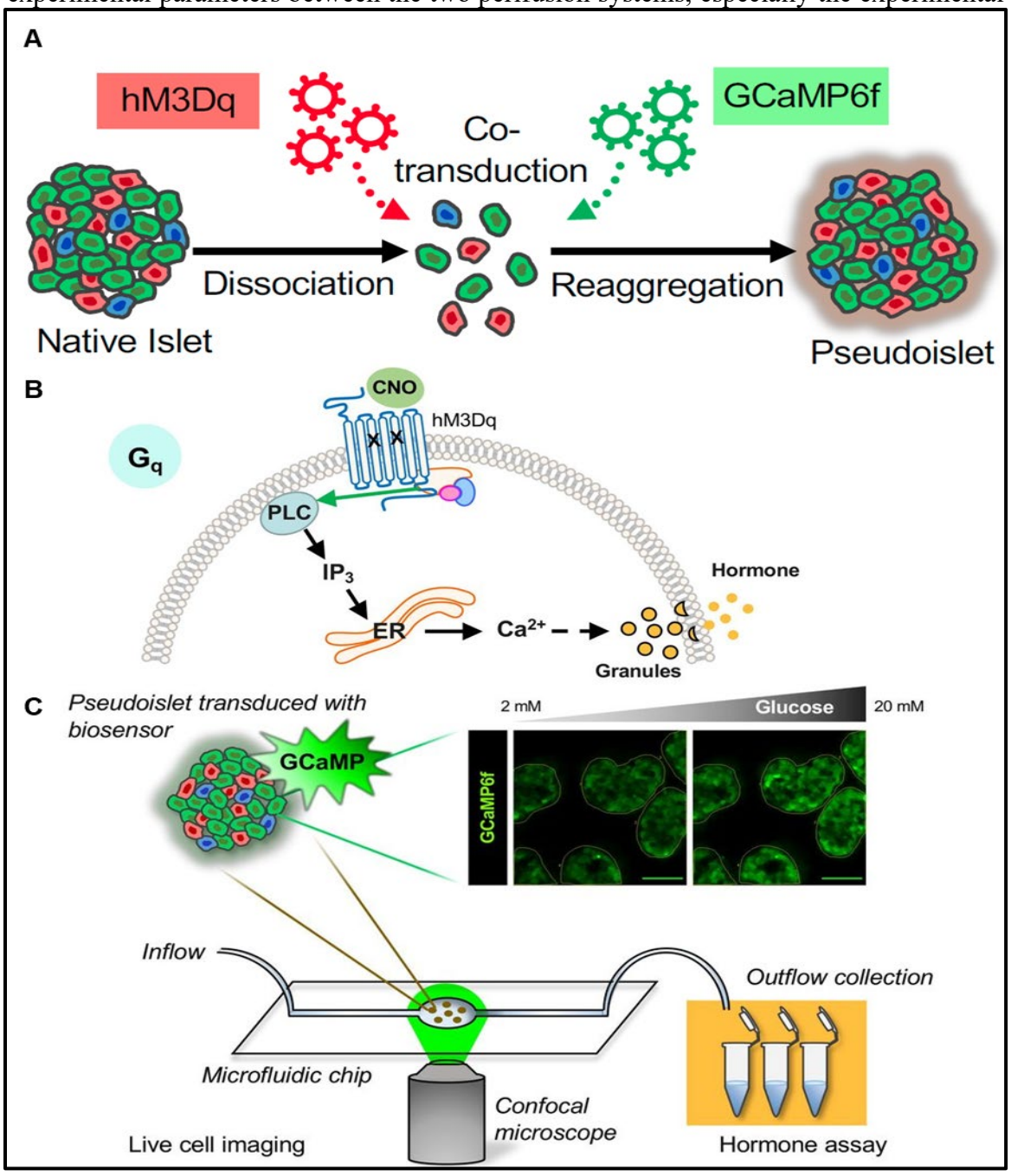

Figure 4.4 Schematic of experimental approach for synchronous measurement of intracellular signaling and hormone secretion. (A) Schematic of experimental workflow to incorporate genetically encoded biosensor into hM3Dq-expressing pseudoislets. (B) Schematic of the Gq-coupled GPCR signaling pathway. CNO – clozapine-N-oxide, PLC – phospholipase C, IP_3 – inositol triphosphate, ER – endoplasmic reticulum, Ca^{2+} calcium ion. (C) Schematic of pseudoislet integration into microfluidic device. *Adapted from images produced by the Powers and Brissova Group at Vanderbilt University.*

time for each stimulus and the flow rate. Overall, this analysis demonstrates how perifusion parameters can impact insulin secretory pattern and indicates the strength of using complementary approaches. It also emphasizes the importance of validating new microperifusion devices by comparing these with macroperifusion that have been used for many years by many laboratories.

4.3.3 Synchronous measurement of intracellular signaling and hormone secretion

To investigate the dual effects of activated G_q signaling on insulin secretion, we co-transduced pseudoislets with hM3Dq and GCaMP6f, a calcium biosensor (Figure 4.4A). hM3Dq, is a G_q designer receptor exclusively activated by designer drugs (DREADD). DREADDs are a type of G-protein coupled receptor (GPCR) with specific point mutations that render them unresponsive to their endogenous ligand. Instead, they can be selectively activated by the otherwise inert ligand, clozapine-N-oxide (CNO), thus providing a selective and inducible model of GPCR signaling (*76, 77*). This class of G_q-coupled GPCRs signal through phospholipase C, leading to IP_3-mediated Ca^{2+} release from the endoplasmic reticulum (Figure 4.4B). While conventional macroperifusion systems, including the macroperifusion system used in this study reliably assess islet hormone secretory profiles (*51, 56, 57, 75, 78*), their configuration does not allow coupling with imaging systems to measure intracellular signaling. To overcome this challenge, we developed an integrated microperifusion system consisting of pseudoislets and a microfluidic device that enables studies of islet intracellular signaling using genetically-encoded biosensors in conjunction with hormone secretion (Figure 4.4C).

In the absence of CNO, hM3Dq-expressing pseudoislets had stepwise increases in GCaMP6f relative intensity as glucose increased, corresponding to increasing intracellular

Ca^{2+} and highlighting the added value of the system (Figure 5B). This intracellular Ca^{2+} response to stepwise glucose increase was accompanied by increasing insulin secretion (Figure 5C), but the first phase of insulin secretion was not as clearly resolved as in the macroperifusion.

When G_q signaling was activated with CNO, a transient stimulation of insulin secretion at low glucose followed by relative inhibition through the glucose ramp was observed, while glucagon secretion from α cells was stimulated throughout the entire

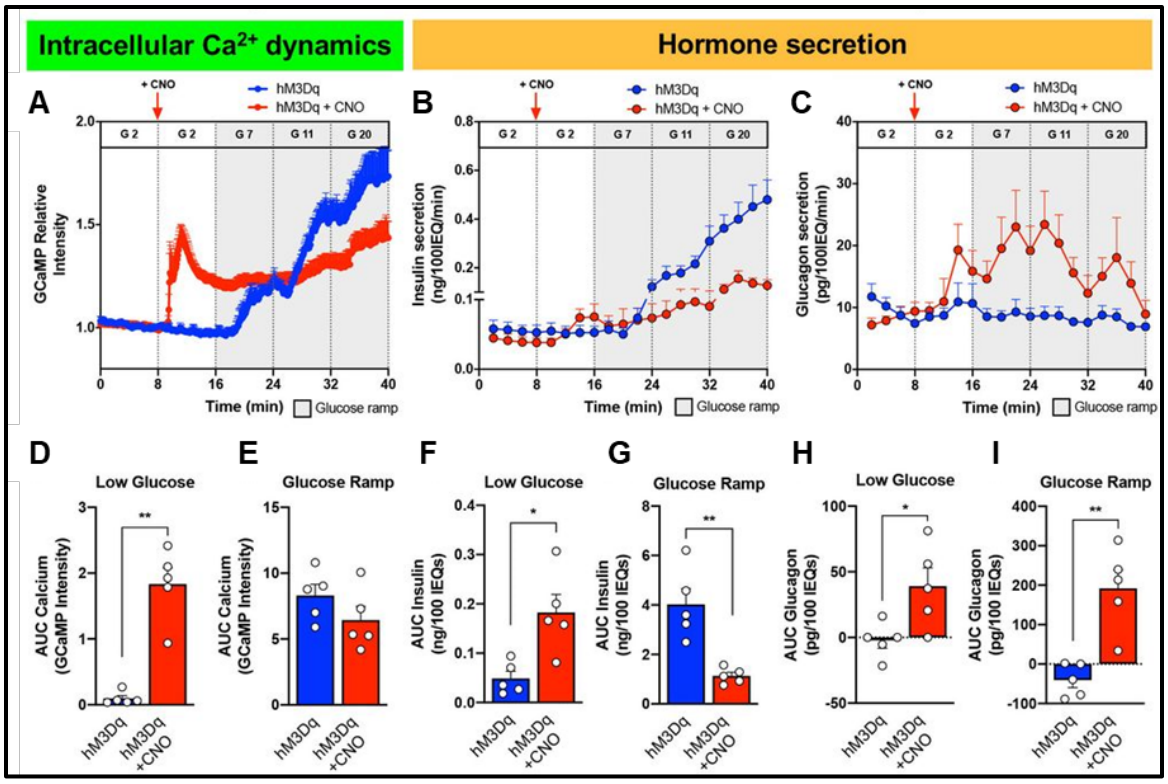

Figure 4.5 Co-registration of hormone secretion and intracellular signaling dynamics. Dynamic changes in GCaMP6f relative intensity (A), insulin secretion (B), and glucagon secretion (C) assessed during microperifusion in response to a low glucose (G 2 – 2 mM glucose; white), glucose ramp (G 7 – 7 mM, G 11 – 11 mM, and G 20 – 20 mM glucose; grey) and in the absence (blue trace) or presence of CNO (red trace); n=3 donors/each. 10 µM CNO was added after the first period of 2 mM glucose as indicated by a vertical red arrow and then continuously administered for the duration of the experiment (red trace). See Appendix A4 for representative video visualizations of each experiment. Calcium signal (D,E) and insulin (G, H) and glucagon (I, J) secretion was integrated by calculating the area under the curve (AUC) for response to the low glucose (white) and glucose ramp (gray). Baseline was set to the average value of each trace from 0 to 8 minutes (before CNO addition). Calcium and hormone traces in panels B-D were compared in the absence vs. presence of CNO by two-way ANOVA; * $p < 0.05$ for calcium trace, **** $p < 0.0001$ for both insulin and glucagon secretion. Area under the curve of calcium (E, F), insulin (G, H) and glucagon responses (I, J) to low glucose and glucose ramp were compared in the absence vs. presence of CNO by Mann-Whitney test; *, $p < 0.05$, **, $p < 0.01$. Data are represented as mean ± SEM. *Figure produced by Heather Nelson from the Powers and Brissova Group at Vanderbilt University.*

perifusion, independently of glucose concentration (Figures 4.5B, 4.5C, 4.5D-I). Furthermore, the Ca^{2+} dynamics in response to G_q activation were consistent with the insulin secretory trace showing a rapid but short-lived increase in intracellular Ca^{2+}. Interestingly, the Ca^{2+} signal remained elevated above baseline but did not significantly increase with rising glucose (Figures 4.5A, 4.5D and 5E). This indicates that the dual effects of G_q signaling on insulin secretion in β cells are largely mediated by changes in intracellular Ca^{2+} levels.

4.4 Discussion

The three-dimensional multicellular architecture of human islets, while essential function, presents experimental challenges for mechanistic studies of intracellular signaling pathways. To evaluate the coordination between intracellular signals and islet hormone secretion, we developed an integrated system consisting of pseudoislets and a microfluidic device that enables studies of islet intracellular signaling using genetically encoded biosensors in conjunction with hormone secretion. Furthermore, we used this integrated approach to define new aspects of human islet biology by investigating GPCR signaling pathways using DREADDs and a calcium biosensor.

Despite α and β cells both being excitable secretory cells and sharing many common developmental and signaling components, this experimental approach enabled characterization of a distinct response due to activation of GPCR signaling pathways. The activation of G_q signaling showed major differences in β and α cells. In α cells, the activated G_q signaling elicited a robust and sustained increase in glucagon secretion in the presence of a glucose ramp. In contrast, G_q signaling in β cells had a transient stimulatory effect in low glucose and then inhibitory effects on both insulin and intracellular Ca^{2+} levels with

sustained activation during glucose ramp. Interestingly, previous studies of acetylcholine signaling have also reported dual effects on Ca^{2+} dynamics in β cells depending on the length of stimulation (*79*). This signaling was thought to be mediated through the muscarinic acetylcholine receptor M_3 (from which the hM3Dq DREADD is based). Overall, these results suggest a negative feedback or protective mechanism that prevents sustained insulin release from β cells in response to G_q signaling that is not active in α cells under similar circumstances.

There are limitations and caveats to the current study. First, our approach expressed the DREADD receptors in all cell types. Although we can distinguish the effects on β and α cells through the cell's distinct hormone secretion, it is possible that paracrine signaling, including somatostatin from δ cells, is contributing to the results described here. Future modifications could incorporate cell-specific promoters to target specific islet cell types. Second, the DREADD receptors are likely expressed at higher levels than endogenous GPCRs. To mitigate this, we used the appropriate DREADD-expressing pseudoislets as our controls and were encouraged to see normal secretory responses in these control pseudoislets. Third, while there is some concern that CNO can be reverse-metabolized *in vivo* into clozapine which could potentially have off-target effects (*80*), this is unlikely to impact our *in vitro* system. Further, while we used a CNO concentration of 10 μM for all experiments, a standard concentration used for *in vitro* assays (*70, 81*), it is possible that islet cells may respond in a dose-dependent manner. Finally, this is an *in vitro* study, and there may be differences in these pathways compared to what is seen *in vivo*. Future work could involve transplantation of DREADD-expressing pseudoislets into immunodeficient mice to study the effect of activating these pathways on human islets *in vivo* (*82*).

CHAPTER 5

Oxygen Permeable Microphysiological System for Functional Preservation of Pancreatic Islets embedded in 3D Matrix

5.1 Overview

The practice of *in vitro* cell culture on static, two-dimensional (2D) glass or polystyrene surfaces has provided the foundation for numerous biomedical discoveries over the last century. The inability of these culture systems to recapitulate critical human *in vivo* physiological responses, however, has been well-documented (*21, 83*). Replacement of human cell monolayers with three-dimensional (3D) organoids, procured from biopsies, cadaveric organ donations, or the self-organization of cultured pluripotent stem cells, provides superior *in vitro* models for the investigation of complex biological phenomenon and the effective screening of new pharmaceuticals (*84*). For example, 3D multi-cellular pancreatic islets of Langerhans are considered widely superior to beta cell monolayers for studying pancreatic physiology and autoimmune diabetes, as well as for drug screening and cellular transplantation (*85, 86*).

Maintaining primary organoids, such as pancreatic islets, *in vitro* is exceptionally challenging. The current standard protocols for culturing primary islets (i.e. static culture in a flask or petri dish under low seeding densities) are suboptimal, resulting in significant temporal declines in cell mass and function (*87*). This can be partly attributed to both the loss of native 3D microarchitecture and the deficient delivery of nutrients *in vitro* (*88*). As a result, the utility of islet organoids for pharmaceutical screenings, biological studies, and transplantation therapies is extremely limited. Overcoming these challenges has proven difficult due to the complexity of developing *in vitro* culture systems that provide key

features of the *in vivo* environment, such as a 3D support matrix and a sufficient supply of nutrients, while retaining ease of use in a general laboratory setting.

To provide 3D support for spatiotemporal cellular activity of organoids, hydrogels made from synthetic or natural-based materials have been used (*89*). Alginate, a seaweed-derived polysaccharide, has been extensively studied for 3D encapsulation of cells due to its low toxicity, ease of gelation, and tunable properties (*90*). Due to its inert nature and biostability, the *in vitro* immobilization of cells within an alginate hydrogel also facilitates cell specific imaging and tracking during extended culture periods. However, embedding organoids within 3D hydrogels creates an additional barrier to the diffusion of solutes, resulting in decreased nutrient delivery during conventional static culture. For organoids with high metabolic activity, such as islets, static culture in a bulk 3D matrix is highly unsuitable for maintaining long-term cell viability and function (*87*).

Dynamic culture systems, such as stirred flasks, rotating-wall vessels, hollow fibers, and direct perifusion chambers, can improve mass transport for effective nutrient delivery and waste removal (*91*). The widespread implementation of these approaches for organoid culture is hindered by their large culture media volumes and limited compatibility with existing assays. Microphysiological systems (MPS), such as organs-on-chips, have the potential to address these challenges by significantly decreasing the culture scale and facilitating the integration of sensors, functional readouts, and optical monitoring (*5*). These microfluidic devices are commonly fabricated from polydimethylsiloxane (PDMS), a noncytotoxic silicone polymer (*28*). However, the fabrication of PDMS-based MPS requires highly specialized photolithography facilities and the inherent size restrictions of this method creates challenges in developing MPS for organoid culture (*92*).

Substituting PDMS for poly(methyl methacrylate) (PMMA) as the manufacturing material, we engineered an MPS platform for the long-term continuous dynamic culture of organoids within a 3D hydrogel. Rodent- and human-derived islets were embedded in alginate and integrated into our MPS or cultured using traditional methods. The impact of the culture systems on islet health were temporally assessed and compared, both *in silico* and *in vitro*. We further demonstrated the ability of our MPS to platform serial dynamic characterization of islet function, through collaboration with Smit Patel, from the Stabler Lab at the University of Florida. With the establishment of a successful 3D islet organoid culture system using our MPS, leveraging this platform for the study of autoimmune diabetes and the screening of diabetic pharmaceutical agents and/or therapies is discussed.

5.2 Materials and Methods

5.2.1 Design and fabrication of organoid MPS

The design of the modified fluidic chips was performed in SolidWorks 2018 3D computer-aided design (CAD) software (Dassault Systèmes, France). Fluidic chips were machined from optically clear PMMA workpieces (McMaster-Carr, Elmhurst, IL) using an MDX-540 computer numerical control (CNC) milling machine (Roland, Japan). The final form factor of the fluidic chip was laser cut from the workpiece with a 30W CO_2 Laser Engraver (Epilog Laser, Golden, CO). To locally supply oxygen to islets, the culture wells were through cut and a 25 μm thick PFA membrane (McMaster-Carr, Elmhurst, IL) was bonded to the bottom piece of the device using a silicone adhesive (McMaster-Carr, Elmhurst, IL). The fluidic device was assembled in a commercially available microfluidic chip holder (Micronit Microfluidics, Netherlands) with silicone gaskets, developed inhouse, to seal the system and introduce fluidic connections. To prevent bubbles from

entering the fluidic chip, a low volume bubble trap (Darwin Microfluidics, France) was placed in the fluid line just before the inlet. The fluidic devices were sterilized with ethylene oxide gas prior to the cell culture experiments.

5.2.2. Oxygen partial pressure measurement

To measure oxygen in the fluidic platform, an optical oxygen sensor was incorporated into the fluidic chip. Briefly, an oxygen spot sensor was bonded to the roof of the culture well and the partial pressure of oxygen was monitored via polymer optical fibers connected to a multi-channel oxygen meter (PreSens, Germany). The fluidic platform was first purged of oxygen by pumping in nitrogen. Once the oxygen pressure was sufficiently low, the nitrogen flow was shut off and the partial pressure of oxygen was recorded for 5 min while oxygen from the ambient air permeated into the culture well. Oxygen permeation measurements were performed at room temperature.

5.2.3 Computational modeling

Finite element method (FEM) models of fluid dynamics, mass transport, and rodent pancreatic islet function within the MPS was developed in COMSOL Multiphysics 5.0 (COMSOL Inc., Burlington, MA). The model consisted of a 2D cross-section of the islet MPS geometry and ten circular regions, each representing an islet with a diameter of 150 μm, spaced 750 μm apart. A static culture model was developed based on the geometry of a single well from a 48-well culture plate. Both the islet MPS and static culture models included an alginate region. Fluid dynamics were governed by the incompressible Navier-Stokes equation with a no-slip boundary condition. Convective and diffusive mass transport of oxygen, glucose, and insulin were governed by the generic equations in the Chemical Species Transport Module of COMSOL. Diffusion coefficients for each species

in different media were obtained from literature (*11*). Islet function was incorporated using a previously described and validated local concentration-based insulin secretion model (*7*). Hypoxia-induced islet dysfunction was defined as the islet area where oxygen concentration was below 5.1×10^{-4} mol/m^3 after simulating 24 h in culture. Insulin secretion from islets in the static culture model was determined by recreating the dysfunctional area in a dGSIS model within the Acry-chip geometry. All parameters used for the present model are summarized in Appendix A5.

5.2.4 Pancreatic islet isolation

All animal procedures were conducted under Institutional Animal Care and Use Committee-approved protocols at the University of Florida and in accordance with National Institute of Health guidelines. Rodent islet isolations were performed on 250 to 280 g male Lewis rats (Envigo, United Kingdom), using methods described previously (*93*). Rat islets were handpicked for experiments. Human islets were obtained through participation in the NIDDK-funded Integrated Islet Distribution Program (IIDP). The reported human islets data were generated from a non-diabetic female donor with weight and body mass index (BMI) of 82 kg and 32 kg/m^2 respectively (IIDP RRID: SAMN08612554). Human islets were obtained within six days post-isolation from the isolation center at the University of Miami at the islet viability and purity of 90%. Both human and rodent islets were cultured in CMRL 1066-based media (Mediatech, Manassas, VA) supplemented with 10% fetal bovine serum (HyClone Laboratories, Logan, UT), 25 mM HEPES, 1% penicillin-streptomycin, and 1% L-glutamine (all from Sigma-Aldrich, St. Louis, MO) under standard incubator culture conditions (37º C, 5% CO_2). Rodent islets after isolation and human islets after receiving were cultured overnight in 100 mm × 15

mm nontissue-culture petri-dish(s) at a loading density of 120 IEQ/cm^2 within media of approximately 1.3 mm height prior to utilization for each experiment.

5.2.5 Islet encapsulation and culture

Ultrapure, cGMP grade, medium viscosity sodium alginate (Novamatrix PRONOVA UP MVG, MW > 200 kDa, G/M ratio ≥ 1.5; Dupont, Norway) was dissolved at 1.6% w/v in sterile 1xPBS and filtered through 0.22 μm nylon syringe filter. Islets were handpicked and embedded in prepared alginate, at a loading density of 50 – 100 islets per 25 μL of alginate precursor solution, by gentle mixing until islets were homogeneously distributed within the matrix. The uncrosslinked islet-alginate mixture was then transferred to a standard 48-well plate or loaded within an Acry- or Oxy-Chip cell culture well. Alginate was then gelled via 10 min exposure to BaCl2-MOPS buffer (50 mM $BaCl_2$, 10 mM MOPS, 3 mM KCl, 50 mM NaCl, 0.2 mM Tween 20, pH 7.4), followed by three washes with sterile 1xPBS. Islet MPS were then assembled as described above. Of note, islet cell density was kept consistent for all experiments reported herein. During long-term experiments, islets within the islet MPS were continuously perfused with media at a constant flow rate of 30 μL/min. Static control samples were cultured in a nontissue-culture 48-well plate and incubated with 150 μL media, thus keeping a consistent media height across all platforms. Culture media for all experiments was refreshed every 48 h. Islet encapsulation and culture were performed at the University of Florida by Smit Patel.

5.2.6 Evaluation of islet function

The dGSIS of the islets, rodent and human, was conducted by connecting MPS to a PERI-4.2 perifusion system (Biorep Technologies, Miami Lakes, FL). Control islets in static culture were transferred into a new Acry-Chip, at appropriate time points, for dGSIS

assessments to ensure consistency in stimulation profiles. Standard perifusion buffer containing KRBB buffer (115 mM $NaCl_2$, 4.7 mM KCl, 1.2 mM KH_2PO_4, 1.2 mM MgSO4, 2.5 mM $CaCl_2$, 26 mM $NaHCO_3$, 0.2% w/v BSA, and 25 mM HEPES, pH 7.4) with a selected glucose concentration (low = 3 mM; high = 11 mM) and/or KCl (25 mM) was perifused at a constant flow rate of 30 µL/min. Specifically, islets were first stabilized using low glucose solution for 60 min and then stimulated with a sequence of 20 min low glucose, 30 min high glucose, and 30 min low glucose, 10 min KCl, and 80 min low glucose media. Analytes were collected every 2 min from the outflow tubing and immediately stored at 80°C. Insulin concentrations were quantified using commercially available ELISA kits (Mercodia, Sweden). The values were first converted to µg/L units. They were then converted to pg/min using the constant flow rate as listed above, normalized to the number of handpicked islets, and plotted as a function of time. The dead volume within the circulation tubing and islet MPS channels induced a lag of ~8 min. As such, all dGSIS plots were denoted with 3G, 11G, and/or KCl to represent the stimulation times executed by the perifusion system with an inclusion of the calculated dead volume delay. AUC of an entire region of high glucose, beyond the denoted regions illustrated in the dGSIS plots, was calculated. The peak values were normalized to the corresponding average glucose basal levels for AUC calculations. Of note, during serial assessments of the islet functionality, the dGSIS performed at earlier time points (i.e., 24 h and/or 48 h) did not include the KCl stimulation step. Evaluation of islet function was performed at the University of Florida by Smit Patel.

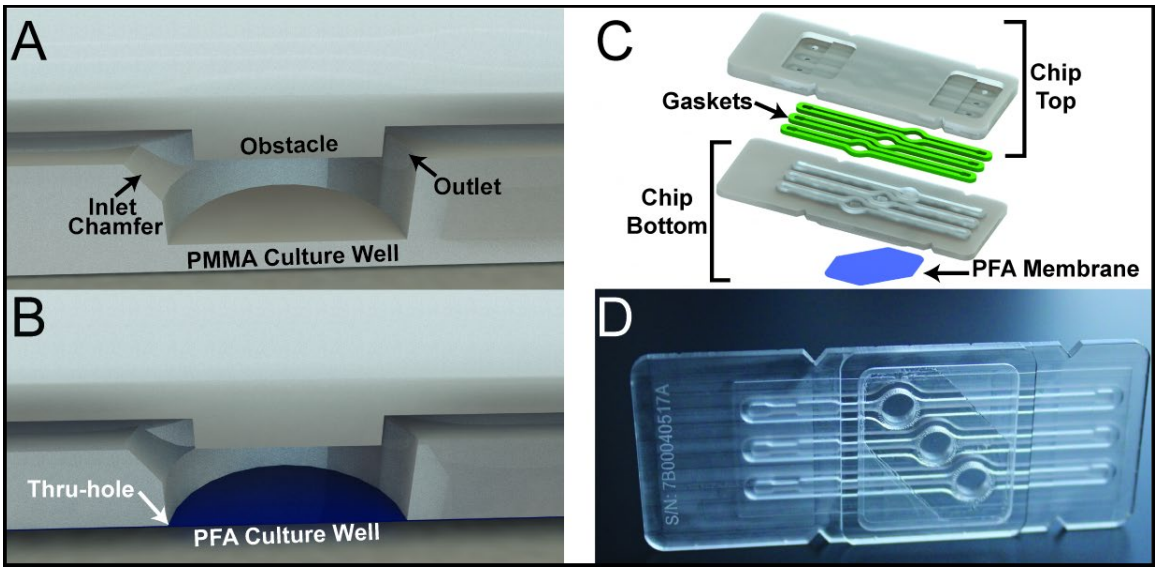

Figure 5.1 Development of organoid MPS (A) 3D CAD render of organoid MPS with PMMA bottom and features for optimized fluid transport. (B) 3D CAD render of organoid MPS chip with a thru-hole for the PFA membrane to enable oxygen permeability in the culture well. (C) Exploded view of 3D CAD render of PFA chip, comprised of a chip top with embedded gaskets to create a fluidic seal and a chip bottom with a PFA membrane for oxygen permeability. (D) Fully fabricated PFA chip bottom with through holes sealed by optically clear PFA membrane.

5.3 Results

5.3.1 Organoid MPS development and implementation

The organoid MPS used in this study was optimized from our previously described fluidic chip (*6*). The original fluidic chip, referred to as the Acry-Chip, was fabricated entirely from PMMA and contained geometric features (i.e., an inlet chamfer and an obstacle) in the flow path designed to optimize convective transport into the culture well (Figure 5.1A). An improved chip design was developed by replacing the PMMA base of the culture well with an oxygen-permeable perfluoroalkoxy (PFA) membrane, referred herein as the Oxy-Chip (Figure 5.1B). Chips were fabricated to the specifications of 3D computer aided design (CAD) models using a subtractive rapid prototyping approach, which utilized a combination of computer numerical control (CNC) micromilling and CO_2 laser cutting. A through-hole was milled into the culture wells and the PFA membrane was

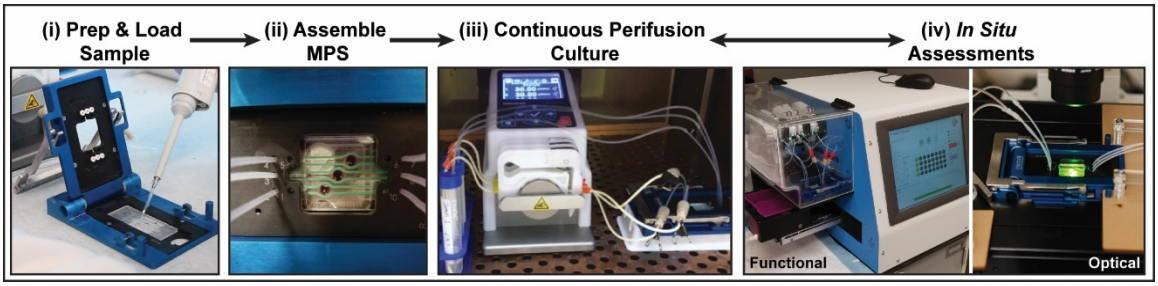

Figure 5.2 Schematic representation of experimental workflow, where (i) organoids and hydrogel are prepared and manually loaded into the wells of the chip, (ii) the chip is sealed and fluidic connections are introduced when the MPS is assembled in the chip holder, (iii) the organoid MPS is placed in an incubator with a pump for continuous perifusion culture, and (iv) the MPS can be temporarily removed from culture to perform a dynamic functional assay or for optical assessment(s).

adhered to the bottom piece (Figure 5.1C). The top piece contained embedded gaskets for sealing the culture wells. The final assembled Oxy-Chip consisted of three independent, fluidically sealed, and optically clear culture niches (Figure 5.1D).

A streamlined workflow was developed to facilitate the implementation of the organoid MPS (Figure 5.2). First, primary islets within a hydrogel matrix were manually loaded into the open culture wells of the bottom chip piece. After placement of the top piece, a commercially available chip holder was used to seal the two pieces and integrate fluidic connections. Each well was then independently perifused with recirculating media using a peristaltic pump in a standard cell culture incubator (37°C, 5% CO_2). For *in situ* functional (i.e., cellular secretion) or optical (i.e., bright field and/or fluorescent) assessment, the fluidic connections and form-factor of the organoid MPS were designed to be compatible with existing laboratory equipment, such as a dynamic perifusion system or a confocal fluorescent microscope.

5.3.2 Characterization of oxygen diffusion within organoid MPS

To characterize the impact of the PFA membrane on oxygen transport into the culture well, the PFA chip was further modified to incorporate fiber optic oxygen sensors to record the partial pressure of oxygen within the culture well (Figure 5.3A-B). The

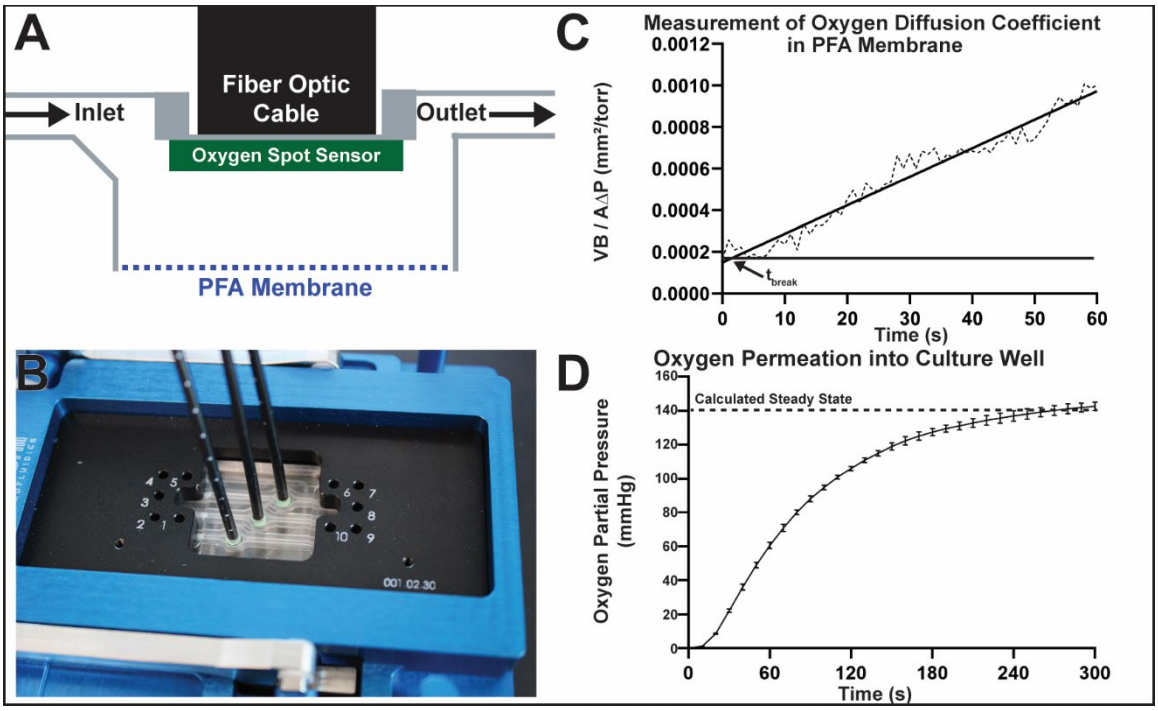

Figure 5.3: Characterization of oxygen permeable PFA membrane. (A) Schematic representation of modified chip that includes oxygen sensors. (B) Fabricated and assembled chip with oxygen sensing hardware. (C) Estimation of oxygen diffusion coefficient in PFA using previously reported methods (*54*). (D) Validation of calculated diffusion coefficient based on oxygen permeability of PFA culture well measured by noninvasive oxygen spot sensors.

diffusion coefficient of oxygen in the PFA membrane was estimated using a previously described method (*94*). Briefly, the measured change in the partial pressure of oxygen (P_{O2}) was converted to an equivalent volume (V):

$$V = \left(\frac{P_{O2}}{P_0}\right)\left(\frac{T_0}{T}\right)V_s$$

Where P_0 is the partial pressure of oxygen at the standard pressure (160 torr), T_0 is the standard temperature (273 K), T is the measurement temperature (292 K) and V_s is the volume of the culture well (217.56 mm^3). The volume of gas (V) that permeates a membrane as a function of time (t) can determined from (*95*):

$$V = P \times A \times P_{app} \times \frac{t}{B}$$

Where P is the permeability coefficient, A is the membrane area (12.57 mm^2), P_{app} is the applied pressure, and B is the membrane thickness (0.0254 mm). Finally, the time

required for oxygen to break through the membrane (t_{break}) can be determined from B and the diffusion coefficient of the membrane (D):

$$t_{break} = \frac{B^2}{6D}$$

The oxygen diffusion coefficient of the 25 μm-thick PFA membrane was approximated to be 5.6×10^{-11} m^2/s (Figure 5.3C). This result was validated by first purging the chip of oxygen and then recording the partial pressure of oxygen (P_{O2}) as it diffused back into the culture well. Using the error function solution to Fick's 1st Law, the theoretical steady-state P_{O2} was calculated and found to be within 1.5% of the experimental steady-state P_{O2} observed after 5 min (Figure 5.3D).

5.3.3 In silico modeling of islet physiology within organoid MPS

The impact of the organoid MPS on cultured hydrogel-embedded islets was first investigated *in silico* using a FEM model of islet physiology (*7*). We hypothesized that continuous perifusion of oxygenated media and the integration of the oxygen-permeable membrane would increase local oxygen supply to the islets, resulting in decreased cellular hypoxia and downstream impacts on insulin secretion. Islets were modeled as a single idealized size (diameter = 150 μm) discreetly distributed into the 3D hydrogel. Three models were developed: i) static culture; and continuous perfusion culture in the ii) Acry-Chip and iii) Oxy-Chip.

A spatially distinct oxygen concentration gradient was observed in each of the culture conditions (Figure 5.4A). For the static model, classic oxygen gradients were observed, with a negative correlation between oxygen concentration and the islet's distance from the surface of the bathing media. In the perifusion culture models, the concentration gradient followed the fluid flow path, where oxygen levels were reduced in the region

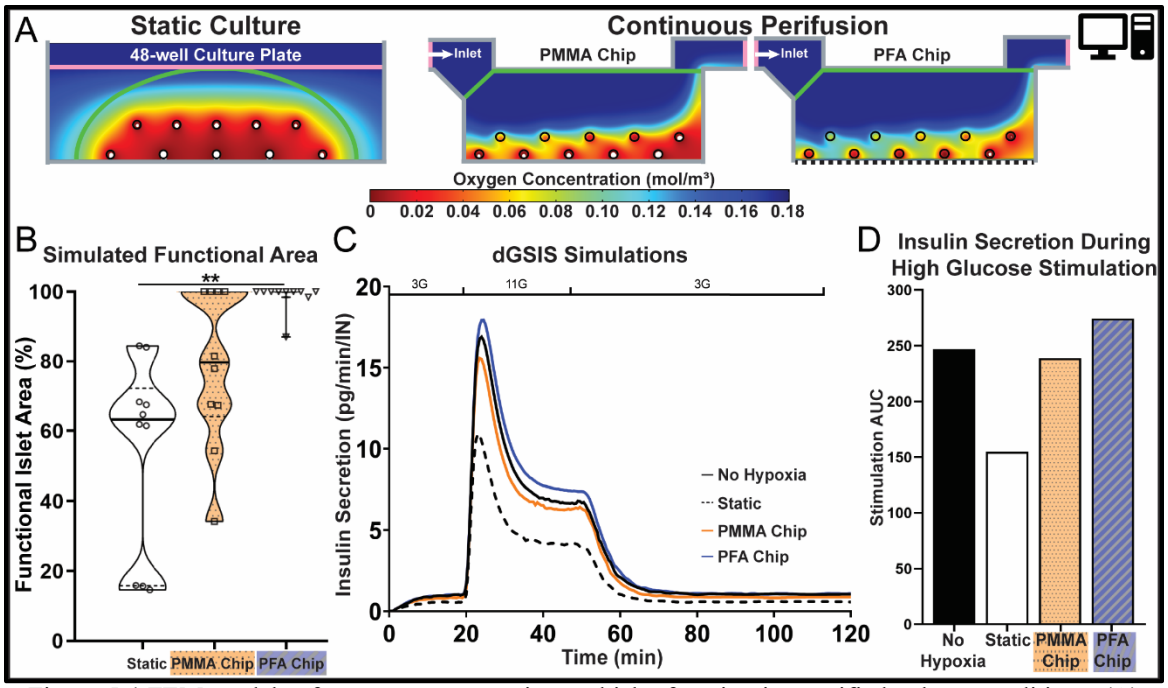

Figure 5.4 FEM models of oxygen concentration and islet function in specified culture conditions. (A) Simulated oxygen concentration profile after 24 h culture in static culture or continuous perifusion culture in either the PMMA or PFA chip. Islets (outlined in black) are embedded in a hydrogel (outlined in green) and cultured in media (outlined in pink). The white area denotes areas of potential dysfunction due to hypoxia ([O2]dys ≤ 5.1 uM). (B) Quantification of functional islet area, defined as percentage of islet region with an [O2] > [O2]dys, predicted by FEM models. The violin plot displays five-number summaries; Statistical analysis by one-way ANOVA (Browne-Forsythe and Welch tests corrected for multiple comparisons using Dunnett T3 approach for N = 10; **P < 0.01). (C) Predicted dGSIS curves for islets after 24 h of culture within each culture system. The No Hypoxia curve represents an ideal insulin secretion profile for healthy islets. Legend at top of graph indicates the glucose concentrations of the bathing media, where G = mM glucose. Insulin secretion is normalized per number of islets (IN) (D) Quantification of predicted total insulin secretion during glucose stimulation from FEM models.

furthest away from the fluidic inlet. The average intra-islet oxygen concentration after 24 h simulated culture was an order of magnitude higher in the Acry-Chip continuous perifusion model (0.02 mol/m^3) when compared to the static model (0.002 mol/m^3). The addition of the oxygen permeable membrane within the MPS (Oxy-Chip) further elevated oxygen delivery, resulting in an additional two-fold increase in average oxygen levels (0.04 mol/m^3).

Acute exposure to hypoxia impairs glucose-stimulated insulin secretion, even though significant cell death might not occur (*96, 97*). To assess potential islet dysfunction due to culture conditions, a hypoxia-induced dysfunction threshold was set at 5.1×10^{-4}

mol/m^3 and the estimated islet functional area following 24 h simulated culture was calculated (*98*). As shown (Figure 5.4B), functional islet area was significantly higher in the Oxy-Chip (98.6 ± 4.1%) than in the static culture model (53.9 ± 27.4%; P = 0.001), while the Acry-Chip was predicted to functionally support an intermediate percentage of islets (78.3 ± 22.7%). Models also predicted a more homogenous distribution of oxygen in the Oxy-Chip, with reduced variability in islet functional area (F-test between the three conditions of P = 0.0002). Simulations of insulin release in response to a high glucose challenge (i.e., dGSIS) further captured culture-induced differences (Figure 5.4C). Under ideal culture conditions (No Hypoxia control), a classic biphasic dGSIS response curve was predicted, with a 1st phase peak insulin release and a 2nd phase plateau during high glucose stimulation (11 mM), followed by a return to basal secretion levels under non-stimulatory glucose (3 mM) (*99*). While islets cultured in Acry- and Oxy-Chip models were predicted to exhibit no major alterations in this dynamic secretion profile, islets within static cultures were substantially suppressed, with an area under the curve (AUC) during high glucose stimulation of only 67% of the No Hypoxia control group (Figure 5.4D). Overall, while the additional parameters of islet size and loading density were not explored in this model, FEM generally predicts that continuous perifusion culture within the Oxy-Chip MPS mitigates islet hypoxic stress within the culture niche, resulting in a positive impact on islet health and function compared to standard static culture conditions.

5.3.4 Serial Assessment of rodent and human islets

An advantage of our MPS is the ability to easily perform sequential functional assessments at multiple time points on the same set of organoids. One of the primary endocrine functions of pancreatic islets is to secrete insulin in response to stimulatory

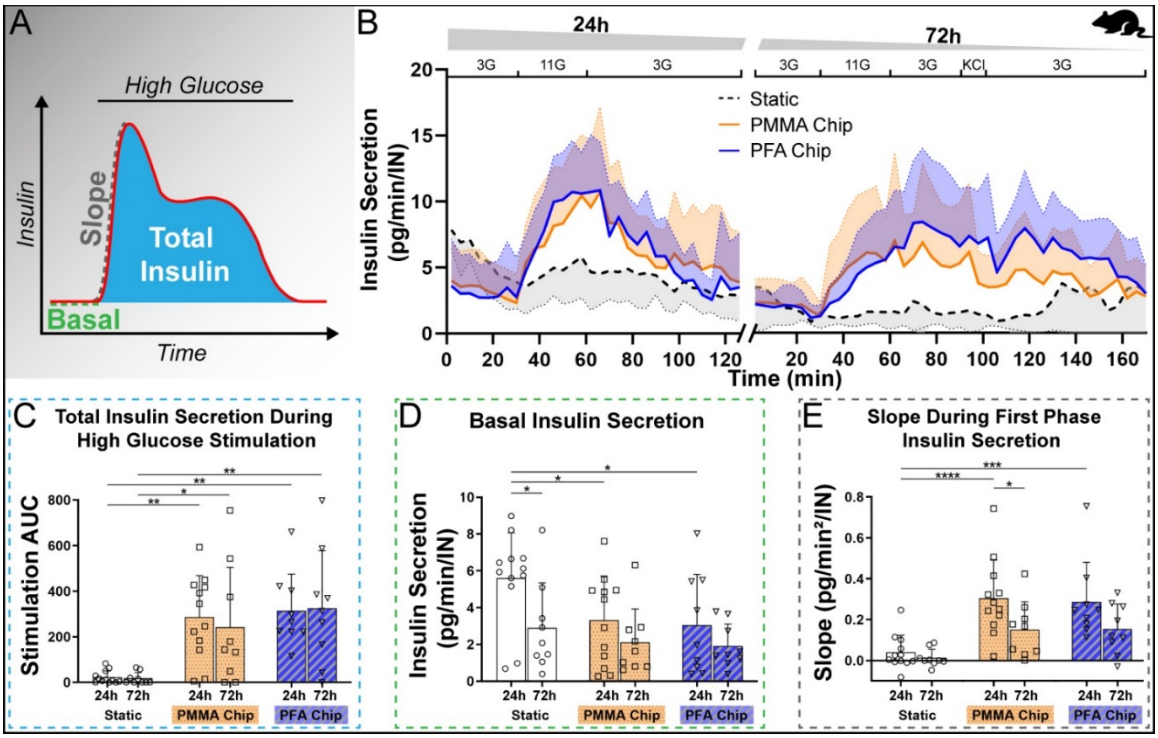

Figure 5.5 Serial dGSIS assessment of functionality of hydrogel-embedded rodent islets cultured in all three conditions. (A) An idealized dGSIS profile denoted with different colors to identify the origin of different matrices. Red = insulin secretion. Cyan = AUC during high glucose stimulation. Green (dashed line) = insulin secretion basal levels. Grey (dashed line) = slope to attain first phase of insulin secretion. (B) dGSIS profiles of rodent islets cultured within islet MPS chips compared to static condition. The islets were assessed for functionality at 24 h, returned back to the incubator for more culture, and assessed for functionality again at 72 h. The shaded area of the dGSIS profiles represents standard deviation values corresponding to its mean. Legend at top of graph indicates the glucose concentrations of the bathing media, where G = mM glucose. (C) Calculated AUC representing total insulin secretion during high glucose stimulation peak. (D) Average basal insulin secretion levels of rodent islets prior to high glucose challenge. (E) Slope of the dGSIS profile between the last basal value and maximum insulin secreted in response to the high glucose challenge. Statistical analysis by two-way ANOVA with mixed-effects model approach (Matching factors; Sidak's multiple comparison to compare between static, PMMA, and PFA chip culture conditions; Tukey's multiple comparison to compare time factor within each culture conditions; assumed sphericity as repeated measures of only two levels; ROUT test with Q = 1% to remove outliers; *P < 0.05, **P < 0.01, ***P < 0.001, ****P < 0.0001). All values displayed as mean ± SD. dGSIS profiles are from more than three rodent islet isolations with N ≥ 9 biological replicates. *Data and figure produced by Smit Patel from the Stabler Lab at the University of Florida.*

glucose levels. A gold standard assessment to evaluate in vitro islet function is the dGSIS assay, where insulin release in response to dynamic glucose changes is measured with respect to time (Figure 5.5A). Specific metrics can be obtained from the insulin secretion profile to characterize islet functionality, such as the basal secretion level, the rate of insulin release following glucose stimulation, and the overall AUC during the glucose challenge. For most dGSIS perifusion systems, islet recovery and culture post-dGSIS is challenging,

as islets are either suspended in a slurry of polyacrylamide beads in perfusion chambers or trapped within permanently sealed MPS platforms (*100, 101*). As such, dGSIS is typically an endpoint assay for a single set of islets. Without such restrictions, our MPS permitted sequential glucose challenging of hydrogel-embedded rodent islets cultured at discreet culture times (24 and 72 h). Average insulin secretion profiles during dGSIS, plotted with respect to time (Figure 5.5B). Curves represent an aggregate from three islet isolations and three independent trials for each isolation. Islets cultured in either the Acry- or Oxy-Chip exhibited robust stimulation profiles in the presence of high glucose, in stark comparison to the minimal responses measured from islets cultured under the static condition for only 24 h. These differences were further exacerbated after 72 h, with complete loss of glucose stimulated insulin secretion for islets cultured in the static condition.

Deeper analysis of dGSIS curves revealed additional differences. Statistical analysis of total insulin secretion, obtained from calculating AUC during high glucose stimulation, found the culture platform to impart a significant effect ($P = 0.0001$; 2-way ANOVA) (Figure 5.5C). The AUC for islets was significantly higher within Acry-Chip or Oxy-Chips, at 12.6- and 13.8-fold larger than static culture controls (Figure 5.5C; $P = 0.0014$ and 0.0011, respectively). After 72 h, similar trends were observed, with the total insulin secretion of islets cultured under Acry-Chip and Oxy-Chip quantified as 13.7- and 18.3-fold higher than static culture ($P = 0.034$ and 0.001, respectively). Comparison of time effects across culture platforms found no significant changes, indicating stability in function over the culture period. Basal insulin secretion levels were significantly impacted by the duration of culture (Figure 5.5D; $P = 0.0045$, 2-way ANOVA). Under non-stimulatory glucose levels, islets cultured overnight under static conditions exhibited 2.44-

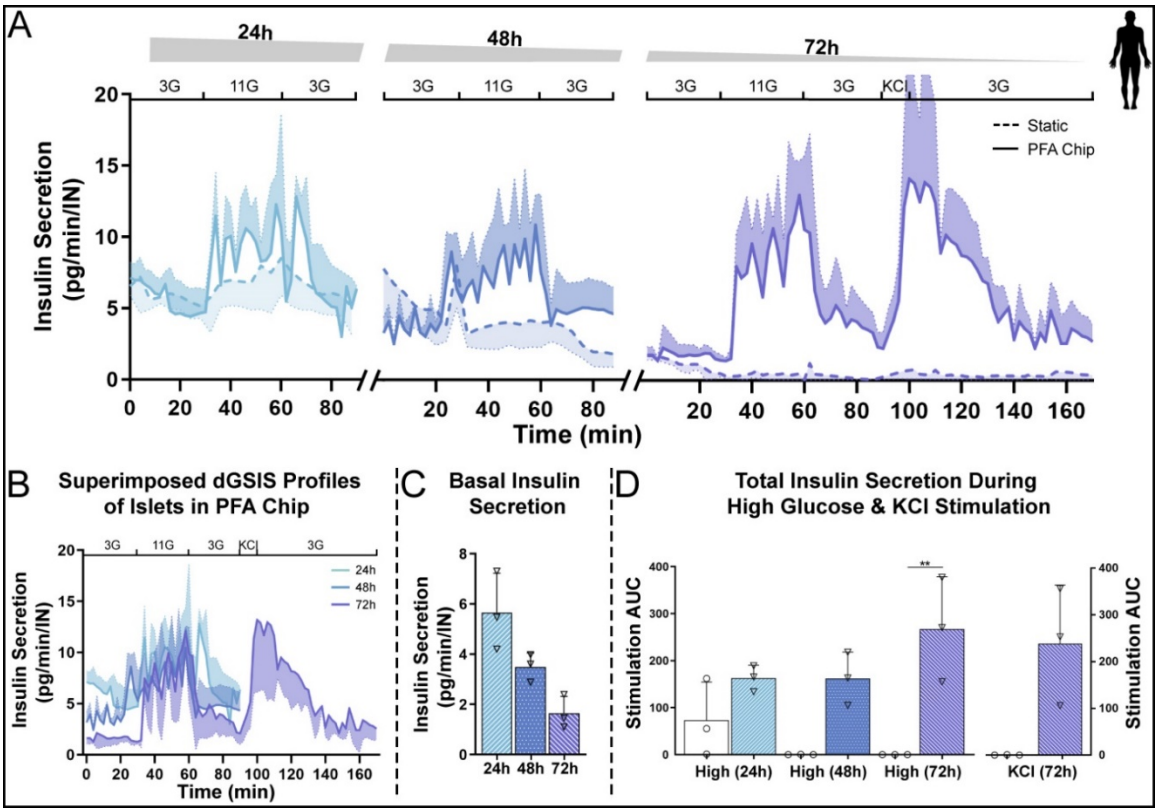

Figure 5.6 Hydrogel-embedded human islets cultured in the PFA chip for up to 72 h with functionality assessments performed at every 24 h. (A) Serial dGSIS assessment of human islets cultured in islet MPS chip and static condition at 24, 48, and 72 h. The shaded area of the dGSIS profiles represents standard deviation values corresponding to its mean. Legend at top of graph indicates the glucose concentrations of the bathing media, where G = mM glucose. (B) Overlaying human islet functional performance within the islet MPS for three consecutive days. (C) Average basal insulin secretion levels of human islets cultured in islet MPS prior to high glucose challenge. Statistical analysis by one-way ANOVA (Browne-Forsythe and Welch tests corrected for multiple comparisons using Dunnett T3 approach for $N < 50$ samples). (D) Calculated AUC representing total insulin secretion during high glucose and KCl stimulation peak(s). High glucose AUC statistical analysis by two-way ANOVA (Tukey's post-hoc pairwise comparison; $^{**}P < 0.01$). KCl AUC statistical analysis by unpaired parametric student t-test with Welch's correction. All values displayed as mean ± SD. dGSIS profiles are from a single islet isolation batch preparation with N = 3 biological replicates. *Data and figure produced by Smit Patel from the Stabler Lab at the University of Florida.*

to 2.20-fold higher insulin secretion, when compared to Acry- and Oxy-Chips (Figure 5.5D), indicating "leaky" beta cells. The efficiency of the islet's functional response to the glucose challenge, captured by analysis of the dGSIS slope following exposure to stimulatory glucose levels, was significantly impacted by both the culture platform and time (Figure 5.5E; P = 0.003 and 0.001, respectively, 2-way ANOVA). Islets cultured under static conditions were non-responsive to the high glucose challenge, resulting in a

close to zero average slope values (0.040 ± 0.084 and 0.013 ± 0.043 pg/min^2/islet at 24 h and 72 h, respectively), in stark contrast to islets cultured in Acry- and Oxy-Chips ($P \leq 0.001$). Furthermore, MPS cultured islets did not exhibit a significantly altered dynamic response to a glucose challenge over the culture period.

Translating this work to human cell sources, the in vitro function of non-diabetic human islets was characterized. Alginate-embedded human islets were cultured in the perfused Oxy-Chip or standard conditions for 72 h, with functional assessments performed at 24, 48, and 72 h. Human islets in 3D alginate hydrogels cultured in static conditions rapidly lost their capacity to respond to a glucose challenge, exhibiting a nonfunctional dGSIS profile after only 24 h culture (Figure 5.6A). Contrarily, human islets in the Oxy-Chip showed robust responsiveness to high glucose exposure, with a return to basal insulin secretion levels after termination of the glucose challenge (Figure 5.6A). In fact, superimposing the human islet MPS dGSIS profiles over the course of 72 h (Figure 5.6B) visually illustrates retention in insulin secretion during the high glucose challenge and statically significant global reduction in the average basal insulin levels over the culture period (Figure 5.6C; $P = 0.034$, 2-way ANOVA). Total insulin secretion, as measured by stimulation AUC, was significantly affected by the culture platform ($P < 0.0001$, 2-way ANOVA), with a marked increase in total insulin secretion for human islets cultured in the MPS (Figure 5.6D). Collectively, the functional output of human islet organoids in a 3D matrix during in vitro culture was preserved by our custom Oxy-Chip platform.

5.4 Discussion

Our MPS platforms, both the Acry-Chip and Oxy-Chip, supported the prolonged survival of perfused 3D organoids within hydrogel matrices, while also permitting ease in

longitudinal (serial) functional cellular assessments. Replacing the commonly used PDMS with PMMA as the base fabrication material avoided many of the critical challenges faced in using PDMS-MPS for drug screening or long-term organoid culture, such as problems with accurate large-scale manufacturing and biofouling (*30, 102*). While others have also made this transition using polycarbonate (*103*) , long-term microfluidic culture using plastic based MPS is challenged by the poor oxygen permeability of these materials (*104*). We address this issue by integrating a PFA membrane, an oxygen-permeable and low biofouling perfluorinated polymer, into the acrylic MPS platform (*33, 105*). The PFA membrane facilitates oxygen transport at the cell culture niche, while retention of PMMA as the primary fabrication material ensures a robust and stable framework suitable for largescale manufacturing.

Islet functional assessments correlated with results from the computational models. Human and rodent hydrogel-embedded islets exhibited nonfunctional insulin release profiles after static culture overnight. This precipitous loss of function is attributed to significant oxygen deprivation, as well as apoptotic-induced islet dysfunction, and highlights the challenges of culturing these primary organoids within 3D hydrogels using conventional culture systems (*106*). In stark contrast, our MPS platform retained robust glucose-stimulated insulin secretion for both human and rat islets over the entire three-day culture period. MPS-cultured islets also exhibited decreased basal insulin secretion when compared to static conditions. As elevated insulin release under non-stimulatory glucose conditions has been attributed to β cell stress, typically induced via hypoxia or inflammatory cytokines, the capacity of our MPS to decrease basal levels during extended culture highlights the benefits this MPS niche on supporting islet health (*107, 108*).

Further investigation into rodent dGSIS profiles during MPS culture did exhibit some features divergent from an ideal stimulatory trace. For example, a classic biphasic insulin secretion profile was not observed for rat islets. This is likely due to the combination of insufficiently stimulatory glucose levels, blunting of the first-phase response due to the additional flow barrier imposed by the hydrogel, and the 3- to 30-fold lower perifusion rates employed during this dGSIS study (*7, 11, 100, 109, 110*). Furthermore, after 72 hours of continuous culture, rat islet insulin secretion post-high glucose stimulation did not fully return to its original basal levels. This feature indicates early islet stress due to ionic channel leakage or accumulated reactive oxygen species (*111, 112*). Thus, future studies will identify the ideal glucose levels and flow rates needed to optimize effluent insulin release, as well as explore other hydrogels that may decrease any biomaterial-induced dampening. Islet culture media will also be screened, as recent work indicates this plays a significant role in long-term *ex vivo* islet survival (*113*). These features can be easily manipulated within the modular operational workflow of the islet MPS.

Of interest, dGSIS profiles of human islets cultured in hydrogels under continuous perifusion exhibited pulsatile insulin secretion, a phenomenon not observed in the rodent islets used in this study. Rodent, canine, nonhuman primate, and human islets are reported to generate pulsatile insulin secretion that is primarily driven by calcium oscillations, although this is a highly debated topic (*114-116*). The lack of an oscillatory secretion profile for rodent islets may again be attributed to the glucose concentrations used in this study, as rodent islets may need to be stimulated in the range of 16 – 28 mM glucose to observe these fluctuations (*109, 115*). To our knowledge, the oscillatory nature of insulin secretion in human islets within hydrogels has not been previously reported. These results

highlight the potential of our MPS to capture a highly sensitive physiological phenomenon, as well as its capacity to spatiotemporally track islet function from the same set of islets. Thus, future work will serve to synchronize dGSIS with calcium imaging to further explore this phenomenon.

Acry-Chip and Oxy-Chip MPS platforms described herein provide a distinct portfolio of capabilities not available in other platforms, specifically long-term culture, controlled and dynamic perifusion, serial assessments during extended culture, and ease of sample retrieval. For example, acute multimodal characterization of islets has been reported, but devices used lack long-term culture capabilities and ease of cell retrieval for off-chip assessments (*100, 110*). Complex platforms, like the Mimetas Organoplate, supports 3D cell culture within hydrogel matrices and assessment via optical assays, but their passive perifusion mechanism limits dynamic secretion assays (*117-119*). The TissUse 2-Organ-Chip was utilized to couple pancreatic islet microtissues and liver organoids (*120*); however, functional assessment of islets was performed off-chip and the system did not include a 3D hydrogel matrix. Currently our platform is limited by its three-channel form-factor, therefore future platform development will focus on increasing throughput without sacrificing ease of use.

CHAPTER 6

Modular, PDMS-free Microphysiological System for In Vitro Modeling of Biologic Barrier Function

6.1 Overview

Microphysiological systems (MPS), commonly referred to as organs-on-chips or tissue chips, have emerged as a novel approach to create *in vitro* models of normal and disease physiology. By incorporating human cells into microfluidic devices that recapitulate dynamic *in vivo* stimuli, MPS have promised to address the high attrition rate of compounds in drug development by providing a more human-relevant tool to identify therapeutic targets and assess drug toxicity (*5*). The rapid development of MPS has been greatly influenced by the widespread use of polydimethylsiloxane (PDMS) as a biocompatible material for microfluidic devices (*25, 26, 121*). PDMS demonstrated a number of advantages for early biological applications, including low cytotoxicity, optical transparency, gas permeability, and ease of microfabrication (*28*). One of the earliest MPS, a lung-on-a-chip, validated PDMS for applications that involve recreating the dynamic flow and mechanical stretching of the *in vivo* alveolar air-liquid interface (ALI) (*27, 122*). However, the implementation of MPS has been hampered by some of the innate properties of PDMS (*104*). Of these drawbacks, the adsorption of hydrophobic compounds and leaching of uncrosslinked oligomers have provided the greatest hinderance to the adoption of PDMS-based MPS in the context of drug discover assays (*30*).

Due to the long history of microfluidic technology, there is extensive literature on the fabrication and use of plastic microfluidic devices, which may serve as an alternative to PDMS for microphysiological systems (*32, 34*). Poly(methyl methacrylate) (PMMA), a transparent thermoplastic, is not only amenable to a number of microfluidic fabrication

techniques, but also highly biocompatible and less absorptive than PDMS. Previously, we have demonstrated the feasibility of a PMMA fluidic platform for biologic applications through the functional assessment and optogenetic control of pancreatic islets (*6*). However, designing fluidic channels to recapitulate *in vivo* barriers, such as the alveolar ALI or glomerular filtration barrier (GFB), while maintaining a resealable format is difficult due to the limitations of the subtractive rapid prototyping (SRP) technique employed to fabricate PMMA-based MPS.

Here, we have overcome this limitation and engineered a modular MPS using PMMA to recapitulate the *in vivo* microenvironment of biologic barriers. The two-part microfluidic chip is comprised apical and basal channels separated by a removable porous membrane. We demonstrate that static co-culture models of the lung alveolar air liquid interface (ALI) and GFB can be transferred to the MPS and exposed to physiomimetic dynamic stimuli. This approach aims to simplify cell culture and seeding methods within the microfluidic device and minimize the time to achieve functional constructs within the MPS.

6.2 Materials and Methods

6.2.1 Design and fabrication of PDMS-free microfluidic device

The fluidic chip design, which is analogous to many organ-on-chip devices, was developed to house an epithelial/endothelial cellular co-culture, supported by a porous membrane, between independent flow channels. Apical and basal flow channels were incorporated into a two-part, resealable form-factor, based on our previously published platform for interrogation of pancreatic islets. Computer-aided design (CAD) software

(SolidWorks, Dassault Systèmes) was used to generate three-dimensional parts and assemblies of the fluidic chip design.

Subtractive rapid prototyping (SRP) of CAD designs was used to fabricate fluidic chips. Briefly, device features were milled from optically-clear, UV-resistant acrylic (0.125" thick, McMaster-Carr) using a computer numerical control milling machine (MODELA MDX-540, Roland). A 30W CO2 laser machine (Legend Helix, EpilogLaser) was used to laser cut the final form-factor of the chip from the milled workpieces (Figure 1C). Unlike additive manufacturing approaches, SRP does not enable the fabrication of closed, hollow channels. As a result, the basal flow channel must be sealed after milling. This was achieved by bonding a fluoropolymer membrane to the underside of the bottom piece using a silicone adhesive.

Custom gaskets were fabricated using a two-part silicone epoxy (Duraseal 1533, Cotronics Corp.). To improve the ease and speed of assembly, the gaskets were bonded to the top piece of the fluidic chip using a 100μm thick differentially-coated polyester adhesive film (PS-1340, Polymer Science). The fully fabricated fluidic chip is then clamped in a chip holder (Fluidic Connect PRO, Micronit) to create a fluidic seal and introduce tubing connections.

6.2.2 Flow profile characterization

The fully fabricated fluidic chip is clamped in a chip holder (Fluidic Connect PRO, Micronit) to create a reversible fluidic seal and introduce tubing connections. Two microfluidic pressure pumps (Flow-EZ, Fluigent) were used to independently provide flow to the apical and basal flow channels. Flow rate was continuously measured at the outlet

of the fluidic chip using liquid flow meter microsensor (LG16, Sensirion). The average flow rate was calculated from 60s recordings at pressures ranging from 0 to 150 mbar. From flow rate measurements, the fluid shear stress (τ) on the apical and basal sides of the membrane was calculated using the following equation:

$$\tau = \frac{6\mu Q}{bh^2}$$

where μ is the fluid viscosity, Q is the volumetric flow rate, b is the width at the center of the culture well, and h is 0.5 mm, the height of the culture well. In the present design, the width of the culture well for the apical and basal flow channels was 6 mm and 4.5 mm, respectively, and the height of the channels.

6.2.2 Computational fluid dynamics

Computational modeling of fluid dynamics was performed using the FEM software, COMSOL Multiphysics 5.0. Three-dimensional models of the fluidic channels were imported into COMSOL from SolidWorks as a Parasolid file. The Free and Porous Media Flow physics module was used to solve for velocity and pressure fields of single-phase flow in the channels and the porous membrane separating the channels, simultaneously. Fluid flow was modeled as the incompressible flow of water (density = 1000 kg/m^3 and dynamic viscosity = 0.001 Pa·s) governed by the Navier-Stokes and Brinkman equations. The permeability parameter of the membrane was approximated based on the hydraulic-electrical circuit analogy (*123, 124*). This approach is based on the similarities of Hagen-Poiseuille's law for fluid flow and Ohm's law for electrical current flow. Assuming each pore of the membrane is a circular pipe, the fluidic resistance of a single pore (R_{pore}) can be calculated:

$$R_{pore} = \frac{8\mu L}{\pi R^4}$$

Where μ is the viscosity of the fluid, L is the thickness of the membrane, and R is the radius of the pore. The fluidic resistance of the whole membrane (R_{memb}) can then be calculated from the area (A) and porosity (ρ_{pore}) of the membrane:

$$R_{memb} = \frac{R_{pore}}{A\rho_{pore}}$$

Using Ohm's law and the above equations, the permeability parameter (k) can then be expressed as a function of the porosity and pore radius:

$$k = \frac{\pi\rho R^4}{8}$$

A stationary solver was implemented to determine the steady state solution of the velocity and pressure fields. Flow rates were derived from the 3D computational models by taking the surface integral of the velocity field across specific regions.

6.2.4 Characterization of membrane strain

Bi-axial strain applied to the membrane was calculated based on the membrane deflection due to applied pressure. Membrane deflection was measured using the perfect focus system on a TI-Eclipse microscope (Nikon). First, the pump for basal flow channel was set to 80mbar to perfuse phosphate buffered saline through the basal channel. Next, the initial focal distance of the center of the membrane was recorded. Then, the pressure for the apical flow channel pump was increased from 0mbar to 315mbar in 15mbar increments. The focal distance at each applied pressure was recorded and membrane deflection was calculated as the change from the initial focal distance. The surface of the area of the membrane could then be calculated by assuming a semi-ellipsoid geometry:

$$SA = 2\pi * \frac{(a*b)^{1.6075} + (a*c)^{1.6075} + (b*c)^{1.6075}}{3}^{\frac{1}{1.6075}} + (\pi * b * c)$$

Where a is the membrane deflection and b and c are the major and minor semi-axes, respectively. Based on the change of surface area, the bi-axial surface expansion (ε_{SA}) can be calculated (*125*):

$$\varepsilon_{SA} = \frac{SA_f - SA_0}{SA_0}$$

Where SA_0 is the initial surface area of the membrane when no pressure is applied and SA_f is the surface area of the membrane calculated based on the membrane deflection.

6.2.5 TEER measurement

Integrity of the cellular layers was assessed by transendothelial/transepithelial electrical resistance (TEER) during static culture on transwells. Resistance measurements were obtained using an epithelial volt/ohm meter (EVOM2, World Precision Instruments) equipped with handheld chopstick electrodes (STX2, World Precision Instruments). To avoid variability in measurements, test samples were brought to room temperature and electrodes were held in place using a universal probe stand. TEER values were obtained using the Ohm's Law Method (*126*). Briefly, the resistance of the cellular layer (R_{cells}) first calculated:

$$R_{cells} = R_{meas} - R_{blank}$$

Where R_{meas} is the resistance measurement of the sample, and R_{blank} is the resistance measurement of a transwell membrane without cells. Then the TEER value was calculated by:

$$TEER = R_{cells} \times M_{area}$$

Where M_{area} is 0.336cm^2, the area of the transwell membrane.

6.2.6 Culture of alveolar-capillary interface

Human alveolar epithelial cells (AECs, ATCC) were propagated according to the manufacturer's instructions in ATCC Modified RPMI1640 (ThermoFisher). Human lung microvascular endothelial cells (LMECs, Lonza) were cultured in EGM2 with the manufacturer's supplements.

Recapitulation of the alveolar-capillary interface was achieved by generating an air-liquid interface (ALI) co-culture of AECs and LMECs using methods previously described, with minor modifications (*27, 121*). Briefly, transwell inserts with 0.4μm pores (Greiner Bio-One), were coated with fibronectin (Sigma), diluted to 5μg/mL. LMECs and AECs were seeded on inserts as described for GFB co-culture. On day 3 of the co-culture, the media for the AECs was supplemented with 1μM dexamethasone. Once cells were confluent, after about 7 days, ALI was induced and the media in the lower compartment was changed to a 50/50 mix of EGM2 and ATCC Modified RPMI supplemented with 1μM dexamethasone.

6.2.7 Podocyte culture

Conditionally immortalized human podocytes (CiPodos) were cultured as previously described, with minor modifications (*127*). Briefly, CiPodos were propagated on collagen-coated flasks in permissive conditions (33°C, 5% CO_2) in RPMI1640 media supplemented with penicillin, streptomycin, insulin, transferrin, selenium, and 10% fetal bovine serum.

6.2.8 Endothelial cell culture

Human umbilical vein endothelial cells (HUVECs, Lonza) and human glomerular microvascular endothelial cells (GMECs, Cell Systems) were cultured in Endothelial Cell

Growth Media 2 (EGM2, PromoCell) with the manufacturer's supplements. Cells were propagated on collagen-coated flasks in a standard cell culture incubator (37°C, 5% CO_2)

6.2.9 Glomerular filtration barrier co-culture

Recapitulation of the glomerular filtration barrier (GFB) was achieved by co-culturing CiPodos and GMECs on opposite sides of transwell insert with 3µm pores (Greiner Bio-One). First, inserts were coated with collagen type I from rat tail (Corning) diluted to 0.1 mg/mL. Then, inserts were inverted and GMECs were seeded on the underside of the insert at a density of 50,000 cells per insert. The inverted inserts were then incubated for approximately 2 hours to allow for GMECs to adhere. Finally, the inserts were placed in a 24-well culture plate and CiPodos were seeded in the upper compartment at a density of 50,000 cells per insert. Cells were fed with their respective media every other day.

6.2.9 Filtration assay

For the filtration assay, membranes were cut from their supports after 7 days of culture at 37°C and bonded into a microfluidic device. Two microfluidic pressure pumps (Fluigent, Flow-EZ) were used to drive flow and generate a physiomimetic pressure gradient for 1 hour. A pressure of 80 mbar (approximately 60 mmHg) was applied to the basal flow channel and 20 mbar (approximately 15 mmHg) was applied to apical flow channel to perfuse PBS through the system. The basal flow channel was supplemented with 100 µg/mL FITC-conjugated inulin (Sigma-Aldrich, F3272) and/or 2 mg/mL bovine serum albumin (Sigma-Aldrich, A2153). The concentration of albumin was measured in the outflow from each channel based on the absorbance at 280 nm using a NanoDrop UV-Vis Spectrophotometer (ThermoFisher Scientific). The fluorescence intensity of inulin in the

outflow from each channel was measured using a multimode microplate reader (Beckman-Coulter, DTX 880). The amount of albumin or inulin filtered from the basal channel to the apical channel was calculated using the equation for renal clearance (*128*):

$$Urinary\ Clearance = ([A] \times AV)/[B]$$

Where $[A]$ = concentration in apical outlet, AV = apical volume collected, and $[B]$ = concentration in basal outlet. Filtration of albumin and inulin was normalized to the filtration observed on a blank membrane without cells.

6.2.10 Sphingolipid exposure

The ability of podocyte cultures to filter albumin and inulin was assessed after a 1-hour exposure to sphingosine-1-phosphate (S1P). As a control, podocyte cultures not exposed to S1P were also assessed for filtration function. To expose podocytes to S1P, culture media was replaced with RMPI media supplemented with 5 μM S1P, obtained from Alla Mitrovanova from the Fornoni Lab at the University of Miami Miller School of Medicine, 1 hour prior to cutting membranes from the supports for bonding into the MPS for filtration assay.

6.3 Results

6.3.1 Development of modular, PDMS-free MPS

The design of the fluidic chip used in our modular platform, which is analogous to many PDMS-based organs-on-chips, was developed to house an epithelial/endothelial cellular co-culture (Figure 6.1A). Using a three-dimensional (3D) computer-aided design (CAD), a model of the chip was developed to scale to ensure the top and bottom pieces of the chip were compatible and that a porous membrane support would fit in to the culture well (Figure 6.1B). Unlike additive fabrication methods, such as 3D printing, the

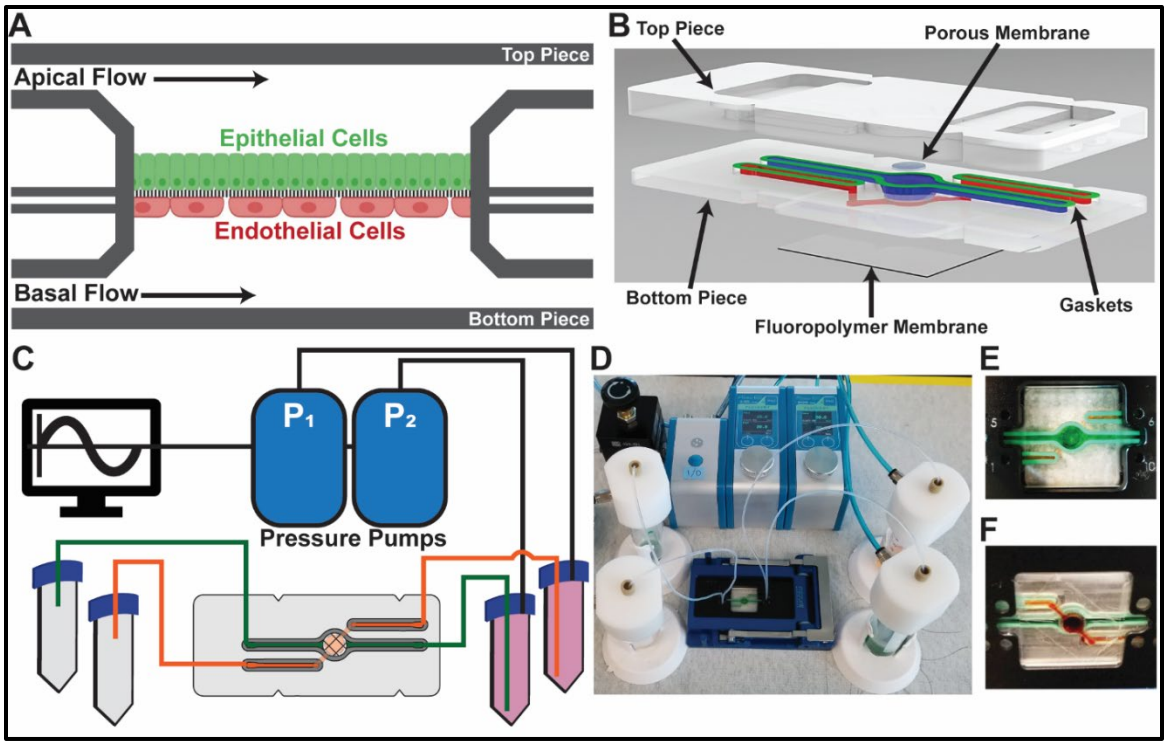

Figure 6.1 Design of modular, PMMA fluidic chip. (A) Schematic illustration of two-piece chip design with apical and basal flow channels and well for epithelial/endothelial co-culture. (B) 3D CAD render of fluidic chip assembly. When clamped between the top and bottom pieces, the gaskets (green) provide a resealable fluidic seal. The porous membrane serves as both a support for cellular co-cultures and a barrier between the apical and basal flow paths. The fluoropolymer membrane not only closes the basal flow channel, but also allows for oxygen transport into the culture area. (C) Schematic representation of the MPS comprised of two pressure pumps controlled by a computer, media reservoirs, and the microfluidic chip. (D) Fully assembled and running MPS. (E) Top and (F) Bottom view showing leak-free perfusion of dyed water through the microfluidic chip.

subtractive rapid prototyping (SRP) approach makes fabrication of closed channels in the z-direction difficult. With PDMS-based organs-on-chips, irreversibly bonding two pieces of PMDS is a common solution to create closed fluidic channels. To maintain resealable form-factor of the chip design, the basal flow channel was closed by adhering a fluoropolymer membrane to the underside of the bottom piece. This membrane not only provides a thin, clear window for optical access, but also enables gas permeability in the culture well of the chip.

To recapitulate the dynamic stimuli that occur *in vivo*, the organ-on-chip platform were modular pneumatic microfluidic pumps implemented to drive flow. Using the

microfluidic automation tool software, the pumps can generate physiomimetic waveforms that drive independent perfusion of the apical and basal flow channels (Figure 6.1C). To validate the design of the modular organ-on-chip platform, the fluidic chip was tested for leaks. Using a commercially available chip holder, the fluidic chip could be sealed and easily connected to the media reservoirs (Figure 6.1D). Both the apical and basal flow channels were observed to operate without leaks (Figure 6.1E-F).

6.3.2 Characterization of flow profile

In vivo, vascular flow is often much faster than interstitial flow. This exposes endothelial cells to high shear stress flow, while epithelial cells experience much less shear stress. To be able to model this phenomenon, we sought to determine the fluid shear stress at the apical and basal boundaries of the membrane separating the two fluidic channels.

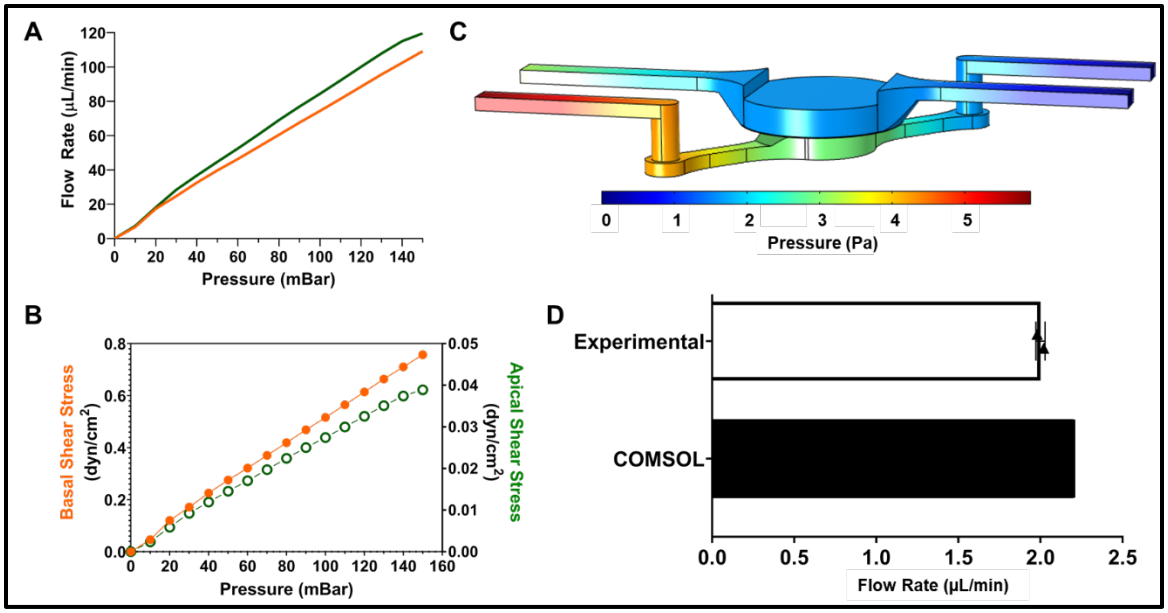

Figure 6.2 Characterization of fluid dynamics in MPS. (A) Relationship between flow rate and pressure in the apical and basal flow channels. The slightly higher flow rates in the apical channel can be attributed to reduced fluidic resistance due geometrical differences between the apical and basal culture wells. (B) Calculated shear stress on the apical and basal membrane surfaces assuming to be a rectangular cross-section. Again, the difference in dimensions between the apical and basal culture wells resulted in about an order of magnitude difference in calculated shear stress. (C) 3D volume view of steady state pressure field in MPS at 100 µL/min inlet flow rate in the apical and basal channels. (D) Fluid flow rate through the membrane separating the apical and basal flow channels determine experimentally and computationally using COMSOL.

This was achieved by first characterizing the flow rate as a function of the applied pressure. As expected, based on the electronic-hydraulic analogy, a linear relation between flow rate and applied pressure was observed (Figure 6.2A). This can be attributed to the constant fluidic resistance of the channels and the constant applied pressure. Interestingly, the flow rate in the apical channel was slightly higher than the flow rate in the basal channel, due to the larger channel geometry. The resulting shear stress at the surface of the membrane, on the other hand, was about an order of magnitude larger in the basal channel than the wall shear stress calculated in the basal channel (Figure 6.2B). This difference can again be attributed to the differences in the size of the apical and basal flow channels.

Based on these results, it was hypothesized that a pressure gradient would develop across the membrane between the two fluidic channels. A 3D computational model of the velocity and pressure fields within the microfluidic device at 100 µL/min, implemented in COMSOL, confirmed this (Figure 6.2C). The stationary solver calculated the velocity and pressure fields in 129 seconds using a normal physics-controlled mesh consisting of 262874 elements. The increased hydrostatic pressure in the basal channel suggests that ultrafiltration should occur within the device. By computing the surface integral of the velocity profile at the membrane surface, a flow rate of 2.21 µL/min was observed in the computational model. This result was confirmed experimentally by comparing the volume change in the apical and basal reservoirs after continuous perfusion overnight. In this setup, a peristaltic pump was implemented to recirculate fluid, ensure a constant flow rate, and mimic steady state conditions (Figure 6.2D).

6.3.3 Modeling the alveolar ALI microenvironment

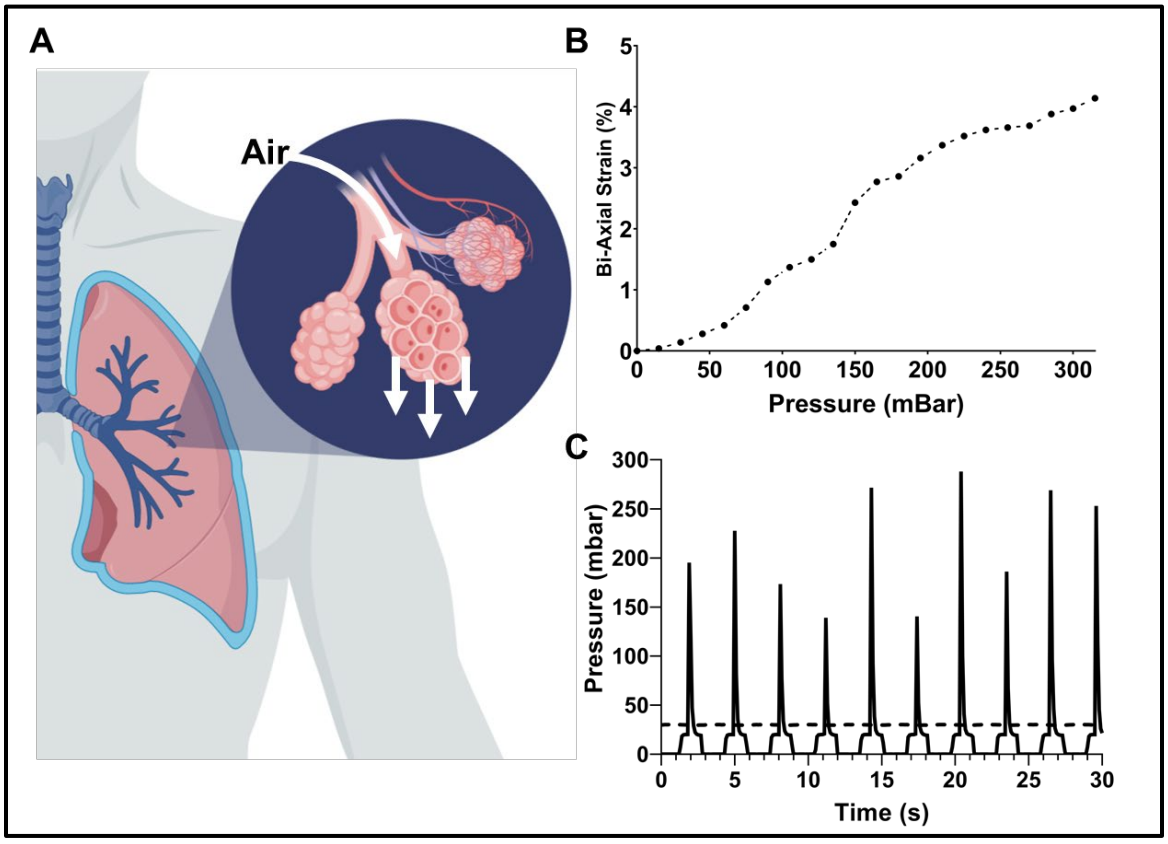

Figure 6.3 Recapitulating alveolar microenvironment (A) Cartoon representation of the expansion of the lung alveolus due to inhalation of air. (B) Bi-axial strain applied to blank membrane with air in the apical channel and PBS in the basal channel to mimic mechanical stress of alveolar ALI. (C) Cyclic application of pressure to the apical channel to mimic breathing at 20 breaths per minute.

An advantage the modular MPS design, is the ability to model multiple *in vivo* microenvironments without significantly altering the device. To demonstrate this, we first sought to recapitulate the ALI found at the alveolar-capillary barrier in the lungs. A key feature of the alveolar microenvironment is the cyclic stretching of the alveolar capsule (Figure 6.3A). To demonstrate the ability to recapitulate the alveolar microenvironment, aimed to characterize the mechanical stretching of the membrane. By perfusing the basal flow channel with phosphate buffered saline (PBS) and applying air pressure through the apical pneumatic pump, it was observed that deflection of the porous membrane in the chip was proportional to the pressure applied. From the measured membrane deflection, bi-axial

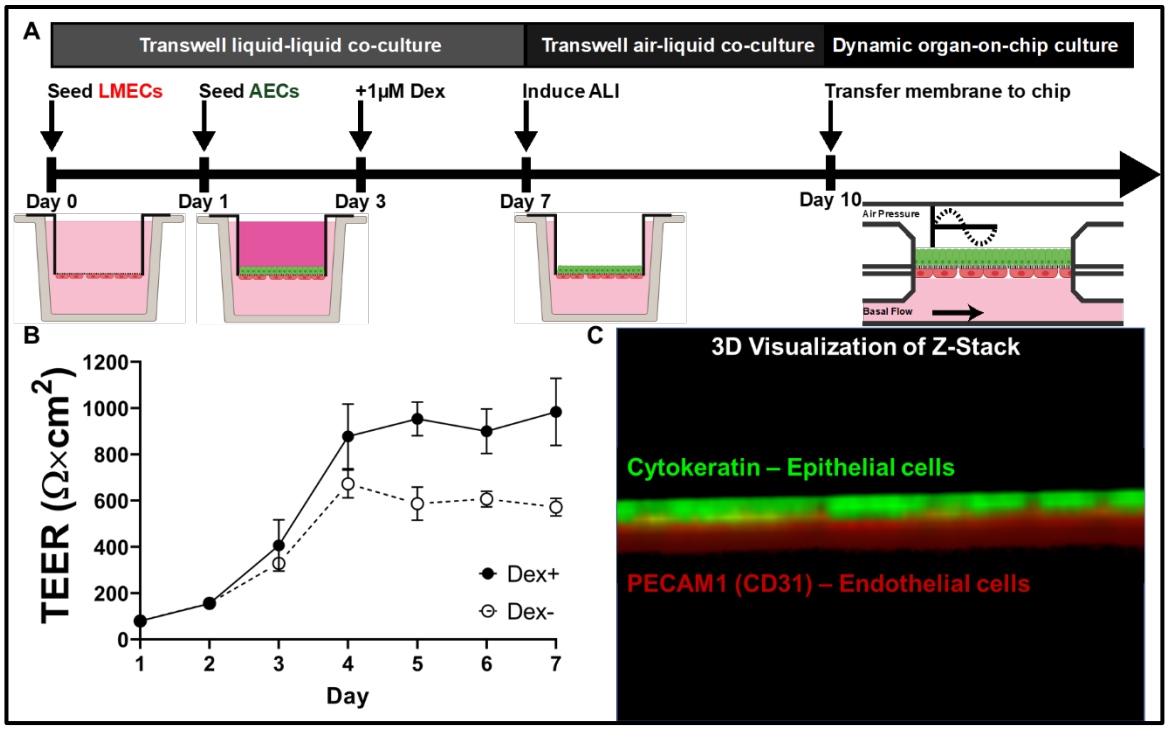

Figure 6.4 Modeling ALI in MPS. (A) Schematic representation to generate and transfer ALI co-culture. (B) TEER recording of co-culture with (Dex+) and without (Dex-) dexamethasone before inducing ALI. (C) 3D visualization of z-stack after 24 hr of dynamic culture in MPS.

strain could be calculated by assuming a semi-ellipsoid shape of the deformed membrane (Figure 6.3B). The maximum bi-axial strain applied to the membrane without cells was just 4%, slightly lower than 4%-12% linear strain thought to occur *in vivo* at the alveolar ALI (*125*). To model the cyclic breathing cycle, a sine wave with an amplitude of 345 mbar and a frequency of 0.33 Hz, corresponding to 20 breaths per minute, was generated in the apical flow channel while the basal flow channel pressure remained constant. The rapid switching of pressure resulted in a pressure profile resembling a human breathing profile more than a sine wave (Figure 6.3C).

Next, an ALI co-culture of lung endothelial and epithelial cells was incorporated in the MPS. Recapitulation of the alveolar-capillary interface was achieved by generating an air-liquid interface (ALI) co-culture of AECs and LMECs using methods previously described, with minor modifications (Figure 6.4A) (*27, 121*). TEER measurements were

recorded during the transwell liquid-liquid co-culture (Day 0 to Day 7). Following the addition of dexamethasone on Day 3, an increase in electrical resistance was observed (Figure 6.4B). This is can be attributed to increased mucus production, due to the role of dexamethasone in mucin production (*129*). On Day 10, ALI co-cultures were transferred into the MPS and cultured under cyclic application of air pressure. Staining for the epithelial and endothelial cells demonstrated that both cells types survived on the MPS under physiomimetic culture conditions (Figure 6.4C).

6.3.4 Functional modeling of the glomerular filtration barrier

To validate that the microfluidic device can recapitulate a functional biologic barrier, a model of the GFB was developed and assessed for albumin filtration. A co-culture of CiPodos and GMECs was established using a permeable membrane cell culture insert (Figure 6.5A). CiPodos were first seeded on the apical side of the membrane and cultured for 48 hours under permissive conditions (33°C, 5% CO_2). GMECs were then seeded on the basal side of the membrane and the co-culture were shifted to standard culture conditions (37°C, 5% CO_2).

During the static culture in standard conditions, the integrity of the cellular layers was monitored through TEER measurements (Figure 6.5B). TEER measures the electrical resistance across cellular layers to confirm integrity of tight functions prior to evaluation of permeability to specific molecules (*126*). Under standard culture conditions, the CiPodos become terminally differentiated and stop proliferating. As a result, very little change is observed in the podocyte only TEER measurements. On the other hand, GMECs proliferate under standard culture conditions and develop tight junctions as the cell layer becomes more confluent. Therefore, a larger increase in TEER is observed over the course of the

culture. As expected, the largest increase in TEER was observed in the co-culture of CiPodos and GMECs. However, the final TEER measurement of the co-culture was just slightly higher than the TEER measurement of GMECs only. This suggests that the endothelial cells are the primary contributor to tight junction formation.

To assess the ability of the co-culture model to recapitulate the physiological function of the GFB, an albumin filtration assay was performed. Physiomimetic pressure driven flow was applied to perfusion PBS through the device for 1 hour. To recreate the hydrostatic pressure of the glomerular microenvironment, 80 mbar (approximately 60 mmHg) was applied to the basal flow channel and 20 mbar (approximately 15 mmHg) was

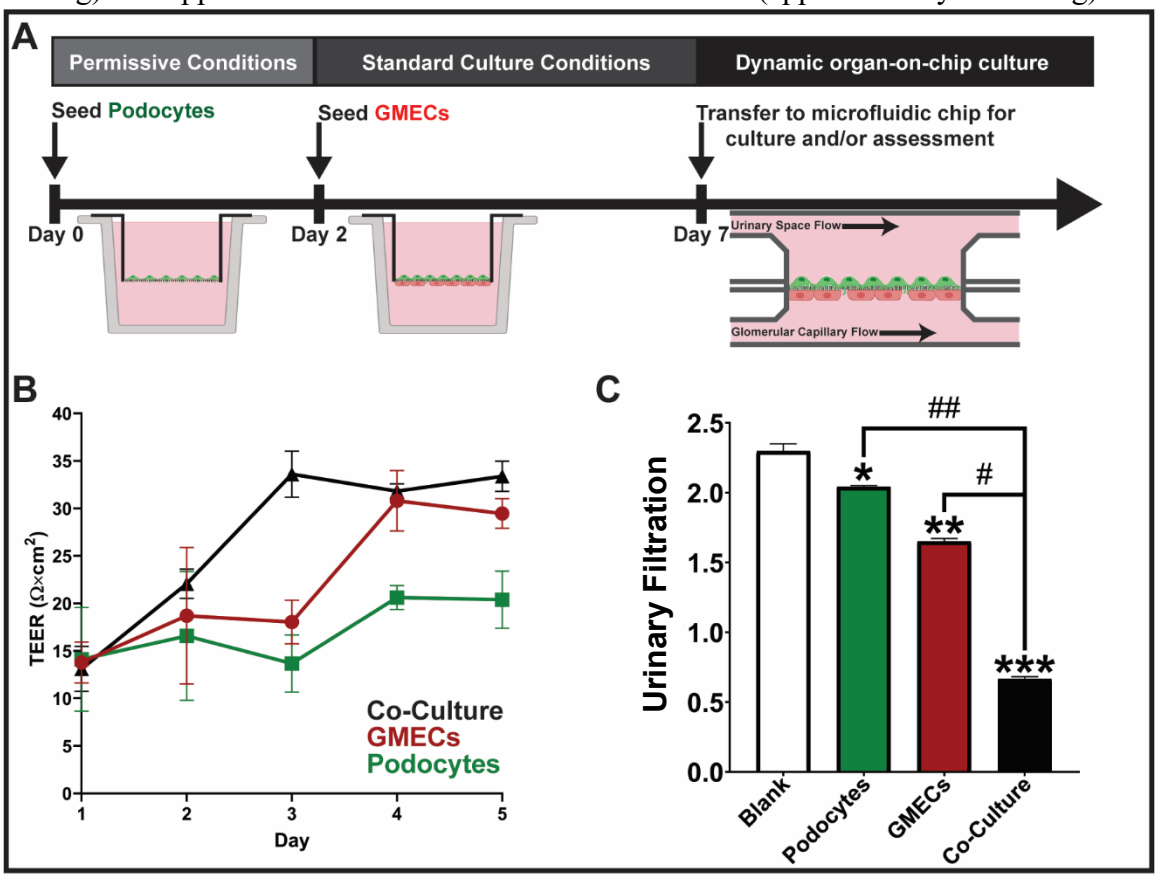

Figure 6.5 Recapitulating the GFB (A) Schematic representation of the workflow for the development of the co-culture model of the GFB. (B) TEER measurements of podocytes only (Green), endothelial cells only (Red), and co-culture (black) during static culture on a transwell insert over the course of 5 days. (C) Urinary filtration of albumin in 1 hour on the microfluidic device. The significant decrease in the urinary filtration of albumin between the co-culture, despite similar TEER values, indicates a functional barrier as opposed to a physical barrier. Statistical analysis by unpaired t test (N = 2; * indicates vs blank; # indicates vs co-culture). *P < 0.05, **P < 0.01, ***P < 0.001, #P < 0.001, ##P < 0.0001

applied to apical flow channel. The basal flow channel was supplemented with bovine serum albumin (2 mg/mL) to mimic the oncotic pressure gradient. Compared to a blank membrane (*i.e.* no cells), all three cell models significantly reduced the urinary filtration of albumin (Figure 6.5C). Interestingly, the urinary filtration of albumin was also significantly less in the co-culture model compared to GMECs only, despite the similar TEER measurements.

6.3.5 Spingolipid exposure alters albumin filtration in cultured podocytes

Sphingolipids have been shown to be important second messengers in cellular processes such has growth and apoptosis (*130, 131*). S1P, which is generated by phosphorylation of sphingosine, has been indicated to play a role in many diseases, including diabetic kidney disease (*132, 133*). Podocytes play a significant role in the filtration of albumin at the glomerular filtration barrier (GFB) (*134*). Dysfunction of podocytes can lead to albuminuria, which is a hallmark of kidney disease. To elucidate the effect of S1P podocytes' ability to maintain a functional filtration barrier, cells were exposure to 5 μM S1P for 1 hour and then assessed for filtration function. A significant increase the urinary filtration of albumin was observed after just 1 hour of exposure to 5 μM S1P (Figure 6.6). Urinary filtration of inulin, which is freely filtered at

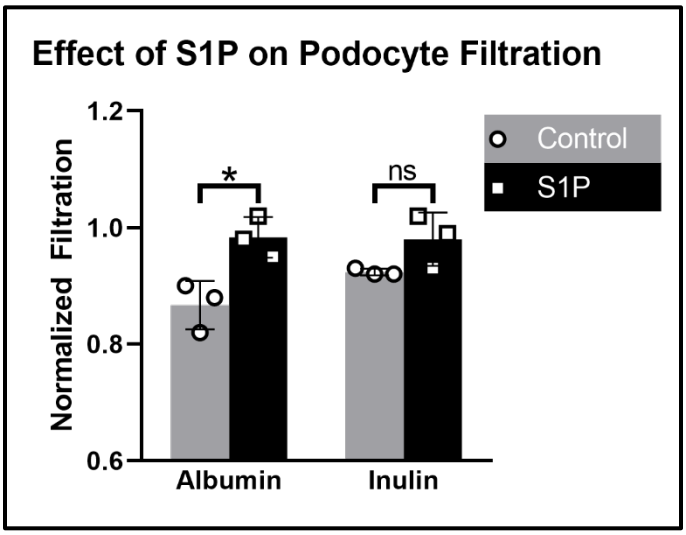

Figure 6.6 Effect of S1P on Podocyte Filtration. Urinary filtration of albumin was increased as a result of exposure to S1P. Urinary filtration of inulin, which is freely filtered at the GFB, was not significantly altered. Statistical analysis by unpaired t-test (n=3, *$p < 0.05$).

the GFB, was not significantly altered due to exposure to S1P. The observed change in albumin filtration after exposure to S1P suggests that exposure to sphingolipids may lead to podocyte dysfunction, resulting in albuminuria.

6.4 Discussion

MPS, also referred to as organs-on-chips, represent a new approach to *in vitro* modeling of biologic phenomenon. These devices aim to recapitulate the minimal functional unit of organs using microfluidics and microfabrication. For many organs, such as the lung and kidney, this functional unit is a biologic barrier. As a result, modeling of barrier function has been the primary focus of many organ-on-chip devices. One the earliest organs-on-chips, a lung-on-chip, was developed using PDMS (*27*). However, PDMS absorption of small molecules is problematic for drug discovery assays (*30*). Here, we report the design and fabrication of a PDMS-free microfluidic device that can recapitulate many of the same dynamic stimuli originally described for organs-on-chips.

The overall design of the microfluidic device is analogous to many biologic barriers and organ-on-chip devices. Two independent flow channels are separated by a porous membrane that can support the culture of an endothelial and epithelial cell layer. The fabrication of stacked channels is relatively straightforward when using additive manufacturing techniques, such as soft lithography or 3D printing. Through these methods, devices can be assembled in layers either through bonding or material deposition. However, fabrication through SRP of the design presents a challenge. Since material must be removed, it is difficult to achieve closed channels at different heights within the device. This challenge has been overcome through the resealable form-factor implemented in the

device design and the incorporation of an oxygen-permeable membrane to seal the basal channel.

Independent perfusion of the two-channels was achieved using two microfluidic pressure pumps. Pressure-driven flow control provides many advantages over other methods, including stable, pulseless flow, fast response time, and precise flowrate control. Further, the use of pressurized air facilitated the implementation of cyclic air flow to stretch the porous membrane and mimic the human breathing cycle. We demonstrated the ability to create an air-liquid interface co-culture model that can be incorporated into the microfluidic device. Thus, modeling a lung-on-chip in the present design. Pressure-driven flow also facilitated the generation of hydrostatic pressure gradients, like those that are found at the glomerular filtration barrier. Together, the versatility of the platform enables recapitulation of multiple *in vivo* microenvironments.

The final proof-of-concept experiment for the microfluidic device design was to model the filtration function of the glomerulus. This was achieved by culturing the glomerular endothelial and epithelial cells on a porous membrane which could be transferred into the MPS. We also demonstrated that the ability of podocytes to effectively filter albumin can be modulated by exposure to sphingolipids. With this, we aimed to demonstrate the utility of the microfluidic device discussed in the Chapter 5. A significant limitation of traditional static culture systems is the inability to recapitulate organ-level function. The microfluidic device to model biologic barriers enables filtration assays to functionally assess podocytes. Despite the model being limited to just podocytes in the present study, a significant increase was observed in urinary filtration of albumin after exposure to S1P. Future studies will focus on recapitulating a more complete GFB by

incorporating endothelial cells and a basement membrane. Albumin is one of the most abundant proteins in human blood and the loss of albumin via the urine is a key clinical marker for kidney failure. We demonstrate that under physiologically relevant pressures, the co-culture of GMECs and CiPodos can effectively prevent urinary filtration of albumin. In the present model, however, urinary filtration of albumin was not minimized to levels that would be acceptable in a clinical setting. This may be attributed to the cell source or the lack of a basement membrane components. The GFB is a complex, highly selective filter and future work will be necessary to improve upon the biologic components.

CHAPTER 7

Integrated Platform for Operating and Interrogating Organs-on-Chips

7.1 Overview

Organs-on-chips aim to recapitulate the minimal physiologically relevant functional unit of tissues and organs (*5*). This has been achieved through the convergence of advances in the fields of microfluidics, microfabrication, cellular engineering, and tissue engineering. The ability of organs-on-chips to recreate not only healthy organ-level physiology, but also dynamic pathophysiological phenomena has generated huge interest from the pharmaceutical industry. Specifically, these in vitro devices are viewed as a more predictive pre-clinical model for drug discovery that can potentially address the high attrition rate of promising therapeutic compounds (*135*). However, a number of challenges beyond the validation of physiological and pathophysiological models has slowed the adoption of organ-on-chip technology. For pharmaceutical end users, these challenges include throughput capability, platform stability, reproducibility, and compatibility with existing laboratory equipment and processes (*136*).

Automated high-throughput screening has become an important part of early drug discovery (*137*). However, the complexity of operating an organ-on-chip makes integration with completely autonomous systems difficult. Further, advancements in this field have focused primarily on the development and characterization of microfluidic chips to create models of a specific organ function and/or disease state (*138*). Many of these devices not only require unique methods for cell culture and functional readouts, but also implement custom fluidic controllers. Further, the diversity of existing organ-on-chip devices creates a challenge in developing platforms for validation and comparative studies. As a result, current systems, developed both in research labs and emerging start-up companies, are yet

to fit seamlessly into the drug development pipeline and address the needs of the pharmaceutical industry (*139, 140*).

To simplify the operation of organs-on-chips, we report on a platform that automates continuous perifusion culture and dynamic cell secretion collection through the integration of programmable hardware. Key design parameters of the integrated platform include compatibility with existing cell culture equipment (i.e. standard CO2 incubators), precise microfluidic control of media, and user-friendly automation. The platform was developed using in-house rapid prototyping and commercially available motors, fluidic switches, and microcontrollers. We validate platform functionality using our previously developed fluidic device for interrogating pancreatic islets (*6*). Through the use of hardware that is agnostic to microfluidic chip design and development of a user-friendly interface, this platform aims to facilitate the adoption of organ-on-chip technology in research labs and companies that lack the engineering expertise to develop and operate existing organ-on-chip devices and microfluidic controllers.

7.2 Materials and Methods

7.2.1 Hardware

A 3-channel, 8-roller peristaltic pump with independent channel control (Cole-Parmer GmbH) is used to drive media throughout the platform. A 10-position/11-port rotary shear valve (IDEX Health & Science) serves as a manifold for selection of media reservoirs and a 3-way isolation valve (NResearch Inc.) directs media for either recirculation or collection. Tubing and fluidic connections were obtained from Cole-Parmer GmbH.

Samples are collected in a standard 96-well plate that sits on a custom-built stage. X-direction and Y-direction movement of the stage is controlled by a NEMA-17 stepper motor (Adafruit) coupled to fast-travel, ultra-precision lead screw (McMaster-Carr). To test the system, our previously described fluidic chip, FP-3W, was used as a model organ-on-chip device.8 A microfluidic chip holder (Micronit) was used to seal the FP-3W fluidic chip and introduce fluidic connections. Bubble traps (Darwin Microfluidics) were placed just before the inlet of the organ-on-chip device to prevent bubbles from entering the device.

An Arduino Mega 2560 microcontroller (Arduino) connected to a motor shield (Adafruit) and CoolDrive® driver circuits (NResearch Inc.) was used to control the stepper motors and 3-way isolation valves. A 24 V, 160 W power supply (Digi-Key) was used to power the entire system via a custom printed circuit board, comprised of 12 V and 5 V DC converters (Traco Power) and a current limiter. All electronic components are rated to function in the temperature and humidity of a standard cell culture incubator.

7.2.2 Design and fabrication

The entire system was designed using SolidWorks 3D computer-aided design (CAD) software (Dassault Systèmes). To ensure precise fitting and facilitate fabrication, CAD files for each hardware component were either obtained from the manufacturer or designed de novo. Custom parts for the platform housing and mounting hardware were also developed in SolidWorks and fabricated from clear acrylic (McMaster) using a 30 W CO_2 laser machine (Epilog). Design files for the custom parts are available on the NIH 3D Print Exchange (https://3dprint.nih.gov/discover/3dpx-011914).

7.2.3 Graphical user interface

A custom graphical user interface (GUI) was developed in Python, using the Tkinter package, to integrate the control of hardware components and enable user-programmed automated protocols. A USB hub (D-Link), housed within the platform, provides a central point for USB connections to each of the hardware components. As a result, only a single RS-232 serial connection is required to enable the GUI to communicate with all the hardware components. The GUI consists of modules that allow for manual control of the platform, programming of automated procedures, and monitoring of platform status. The GUI is packaged into a single, executable file that can be installed on any computer. The complete Python code is available on GitHub (https://github.com/lievbirman/CultureFlow) mindful

7.2.4 Islet isolation and culture

Pancreatic islets were procured from human organ donors by the Human Islet Cell Processing Facility at the Diabetes Research Institute (University of Miami Miller School of Medicine, Miami, FL) under IRB approval for use of human tissue for research. Islets were cultured in Prodo Islet Media (Standard) supplemented with 5% Human AB Serum and 2% glutamine/glutathione overnight at 37 °C and 5% CO_2 after the isolation procedure. All media and supplements were purchased from PRODO Laboratories.

Following the overnight static culture, islets were loaded into the fluidic chip and connected to the platform. Islets were cultured under continuous perifusion at 30 μL/min in the FP-3W fluidic chip. Media was drawn from a single reservoir, with 15 mL of media, and recirculated for all three wells during the culture period.

7.2.5 Dynamic glucose stimulated insulin secretion assay

Islet function was evaluated after 24 hours of culture on the platform using a dynamic glucose stimulated insulin secretion (dGSIS) assay. A standard perifusion buffer solution (125 mM NaCl, 5.9 mM KCl, 2.56 mM $CaCl_2$, 1.2 mM MgCl, 0.1% w/v BSA, and 25 mM HEPES, pH 7.4) was prepared for the dGSIS assay (*101*). Stimulus solutions were prepared by supplementing the buffer solution with 3 mM glucose (Low G), 11 mM glucose (High G), or 25 mM KCL for low glucose, high glucose, and depolarization stimuli, respectively.

An automated perifusion protocol was loaded via the GUI, consisting of the following steps during perifusion at 100 μL min−1: 1 hour equilibration in low glucose, 10 minutes in low glucose, 20 minutes in high glucose, 10 minutes in low glucose, 10 minutes in KCL, then 10 minutes in low glucose. After the 1-hour equilibration, which was dispensed into a waste reservoir, samples were collected in a 96-well plate with a sampling time of 2 min per well. Following the automated perifusion protocol, each well was imaged, and the number of islets was counted manually using ImageJ. Insulin content was quantified using an Insulin ELISA kit (Mercodia). Insulin secretion per islet was determined based on flow rate and number of islets per well.

7.2.6 Cell viability assay

Viability of islet cells was assessed using the LIVE/DEAD™ Viability/Cytotoxicity Kit (Thermo Fisher Scientific). The live/dead staining procedure was performed as an automated protocol. First, islets were washed by perfusing phosphate buffered saline (PBS) through the fluidic chip for 5 minutes. Then, the staining solution, comprised of 2 μM calcein-AM and 4 μM ethidium homodimer-1 (EtD-1) diluted in PBS,

was perfused through the chip for 5 minutes. A 30-minute wait step was included to incubate the islets in the staining solution. The fluidic chip was then removed from the system and islets were imaged on a Zeiss LSM 800 confocal laser scanning microscope (Carl Zeiss AG). Quantification of islet viability was performed using ImageJ (NIH). Briefly, images from three separate field of views were thresholded and the area of live (stained with calcein-AM) and dead cells (stained with Etd-1) was determined using the 'Analyze Particles' function in ImageJ. Percent viability was calculated as the area of live cells divided by the total area of live and dead cells.

7.3 Results

7.3.1 Hardware overview

We have developed a platform to integrate the culture and analysis of cells on an organ-on-chip device. The platform consists of three hardware systems interconnected in a single house: (i) microfluidic handling system, (ii) organ-on-chip, and (iii) sample collection stage (Figure 7.1A). To facilitate cell culture, the footprint of the system housing is designed to fit in a standard cell culture incubator. The internal dimensions of a CO2 incubator, which can vary by model, are approximately 470 mm × 531 mm × 607 mm (W × D × H). To ensure that the platform met the requirements to fit into an incubator, the platform design was modelled using 3D CAD software (Figure 7.1B). The footprint of the fully assembled platform is just 356 mm × 432 mm (W × D), which leaves enough space for the platform to be placed in an incubator without interference from shelving mounts (Figure 7.1C).

The microfluidic handling system consists of valves and a pump to deliver media to the organ-on-chip device and direct media for either recirculation or collection. A 10-

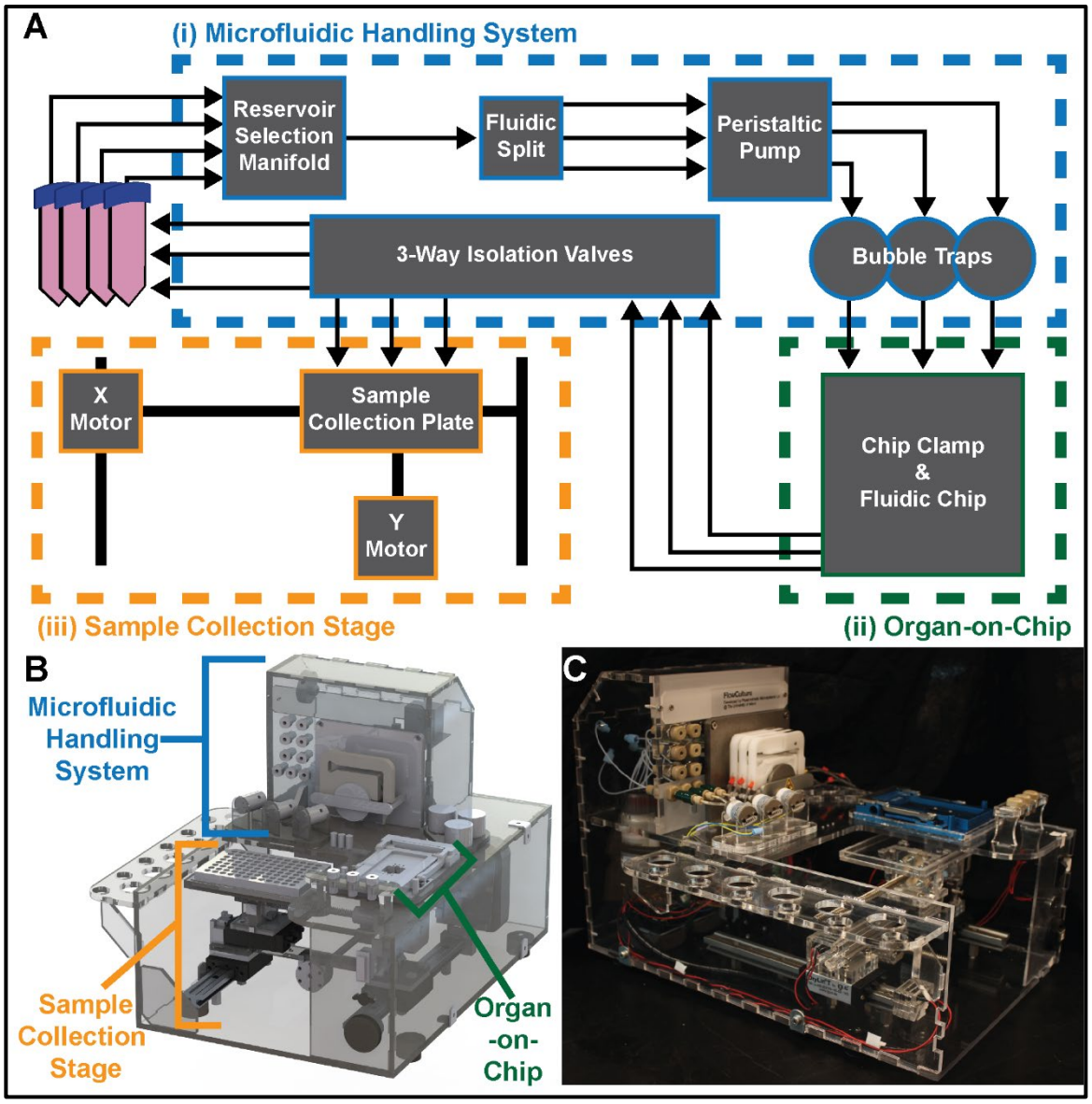

Figure 7.1 Design and development of integrated platform. (A) Schematic representation of integrated platform comprised of three major systems: (i) microfluidic handling system; blue, (ii) organ-on-chip system; green, and (iii) sample collection stage; orange. (B) Three-dimensional CAD render of platform design. Bubble traps not pictured (C) fully assembled platform with all components included. Motors are blocked by other components.

position rotary shear valve serves as a manifold, which allows for up to 10 media reservoirs to be installed. The output of the manifold is split into the three channels of the peristaltic pump. Each channel of the peristaltic pump can be controlled independently which enables control and experimental groups to be run in parallel or for groups to be run in triplicate. With the current 0.051" inner diameter tubing configuration, the pump can achieve flow

rates ranging from 1.7 μL/min up to 1.7 mL/min. The wide range of flow rates and standardized connectors ensure that the microfluidic handling unit can be compatible with a variety of organ-on-chip devices. Except for the peristaltic pump tubing, fluorinated ethylene propylene (FEP) tubing is used throughout the microfluidic handling system. FEP tubing is chemically inert and gas permeable making it an ideal tubing material for use in a standard cell culture incubator.

A sample collection stage was designed to achieve sample collection into all the wells in a standard 96-well plate. The sample collection stage is comprised of two NEMA-17 stepper motors coupled to lead screws and mounted on rails. The 96-well plate sits on a custom-built stage mounted to the X-axis rail. The sample collection stage has a 235 mm × 160 mm range of motion. The extra space allows for an eject position, where the plate can be either loaded on to or collected from the platform.

Currently on market, there are only a few options for automated culture of organ-on-chip devices and, more specifically, for assessment of pancreatic islets. Existing platforms, such as the BioRep perifusion system, can cost upwards of $80,000. At this price point, the BioRep system is specifically for high throughput perifusion (*101*). Additionally, this system is not designed for cell culture. While the system does provide precise temperature control, there is no option for gas or humidity control. The ability to only provide temperature control limits the BioRep system capability for long-term culture.

In its current configuration the entire integrated platform we have developed costs approximately $7000 (Appendix A6). However, nearly half of this cost is due to the peristaltic pump and the microfluidic chip holder. Low-cost peristaltic pumps have been previously developed, but require much larger tubing which would increase the overall in

system volume and lead to increased delay times for sample collection (*141*). The cost of the microfluidic chip holder can be avoided through the use of other organ-on-chip devices, which can be connected to the integrated platform through the standardize fluidic connections. The overall cost of these components is justified by the ease of programming, which also reduced the complexity of the GUI, and the overall end user experience from setup to operation.

7.3.2 Software overview

To simplify user control of the platform hardware, software has been developed to allow for automated protocols to be programmed and run from a single Graphical User Interface (GUI). The lean back-end code, written in Python, uses a modular system architecture which is amenable to expanding the hardware components and software features. Each hardware component is controlled via modules that translate Python code into serial command outputs.

To minimize the connections running out of the incubator, communication for hardware components was centralized through a USB hub. The USB hub provides a single RS-232 serial connection to the computer running the software (Figure 2A). The compact, user-friendly GUI software facilitates operation of the system through either a manual or automatic mode (Figure 2B). Manual mode allows the user to control selection of reservoirs, set sampling rate, move the collection stage, and independently set the flow rate for each pump channel. Thus, manual mode enables the full operating range of the system to either perform short experiments or optimize conditions. The automatic mode offers the same flexibility of choice as the manual mode but allows the user to define experimental

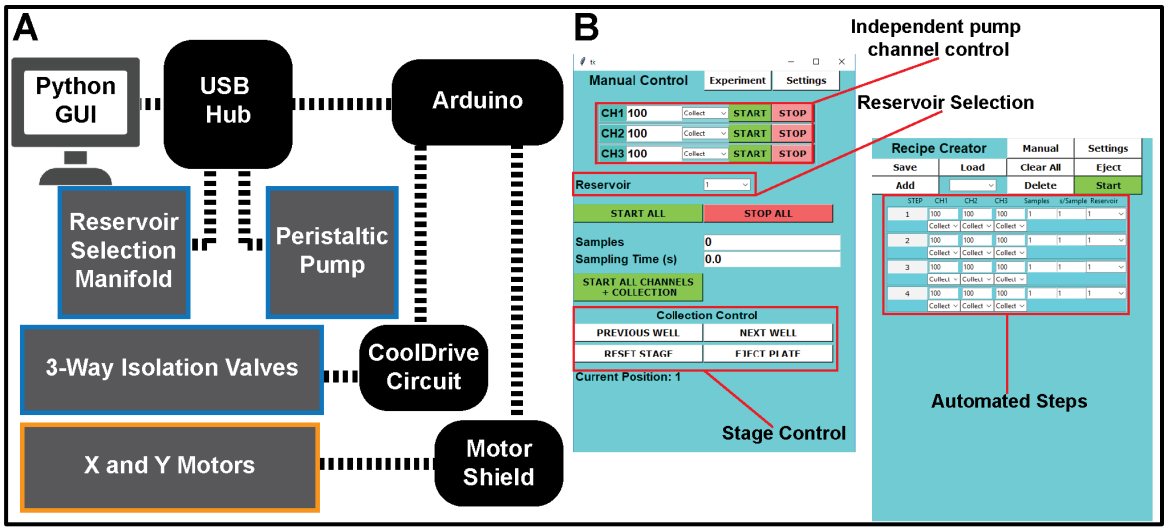

Figure 7.2 Integration of hardware control via Python GUI. (A) Communication network to enable GUI control of hardware via a single USB hub. An Arduino microcontroller is used to provide control to the 3-way valves and motors. (B) Screenshots of the main page and recipe creator page of the GUI. From the main page, the user can manually control most aspects of the platform. From the recipe creator page, the user can set a series of steps to run automatically.

protocols via a step-by-step input form. This allows for longer experiments that require multiple media changes and/or switching between culture and sample collection.

7.3.3 Design verification

Verification testing was performed to ensure to that the platform met design specifications for flow rate accuracy, valve function, and leak-free operation. To verify that the power supply and GUI control for the commercial pump were functioning as intended, flow rate accuracy tests were performed. The system was first calibrated by dispensing 100 µL of water in 1 minute using a function built into the peristaltic pump. Volume was determined by measuring the mass of water collected. Using the GUI, the pump was then programmed to run for 1 minute at flow rates ranging from 10 µL/min to 100 µL/min.

Table 7.1 Flow rate verification testing results. The volume dispensed at each flow rate was collected for 1 minute. Volume collected displayed as average ± standard deviation (n = 3)

Flow Rate (µL/min)	Volume Collected (µL)	Percent Error
10	10.5 ± 0.08	5.0%
25	26.0 ± 1.15	3.9%
50	51.0 ± 1.18	2.0%
75	75.8 ± 1.19	1.1%
100	102.1 ± 1.06	2.1%

For all flow rates tested, the average volume collected at the collection stage from each channel never varied by more than 5% from the expected volume. Further, the standard deviation for each tested flow rate was less than 1.2 µL (Table 7.1). Across all flow rates, the average volume difference from the expected value was just 1.1 µL. Together, these results demonstrate that the integrated platform maintains a level of high accuracy and precision.

Key features of the platform include efficient switching between media reservoirs and accurate sample collection. The low dead volume of the selection valve ensures there is essentially no mixing of media during reservoir changes. The dispensing nozzles were positioned such that the tip of the nozzle grazes the top of the collection plate to collect the final drop of media and mitigate the chance of media being dispensed outside of the designated well. To verify these design specifications, a test protocol requiring two reservoirs and switching between sample collection and waste dispensing was developed. A "snake" pattern was implemented for collection in the 96-well plate to minimize travel distance between well columns (Figure 7.3A). The automated protocol set a flow rate of 1 mL min−1 and a sampling rate of 15 seconds per well. First, 10 samples were collected

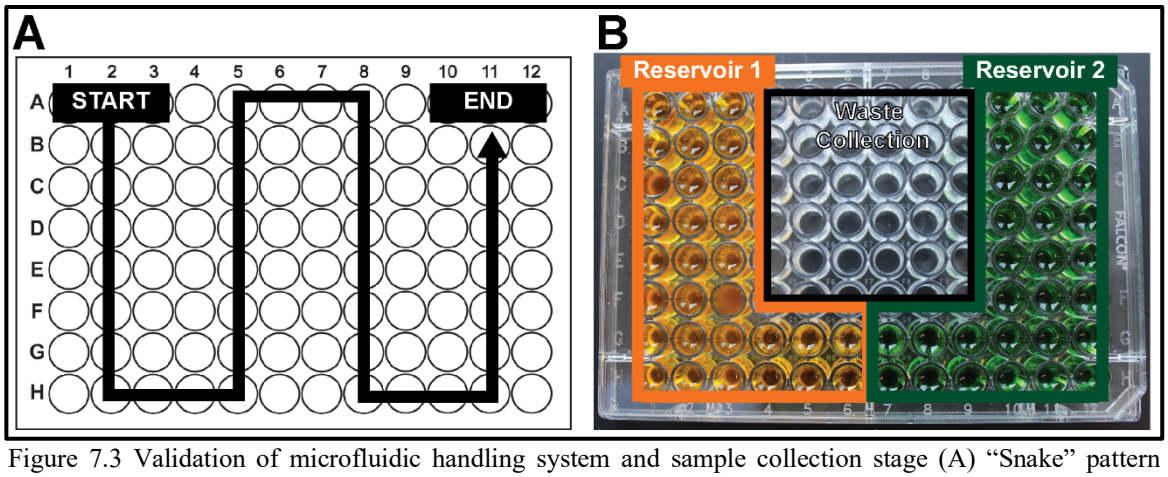

Figure 7.3 Validation of microfluidic handling system and sample collection stage (A) "Snake" pattern programmed for sample collection to minimize travel distance when a column of wells was filled. (B) Validation of platform functionality via a programmed protocol set to collect from reservoir 1, dispense to waste, then collect from reservoir 2.

from reservoir one, the system then switched to reservoir two and dispensed to a waste reservoir for 3 minutes. In the last step, the system switched back to sample collection and 10 samples were collected from reservoir two (Figure 7.3B). Upon completion of the programmed steps, the system automatically ejected the collection plate for the user to retrieve (Appendix A7). Leaks were rarely observed. The primary cause of the minor leaks that did occur was improperly connected tubing and was easily resolved by tightening the connections.

7.3.4 Automated dynamic culture and viability assay

To validate that the integrated platform is compatible with organ-on-chip systems, human pancreatic islets were loaded into the FP-3W fluidic chip and cultured on the platform for 24 hours and assessed for cell viability. An automated culture protocol, to recirculate islet culture media at 30 μL/min for 24 hours, was programmed and performed using the GUI developed for the system. The geometric features in the flow path of the FP-3W fluidic chip are designed to minimize shear stress on islets while providing a sufficient supply of nutrients. After the 24-hour culture protocol, islets could be visualized in the culture wells with minimal deviation from their original position (Figure 7.4A). Additionally, no bubbles were observed in the fluidic chip during or after the culture the period.

To demonstrate the versatility of the platform and that cells remained viable, an automated live/dead staining protocol was performed. The automated protocol successfully labelled islet cells with either calcein-AM or EtD-1, which qualitatively demonstrated that islets were still highly viable after the 24-hour culture period (Figure 7.4B). Quantitative image analysis was also performed. Islet viability, as a percentage of total islet area, was

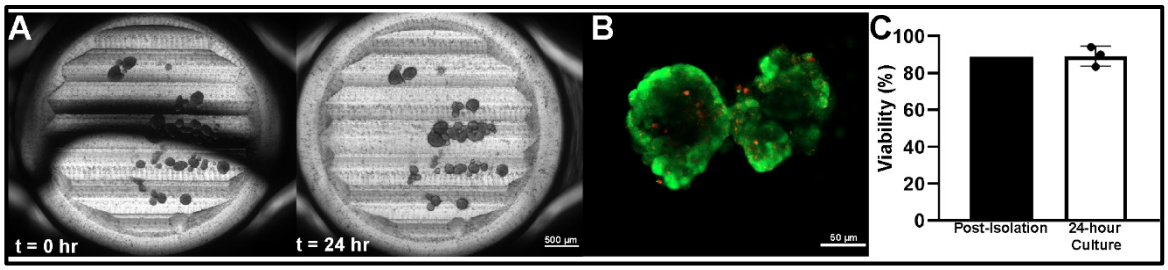

Figure 7.4 Islet viability in FP-3W after 24-hour culture on integrated platform. (A) Brightfield images after loading islets into FP-3W (t = 0 h) and after 24 hours of continuous perifusion on the integrated platform. At t = 0 h, the media used to transfer islets in the chip does not completely fill the well, which causes refraction of the light. After 24 hours, the well is filled with media and islets are in approximately the same location. (B) Representative live/dead stain of islets using ethidium homodimer-1 (red, dead) and calcein-AM (green, live). (C) Quantification of islet viability from three field of views after 24-hour culture and automated staining procedure. Islets viability remained unchanged compared to the viability obtained by Human Islet Cell Processing Facility.

calculated as the live cell area divided by the sum of both live and dead cell area of each islet. Compared to the post-isolation viability (88.9%) reported by The Human Islet Cell Processing Facility, which performed the islet isolation, islet viability was unchanged (89.1 ± 5.4%) after 24 hours of dynamic culture on the integrated platform (Figure 7.4C).

7.3.5 Automated functional assessment of human pancreatic islets

The ability to perform on chip functional assessments is an important feature for organs-on-chips. The integrated platform aims to facilitate the switch from culture to assessment. To demonstrate this capability, a dGSIS assay was performed on human pancreatic islets that were in culture on the platform. Approximately 40 islets were loaded into each well of the fluidic chip and cultured for 24 hours on the integrated platform. After the culture protocol was completed, solutions of low glucose (3 mM), high glucose (11 mM), and KCL (25 mM) were loaded on to the platform. Next an automated dGSIS protocol was loaded and run from the Python GUI. Islets were exposed to low glucose for 1 h to acclimate to the perifusion buffer solution. Then, samples were collected every 2 min while islets were exposed to low glucose, high glucose, and KCL solutions in series.

Upon completion of the automate dGSIS assay, each well was imaged, and the number of islets was manually counted using ImageJ (Figure 7.5A).

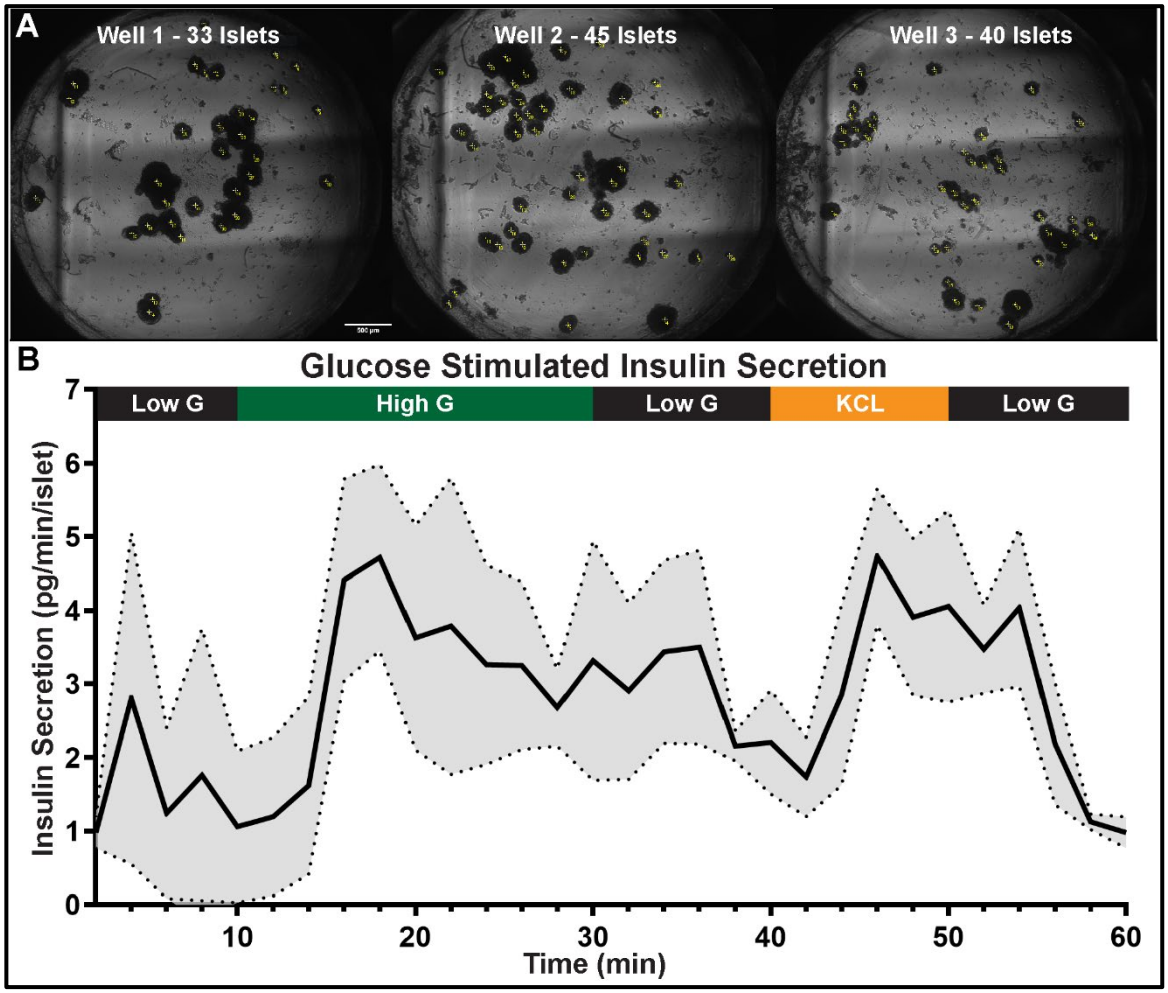

Figure 7.5 Quantification of islets and insulin secretion profile obtained from automated dGSIS. (A) Screenshot of counted islets in each well of the FP-3W fluidic chip after 24 hours of dynamic culture. (B) In response to high glucose stimulus (11 mM; High G), insulin secretion follows a biphasic response with a first phase spike followed by a delayed second phase, which runs into the second low glucose exposure (3 mM; Low G). This is followed by a drop toward the baseline insulin secretion before a first phase secretion peak is achieved by exposure to 25 mM KCL. The observed delay between stimulus exposure and peak insulin secretion is due to system volume. The shaded region of the dGSIS profile represents the standard deviation from the mean insulin secretion (n = 3).

It is well-established that insulin secretion from islets in vivo is characterized by a "first phase" spike, followed by a delayed "second phase" of sustained secretion (*7*). Further, this response is observed specifically when glucose is metabolized within an islet (*99*). Stimulation by KCL, which causes membrane depolarization, only results a first phase spike of insulin secretion before returning to basal levels. Insulin secretion,

normalized to the flow rate and number of islets per well, was collected during the automated dGSIS protocol (Figure 7.5B). There is about a 6-minute delay from the time high glucose or KCL stimulation is applied to the time a significant increase in insulin secretion is observed. This is partly a result of delays in media delivery and sample collection due to system volume. Overall, the functional assessment of pancreatic islets demonstrated that the integrated platform can not only provide stimuli to cultured cells, but also can resolve the biphasic insulin secretion profile through sample collection.

7.4 Discussion

The platform designed, built, and tested here demonstrates the ability to integrate continuous perifusion culture and cellular assessment assays for use with organ-on-chip devices. We were able to culture pancreatic islets and perform both a dGSIS and a live/dead assay using automated protocols through a GUI designed to operate the platform. Further, the results presented demonstrate that the use of our previously developed FP-3W fluidic chip can be expanded to include continuous perifusion culture, in addition to the previously described interrogation methods. The fluidic and mechanical components implemented are sufficiently precise to capture dynamic cell secretion phenomenon, such as the biphasic insulin secretion profile of pancreatic islets. Compared to commercially available automated perifusion systems, this integrated platform provides a wider range of capabilities at lower price point. Overall, this platform and approach for automated operation of organs-on-chips are an important advancement for transitioning organ-on-chip technology to a broader end user population. Future work will aim to develop protocols for culture and assessment of other 3D cell constructs. While the current system relies heavily on plastic parts and prototyping-grade electronics, the design requires little modification to

be manufactured with robust, high-quality components. Ultimately, we hope to develop a polished system that can be competitive in the organ-on-chip market as a platform for a wide range of experiments involving culture and assessment using any of the currently available organ-on-chip devices.

CHAPTER 8

Conclusions and Future Outlook

8.1 Conclusions

The foundation of our understanding of human physiology and disease pathogenesis is the tools available to pursue novel research. The convergence of microfluidics and tissue engineering resulted in the development of organs-on-chips. These microphysiological systems provide a novel approach toward *in vitro* understanding of biologic processes. In CHAPTER 2, the current roadblocks for the translation of organ-on-chip technology was discussed. While the ability to improve the success and efficiency of drug discovery is a promising application organ-on-chip technology, the full potential of these microphysiological systems can be unlocked through development and translation of devices for researchers.

In CHAPTER 3, a throughout characterization of the fluid dynamics within our fluidic platform was performed from an engineering point-of-view. Then, through collaboration with the Humphreys Lab, we demonstrate that this knowledge can be applied to improve the vascularization and maturation of kidney organoids. This multi-disciplinary effort highlights the approach implemented throughout this dissertation to extract the maximum utility from microfluidic organs-on-chips.

The findings in CHAPTER 4 demonstrate the utility of the integrated pseudoislet-microfluidic system to manipulate and study human islets. This was achieved by translating the system to the Powers and Brissova Group at Vanderbilt University to perform synchronous assessment of hormone secretion and live imaging. Ultimately, the integration of the pseudoislet approach with a microfluidic perifusion system and live cell imaging provides a powerful experimental platform to gain insight into human islet biology and the

mechanisms controlling regulated islet hormone secretion which currently limits the development of novel therapeutic approaches. Here, we focused on virally mediated gene expression to alter signaling pathways, but this system could be adapted to accommodate technologies such as CRISPR. Combined with accurate cell-specific targeting, this approach would allow the measurement of intracellular dynamics at the individual cell level and distinguish intracellular responses of α and β cells to stimuli.

CHAPTER 5 highlights the capacity of our islet MPS to elucidate complex islet physiological and pathophysiologic processes by combining dynamic 3D culture, optical assessment, and functional assays. Moreover, this MPS platform can be used to study temporal interactions between complex matrices and other 3D organoids, while also limiting the amount of sample required for assessment. This was demonstrated through a collaborative effort with the Stabler Lab at the University of Florida, where the MPS was translated to Gainesville and multiparametric assessment experiments were performed by Smit Patel. Ultimately, the culture and multiparametric assessment of organoids in this MPS may provide valuable data for the development of novel therapeutics and the study of type 1 diabetes.

CHAPTER 6 focused on the development of a microfluidic platform to recapitulate biologic barrier functions. Barriers are found throughout the human, from the brain to the gut. Here, we developed a platform to recapitulate the air-liquid interface of the lung alveolus and the glomerular filtration barrier found in the kidney nephron. A novel design that enabled independent apical and basal flow channels to be incorporated into our PMMA-based device using SRP. Microfluidic pressure-pumps were utilized to drive flow through the channels. Additionally, the use of pressure-pumps enabled cyclic application

of air to generate mechanical stretching of the porous support membrane. Physiomimetic hydrostatic pressure gradients were generated using this platform to mimic the microenvironment of the glomerulus. Co-culture models were also developed and assessed within the platform. Specifically, the ability of a glomerular endothelial cells and podocytes to effectively prevent filtration of albumin was demonstrated.

Finally, in CHAPTER 7 we demonstrate the ability to engineer an integrated platform that can automate dynamic cell culture and assessment within organ-on-chip devices. The design was developed using a bio-mechatronic design methodology, which factors in the specific processes that occur when operating an organ-on-chip. These range from obtaining suitable cells to analysis of collected samples. The system was developed using in-house fabrication methods and commercially available microfluidic pumps and valves. A GUI was developed to allow users to easily operate the system and program automated procedures. Further, we demonstrate that platform can successfully automate the culture and assessment of primary islet organoids.

The devices and data presented in this dissertation provide an effective approach for developing microfluidic devices to recapitulate human physiology. As an emerging technology, organs-on-chips aim to provide a new tool for asking challenging biological questions. However, in their current nascent state the adoption of this technology is hindered due to the lack of expertise required to implement organs-on-chips into existing research workflows. Further, PDMS-based organs-on-chips have specific material properties that make them unsuitable for certain applications, such as testing of small hydrophobic compounds. The devices developed as part of this dissertation aim to address

limitations, but more studies are needed to fully validate and improve the organ models described.

8.2 Future Outlook

The work presented in this dissertation was primarily focused on the design and fabrication of microfluidic devices. Initial validation and proof-of-concept studies were also performed to demonstrate the utility of the platforms developed. However, there are several studies that can be performed to validate and improve these initial models. Further, the platforms described can be applied to other cellular models to study different biologic processes. In this section, I will briefly describe some of the potential future development that can be performed based on this work.

The next step in the application of the devices presented in this dissertation would be the develop of specific disease models. With respect to the islet work, the incorporation of immune cells would enable modeling of type 1 diabetes. Additionally, the GFB is the nexus of dysfunction in diabetic kidney disease. The use of patient-derived serum to develop a patient-relevant *in vitro* disease model would be an interesting study. These models could be implemented in the drug discovery pipeline to provide more relevant readouts for novel therapeutic compounds.

This work has also led me to form an organ-on-chip company, Bio-Vitro. In the last five years, there has been an abundance of new biotechnology companies entering the organ-on-chip arena. In the US, startup companies have been spun out of academic institutions primarily focused on providing research services that utilize unique organ-on-chip models. In Europe, the expansion of organ-on-chip technology is being driven by microfluidic companies looking to add organ-on-chip applications to their portfolio. The

global market for organs-on-chips is expected to reach approximately $45 million USD by 2022. This growth is driven by the potential to enhance drug discovery and development by providing an alternative tool for pharmaceutical companies, who spent over $5 billion for pre-clinical services in 2013. However, the pharmaceutical pipeline often begins in academia. Currently, the NIH has awarded total of 481 R01 grants for organoid, spheroid, and islet research. Each R01 has a $250,000 annual budget, resulting in about $120 million research expenditure focused on 3D cellular constructs. Bio-Vitro's 5-year plan would be to establish a product portfolio and develop a customer base. Year 1 will focus on transitioning manufacturing from rapid prototyping to large scale injection molding. Year 2 will focus on validating our customer segment and price point through our existing collaborations. Years 3-4 will focus on expanding our customer base and increasing sales to research laboratories. In Year 5, we will reassess the market and begin developing services for pharmaceutical companies.

WORKS CITED

1. R. Hooke, *Micrographia: or some physiological descriptions of minute bodies made by magnifying glasses with observations and inquiries thereupon*. (1665).

2. T. S. Kuhn, *The structure of scientific revolutions*. (University of Chicago Press, 2012).

3. K. I. Kaitin, Deconstructing the drug development process: the new face of innovation. *Clinical Pharmacology & Therapeutics* **87**, 356-361 (2010).

4. J. W. Scannell, A. Blanckley, H. Boldon, B. Warrington, Diagnosing the decline in pharmaceutical R&D efficiency. *Nature Reviews Drug Discovery* **11**, 191-200 (2012).

5. S. N. Bhatia, D. E. Ingber, Microfluidic organs-on-chips. *Nature Biotechnology* **32**, 760-772 (2014).

6. G. Lenguito *et al.*, Resealable, optically accessible, PDMS-free fluidic platform for ex vivo interrogation of pancreatic islets. *Lab on a Chip* **17**, 772-781 (2017).

7. P. Buchwald, A local glucose-and oxygen concentration-based insulin secretion model for pancreatic islets. *Theoretical Biology and Medical Modelling* **8**, 20 (2011).

8. P. Buchwald, FEM-based oxygen consumption and cell viability models for avascular pancreatic islets. *Theoretical Biology and Medical Modelling* **6**, 5 (2009).

9. P. Buchwald, S. R. Cechin, Glucose-stimulated insulin secretion in isolated pancreatic islets: multiphysics FEM model calculations compared to results of perifusion experiments with human islets. *Journal of Biomedical Science and Engineering* **6**, 26 (2013).

10. P. Buchwald, S. R. Cechin, J. D. Weaver, C. L. Stabler, Experimental evaluation and computational modeling of the effects of encapsulation on the time-profile of glucose-stimulated insulin release of pancreatic islets. *BioMedical Engineering OnLine* **14**, 28 (2015).

11. P. Buchwald, A. Tamayo-Garcia, V. Manzoli, A. A. Tomei, C. L. Stabler, Glucose-stimulated insulin release: Parallel perifusion studies of free and hydrogel encapsulated human pancreatic islets. *Biotechnology and Bioengineering* **115**, 232-245 (2018).

12. H. Noguchi *et al.*, Islet culture/preservation before islet transplantation. *Cell Medicine* **8**, 25-29 (2015).

13. D. E. Ingber, Reverse engineering human pathophysiology with organs-on-chips. *Cell* **164**, 1105-1109 (2016).

14. O. Gheith, N. Farouk, N. Nampoory, M. A. Halim, T. Al-Otaibi, Diabetic kidney disease: world wide difference of prevalence and risk factors. *Journal of Nephropharmacology* **5**, 49-56 (2016).

15. J. A. Jefferson, S. J. Shankland, R. H. Pichler, Proteinuria in diabetic kidney disease: a mechanistic viewpoint. *Kidney International* **74**, 22-36 (2008).

16. S. Myers, A. Baker, Drug discovery--an operating model for a new era. *Nature Biotechnology* **19**, 727+ (2001).

17. J. A. DiMasi, H. G. Grabowski, R. W. Hansen, Innovation in the pharmaceutical industry: new estimates of R&D costs. *Journal of Health Economics* **47**, 20-33 (2016).

18. C. H. Wong, K. W. Siah, A. W. Lo, Estimation of clinical trial success rates and related parameters. *Biostatistics* **20**, 273-286 (2019).

19. A dearth of new drugs. *Nature* **283**, 609-609 (1980).

20. F. Steward, G. Wibberley, Drug innovation—what's slowing it down? *Nature* **284**, 118-120 (1980).

21. M. Weatherall, An end to the search for new drugs? *Nature* **296**, 387-390 (1982).

22. J. A. DiMasi, L. Feldman, A. Seckler, A. Wilson, Trends in risks associated with new drug development: success rates for investigational drugs. *Clinical Pharmacology & Therapeutics* **87**, 272-277 (2010).

23. P. Greaves, A. Williams, M. Eve, First dose of potential new medicines to humans: how animals help. *Nature Reviews Drug Discovery* **3**, 226 (2004).

24. F. S. Collins, Reengineering translational science: the time is right. *Science Translational Medicine* **3**, 90cm17 (2011).

25. D. C. Duffy, J. C. McDonald, O. J. Schueller, G. M. Whitesides, Rapid prototyping of microfluidic systems in poly(dimethylsiloxane). *Analytical Chemistry* **70**, 4974-4984 (1998).

26. J. C. McDonald, G. M. Whitesides, Poly(dimethylsiloxane) as a material for fabricating microfluidic devices. *Accounts of Chemical Research* **35**, 491-499 (2002).

27. D. Huh, B. D. Matthews, A. Mammoto, M. Montoya-Zavala, H. Y. Hsin, D.E. Ingber, Reconstituting organ-level lung functions on a chip. *Science* **328**, 1662-1668 (2010).

28. S. K. Sia, G. M. Whitesides, Microfluidic devices fabricated in poly(dimethylsiloxane) for biological studies. *Electrophoresis* **24**, 3563-3576 (2003).

29. A. L. Paguirigan, D. J. Beebe, Protocol for the fabrication of enzymatically crosslinked gelatin microchannels for microfluidic cell culture. *Nature Protocols* **2**, 1782-1788 (2007).

30. B. J. van Meer, H. de Vries, K. S. A. Firth, J. van Weerd, L. G. J. Tertoolen, H. B. J. Karperien, P. Jonkheijm, C. Denning, A. P. IJzerman, C. L. Mummery, Small molecule absorption by PDMS in the context of drug response bioassays. *Biochemical and Biophysical Research Communications* **482**, 323-328 (2017).

31. T. H. Shin, M. Kim, C. O. Sung, S. J. Jang, G. S. Jeong, A one-stop microfluidic-based lung cancer organoid culture platform for testing drug sensitivity. *Lab on a Chip*, (2019).

32. H. Becker, L. E. Locascio, Polymer microfluidic devices. *Talanta* **56**, 267-287 (2002).

33. K. Ren, J. Zhou, H. Wu, Materials for microfluidic chip fabrication. *Accounts of Chemical Research* **46**, 2396-2406 (2013).

34. D. J. Guckenberger, T. E. de Groot, A. M. Wan, D. J. Beebe, E. W. Young, Micromilling: a method for ultra-rapid prototyping of plastic microfluidic devices. *Lab on a Chip* **15**, 2364-2378 (2015).

35. J. M. Collins, O. Reizes, M. K. Dempsey, Healthcare commercialization programs: improving the efficiency of translating healthcare innovations from academia into practice. *IEEE Journal of Translational Engineering in Health and Medicine* **4**, 1-7 (2016).

36. J. van Amerongen, Mechatronic design. *Mechatronics* **13**, 1045-1066 (2003).

37. J. Christoffersson, D. van Noort, C. F. Mandenius, Developing organ-on-a-chip concepts using bio-mechatronic design methodology. *Biofabrication* **9**, 025023 (2017).

38. W. Thielicke, E. Stamhuis, PIVlab–towards user-friendly, affordable and accurate digital particle image velocimetry in MATLAB. *Journal of Open Research Software* **2**, (2014).

39. M. H. Little, M. Takasato, Generating a self-organizing kidney from pluripotent cells. *Current Opinion in Organ Transplantation* **20**, 178-186 (2015).

40. S. T. Wereley, C. D. Meinhart, Recent advances in micro-particle image velocimetry. *Annual Review of Fluid Mechanics* **42**, 557-576 (2010).

41. J. S. Park, C. K. Choi, K. D. Kihm, Optically sliced micro-PIV using confocal laser scanning microscopy (CLSM). *Experiments in Fluids* **37**, 105-119 (2004).

42. K. A. Homan, N. Gupta, K. T. Kroll, D. B. Kolesky, M. Skylar-Scott, T. Miyoshi, D. Mau, M. T. Valerius, T. Ferrante, J. V. Bonventre, J. A. Lewis, R. Morizane, Flow-enhanced vascularization and maturation of kidney organoids in vitro. *Nature Methods* **16**, 255-262 (2019).

43. S. Fox, *Human Physiology*. (McGraw-Hill Science/Engineering/Math, ed. 12, 2010), pp. 574-611.

44. M. Takasato, X. E. Pei, H. S. Chiu, M. H. Little, Generation of kidney organoids from human pluripotent stem cells. *Nature Protocols* **11**, 1681 (2016).

45. H. Wu, K. Uchimura, E. Donnelly, Y. Kirita, S. A. Morris, B. D. Humphreys, Comparative analysis of kidney organoid and adult human kidney single cell and single nucleus transcriptomes. *BioRxiv*, 232561 (2017).

46. C. W. van den Berg, L. Ritsma, M. C. Avramut, L. E. Miersma, B. M. van den Berg, D. G. Leuning, E. Lievers, M. Koning, J. M. Vanslambrouck, A. J. Koster, S. E. Howden, M. Takasato, M. H. Little, T. J. Tabelink, Renal subcapsular transplantation of PSC-derived kidney organoids induces neo-vasculogenesis and significant glomerular and tubular Maturation in vivo. *Stem Cell Reports* **10**, 751-765 (2018).

47. M. Saemisch, M. Balcells, L. Riesinger, M. Nickmann, S. I. Bhaloo, E. R. Edelman, H. Methe, Subendothelial matrix components influence endothelial cell apoptosis in vitro. *American Journal of Physiology-Cell Physiology* **316**, C210-C222 (2019).

48. E. Ferrero, M. E. Ferrero, R. Pardi, M. R. Zocchi, The platelet endothelial cell adhesion molecule-1 (PECAM1) contributes to endothelial barrier function. *FEBS Letters* **374**, 323-326 (1995).

49. J. S. Nielsen, K. M. McNagny, The role of podocalyxin in health and disease. *Journal of the American Society of Nephrology* **20**, 1669-1676 (2009).

50. A. Q. Lam, B. S. Freedman, R. Morizane, P. H. Lerou, M. T. Valerius, J. V. Bonventre, Rapid and efficient differentiation of human pluripotent stem cells into intermediate mesoderm that forms tubules expressing kidney proximal

tubular markers. *Journal of the American Society of Nephrology* **25**, 1211-1225 (2014).

51. M. Brissova, R. Haliyur, D. Saunders, S. Shrestha, C. Dai, D. M. Blodgett, R. Bottino, M. Campbell-Thompson, R. Aramandla, G. Poffenberger, J. Lindner, F. C. Pan, M. G. von Herrath, D. L. Greiner, L. D. Shultz, M. Sanyoura, L. H. Phillipson, M. Atkinson, D. M. Harlan, S. E. Levy, N. Prasad, R. Stein, A. C. Powers, α cell function and gene expression are compromised in type 1 diabetes. *Cell Reports* **22**, 2667-2676 (2018).

52. C. Chen, C. M. Cohrs, J. Stertmann, R. Bozsak, S. Speier, Human beta cell mass and function in diabetes: Recent advances in knowledge and technologies to understand disease pathogenesis. *Molecular Metabolism* **6**, 943-957 (2017).

53. M. Cnop, N. Welsh, J. C. Jonas, A. Jörns, S. Lenzen, D. L. Eizirik, Mechanisms of pancreatic β-cell death in type 1 and type 2 diabetes: many differences, few similarities. *Diabetes* **54**, S97-S107 (2005).

54. A. L. Gloyn, E. R. Pearson, J. F. Antcliff, P. Proks, G. J. Bruining, A. S. Slingerland, N. Howard, S. Srinivasan, J. M. Silva, J. Molnes, E. L. Edghill, T. M. Frayling, I. K. Temple, D. Mackay, J. P. Shield, Z. Sumnik, A. van Rhijin, J. K. Wales, P. Clark, S. Gorman, J. Aisenberg, S. Ellard, P. R. Njølstad, F. M. Ashcroft, A. T. Hattersley, Activating mutations in the gene encoding the ATP-sensitive potassium-channel subunit Kir6.2 and permanent neonatal diabetes. *New England Journal of Medicine* **350**, 1838-1849 (2004).

55. P. A. Halban, K. S. Polonsky, D. W. Bowden, M. A. Hawkins, C. Ling, K. J. Mather, A. C. Powers, C. J. Rhodes, L. Sussel, G. C. Weir, β-cell failure in type 2 diabetes: postulated mechanisms and prospects for prevention and treatment. *Journal of Clinical Endocrinology & Metabolism* **99**, 1983-1992 (2014).

56. R. Haliyur, X. Tong, M. Snayoura, S. Shrestha, J. Lindner, D. C. Saunders, R. Aramandla, G. Poffenberger, S. D. Redick, R. Bottino, N. Prasad, S. E. Levy, R. D. Blind, D. M. Harlan, L. H. Philipson, R. W. Stein, M. Brissova, A. C. Powers, Human islets expressing HNF1A variant have defective β cell transcriptional regulatory networks. *Journal of Clinical Investigation* **129**, 246-251 (2019).

57. N. J. Hart, R. Aramandla, G. Poffenberger, C. Fayolle, A. H. Thames, A. Bautista, A. F. Spigelman, J. A. B. Babon, M. E. DeNicola, P. K. Dadi, W. S. Bush, A. N. Balamurugan, M. Brissova, C. Dai, N. Prasad, R. Bottino, D. A. Jacobson, M. L. Drumm, S. C. Kent, P. E. MacDonald, A. C. Powers, Cystic fibrosis–related diabetes is caused by islet loss and inflammation. *Journal of Clinical Investigation Insight* **3**, (2018).

58. M. Lu, C. Li, Nutrient sensing in pancreatic islets: lessons from congenital hyperinsulinism and monogenic diabetes. *Annals of the New York Academy of Sciences* **1411**, 65 (2018).

59. R. N. Naylor, S. A. W. Greeley, G. I. Bell, L. H. Philipson, Genetics and pathophysiology of neonatal diabetes mellitus. *Journal of Diabetes Investigation* **2**, 158-169 (2011).

60. C. Talchai, S. Xuan, H. V. Lin, L. Sussel, D. Accili, Pancreatic β cell dedifferentiation as a mechanism of diabetic β cell failure. *Cell* **150**, 1223-1234 (2012).

61. R. H. Unger, A. D. Cherrington, Glucagonocentric restructuring of diabetes: a pathophysiologic and therapeutic makeover. *Journal of Clinical Investigation* **122**, 4-12 (2012).

62. V. L. Tokarz, P. E. MacDonald, A. Klip, The cell biology of systemic insulin function. *Journal of Cell Biology* **217**, 2273-2289 (2018).

63. E. Gylfe, P. Gilon, Glucose regulation of glucagon secretion. *Diabetes Research and Clinical Practice* **103**, 1-10 (2014).

64. J. W. Hughes, A. Ustione, Z. Lavagnino, D. W. Piston, Regulation of islet glucagon secretion: beyond calcium. *Diabetes, Obesity and Metabolism* **20**, 127-136 (2018).

65. Q. Yu, H. Shuai, P. Ahooghalandari, E. Gylfe, A. Tengholm, Glucose controls glucagon secretion by directly modulating cAMP in alpha cells. *Diabetologia* **62**, 1212-1224 (2019).

66. M. E. Capozzi, B. Svendsen, S. E. Encisco, S. L. Lewandowski, M. D. Martin, H. Lin, J. L. Jaffe, R. W. Coch, J. M. Haldeman, P. E. MacDonald, M. J. Merrins, D. A. D'Alessio, J. E. Campbell, β Cell tone is defined by proglucagon peptides through cAMP signaling. *Journal of Clinical Investigation Insight* **4**, (2019).

67. A. D. Elliott, A. Ustione, D. W. Piston, Somatostatin and insulin mediate glucose-inhibited glucagon secretion in the pancreatic α-cell by lowering cAMP. *American Journal of Physiology-Endocrinology and Metabolism* **308**, E130-E143 (2015).

68. B. Svendsen, O. Larsen, M. B. N. Gabe, C. B. Chistiansen, M. M. Rosenkilde, D. J. Drucker, J. J. Holst, Insulin secretion depends on intra-islet glucagon signaling. *Cell Reports* **25**, 1127-1134. e1122 (2018).

69. R. H. Unger, L. Orci, Paracrinology of islets and the paracrinopathy of diabetes. *Proceedings of the National Academy of Sciences* **107**, 16009-16012 (2010).

70. L. Zhu, D. Dattaroy, J. Pham, L. Wang, L. F. Barella, Y. Cui, K. J. Wilkins, B. L. Roth, U. Hochgeschwender, F. M. Matschinsky, K. H. Kaestner, N. M. Doliba, J. Wess, Intraislet glucagon signaling is critical for maintaining glucose homeostasis. *Journal of Clinical Investigation Insight* **4**, (2019).

71. M. Brissova, M. J. Fowler, W. E. Nicholson, A. Chu, B. Hirshberg, D. M. Harlan, A. C. Powers, Assessment of human pancreatic islet architecture and composition by laser scanning confocal microscopy. *Journal of Histochemistry & Cytochemistry* **53**, 1087-1097 (2005).

72. O. Cabrera, D. M. Berman, N. S. Kenyon, C. Ricordi, P. O. Berggren, A. Caicedo, The unique cytoarchitecture of human pancreatic islets has implications for islet cell function. *Proceedings of the National Academy of Sciences* **103**, 2334-2339 (2006).

73. C. Dai, M. Brissova, Y. Hang, C. Thompson, G. Poffenberger, A. Shostak, Z. Chen, R. Stein, A. C. Powers, Islet-enriched gene expression and glucose-induced insulin secretion in human and mouse islets. *Diabetologia* **55**, 707-718 (2012).

74. R. Rodriguez-Diaz, R. D. Molano, J. R. Weitz, M. H. Abdulreda, D. M. Berman, B. Leibiger, I. B. Leibiger, N. S. Kenyon, C. Ricordi, A. Pileggi, A. Caicedo, P. O. Berggren, Paracrine interactions within the pancreatic islet determine the glycemic set point. *Cell Metabolism* **27**, 549-558. e544 (2018).

75. N. S. Kayton, G. Poffenberger, J. Henske, C. Dai, C. Thompson, R. Aramandla, A. Shostak, W. Nicholson, M. Brissova, W. S. Bush, Powers A. C., Human islet preparations distributed for research exhibit a variety of insulin-secretory profiles. *American Journal of Physiology-Endocrinology and Metabolism* **308**, E592-E602 (2015).

76. B. N. Armbruster, X. Li, M. H. Pausch, S. Herlitze, B. L. Roth, Evolving the lock to fit the key to create a family of G protein-coupled receptors potently activated by an inert ligand. *Proceedings of the National Academy of Sciences* **104**, 5163-5168 (2007).

77. J. Wess, Use of designer G protein-coupled receptors to dissect metabolic pathways. *Trends in Endocrinology & Metabolism* **27**, 600-603 (2016).

78. D. C. Saunders, M. Brissova, N. Phillips, S. Shrestha, J. T. Walker, R. Aramandla, G. Poffenberger, D. K. Flahery, K. P. Weller, J. Pelletier, T. Cooper, M. T. Goff, J. Virostko, A. Shostak, E. D. Dean, D. L. Greiner, L. D. Shultz, N. Prasad, S. E. Levy, R. H. Carnahan, C. Dai, J. Sévigny, A. C. Powers, Ectonucleoside triphosphate diphosphohydrolase-3 antibody targets adult human pancreatic β cells for in vitro and in vivo analysis. *Cell Metabolism* **29**, 745-754. e744 (2019).

79. P. Gilon, M. Nenquin, J.-C. Henquin, Muscarinic stimulation exerts both stimulatory and inhibitory effects on the concentration of cytoplasmic Ca2+ in the electrically excitable pancreatic B-cell. *Biochemical Journal* **311**, 259-267 (1995).

80. J. L. Gomez, J. Bonaventura, W. Lesniak, W. B. Mathews, P. Sysa-Shah, L. A. Rodriguez, R. J. Ellis, C. T. Riche, B. K. Harvey, R. F. Dannals, M. G. Pomper, A. Bonci, M. Michaelides, Chemogenetics revealed: DREADD occupancy and activation via converted clozapine. *Science* **357**, 503-507 (2017).

81. K. S. Smith, D. J. Bucci, B. W. Luikart, S. V. Mahler, DREADDS: Use and application in behavioral neuroscience. *Behavioral Neuroscience* **130**, 137 (2016).

82. C. Dai, Y. Hang, A. Shostak, G. Poffenberger, N. Hart, N. Prasad, N. Phillips, S. E. Levy, D. L. Greiner, L. D. Shultz, R. Bottino, S. K. Kim, A. C. Powers, Age-dependent human β cell proliferation induced by glucagon-like peptide 1 and calcineurin signaling. *Journal of Clinical Investigation* **127**, 3835-3844 (2017).

83. S. Breslin, L. O'Driscoll, Three-dimensional cell culture: the missing link in drug discovery. *Drug Discovery Today* **18**, 240-249 (2013).

84. A. Ranga, N. Gjorevski, M. P. Lutolf, Drug discovery through stem cell-based organoid models. *Advanced Drug Delivery Reviews* **69**, 19-28 (2014).

85. N. J. Hart, A. C. Powers, Use of human islets to understand islet biology and diabetes: progress, challenges and suggestions. *Diabetologia* **62**, 212-222 (2019).

86. C. Ricordi, J. S. Goldstein, A. N. Balamurugan, G. L. Szot, T. Kin, C. Liu, C. W. Czarniecki, B. Barbaro, N. D. Bridges, J. Cano, W. R. Clarke, T. L. Eggerman, L. G. Hunsicker, D. B. Kaufman, A. Khan, D. E. Lafontant, E. Linetsky, X. Luo, J. F. Markmann, A. Naji, O. Korsgren, J. Oberholzer, N. A. Turgeon, D. Brandhorst, X. Chen, A. S. Friberg, J. Lei, L. J. Wang, J. J. Wilhelm, J. Willits, X. Zhang, B. J. Hering, A. M. Posselt, P. G. Stock, A. M. Shapiro, X. Chen, NIH-sponsored clinical islet transplantation consortium phase 3 trial: manufacture of a complex cellular product at eight processing facilities. *Diabetes*, db160234 (2016).

87. K. K. Papas, H. De Leon, T. M. Suszynski, R. C. Johnson, Oxygenation strategies for encapsulated islet and beta cell transplants. *Advanced Drug Delivery Reviews*, (2019).

88. L. Rosenberg, R. Wang, S. Paraskevas, D. Maysinger, Structural and functional changes resulting from islet isolation lead to islet cell death. *Surgery* **126**, 393-398 (1999).

89. D. W. Scharp, P. Marchetti, Encapsulated islets for diabetes therapy: history, current progress, and critical issues requiring solution. *Advanced Drug Delivery Reviews* **67-68**, 35-73 (2014).

90. K. Y. Lee, D. J. Mooney, Alginate: properties and biomedical applications. *Progress in Polymer Science* **37**, 106-126 (2012).

91. J. W. Haycock, 3D cell culture: a review of current approaches. *Methods in Molecular Biology* **695**, 1-15 (2011).

92. M. Lake, C. Narciso, K. Cowdrick, T. Storey, S. Zhang, J. Zartman, D. Hoelzle, Microfluidic device design, fabrication, and testing protocols. *Protocal Exchange* **10**, 1038 (2015).

93. R. Bottino, L. A. Fernandez, C. Ricordi, R. Lehmann, M. F. Tsan, R. Oliver, L. Inverardi, Transplantation of allogeneic islets of Langerhans in the rat liver: effects of macrophage depletion on graft survival and microenvironment activation. *Diabetes* **47**, 316-323 (1998).

94. C. W. Extrand, L. Monson, Gas permeation resistance of a perfluoroalkoxy-tetrafluoroethylene copolymer. *Journal of Applied Polymer Sci*ence **100**, 2122-2125 (2006).

95. J. Crank, *The mathematics of diffusion*. (Oxford University Press, 1979).

96. E. S. Avgoustiniatos, *Oxygen diffusion limitations in pancreatic islet culture and immunoisolation.* (Massachusetts Institute of Technology, 2002).

97. K. E. Dionne, C. K. Colton, M. Lyarmush, Effect of hypoxia on insulin secretion by isolated rat and canine islets of Langerhans. *Diabetes* **42**, 12-21 (1993).

98. M. M. Coronel, R. Geusz, C. L. Stabler, Mitigating hypoxic stress on pancreatic islets via in situ oxygen generating biomaterial. *Biomaterials* **129**, 139-151 (2017).

99. P. Rorsman, L. Eliasson, E. Renström, J. Gromada, S. Barg, S. Göpel, The cell physiology of biphasic insulin secretion. *Physiology* **15**, 72-77 (2000).

100. A. F. Adewola, D. Lee, T. Harvat, J. Mohammed, D. T. Eddington, J. Oberholzer, Y. Wang, Microfluidic perifusion and imaging device for multi-parametric islet function assessment. *Biomedical Microdevices* **12**, 409-417 (2010).

101. O. Cabrera, M. C. Jacques-Silva, D. M. Berman, A. Fachado, F. Echeverri, R. Poo, A. Khan, N. S. Kenyon, C. Ricordi, P. O. Berggren, A. Caicedo, Automated, high-throughput assays for evaluation of human pancreatic islet function. *Cell Transplantation* **16**, 1039-1048 (2007).

102. M. Adiraj Iyer, D. T. Eddington, Storing and releasing rhodamine as a model hydrophobic compound in polydimethylsiloxane microfluidic devices. *Lab on a Chip* **19**, 574-579 (2019).

103. A. L. Glieberman, B. D. Pope, J. F. Zimmerman, Q. Liu, J. P. Ferrier Jr., J. H. R. Kenty, A. M. Schrell, N. Mukhitov, K. L. Shores, A. B. Tepole, D. A. Melton, M. G. Roper, K. K. Parker, Synchronized stimulation and continuous insulin sensing in a microfluidic human Islet on a Chip designed for scalable manufacturing. *Lab on a Chip*, (2019).

104. E. Berthier, E. W. Young, D. Beebe, Engineers are from PDMS-land, Biologists are from Polystyrenia. *Lab on a Chip* **12**, 1224-1237 (2012).

105. K. Ren, W. Dai, J. Zhou, J. Su, H. Wu, Whole-Teflon microfluidic chips. *Proceedings of the National Academy of Sciences* **108**, 8162-8166 (2011).

106. J. D. Rivas-Carrillo, A. Soto-Gutierrez, N. Navarro-Alvarez, H. Noguchi, T. Okitsu, Y. Chen, T. Yuasa, K. Tanaka, M. Narushima, A. Miki, H. Misawa, Y. Tabata, H. S. Jun, S. Matsumoto, I. J. Fox, N. Tanaka, N. Kobayashi, Cell-permeable pentapeptide V5 inhibits apoptosis and enhances insulin secretion, allowing experimental single-donor islet transplantation in mice. *Diabetes* **56**, 1259-1267 (2007).

107. J. Y. Chan, G. J. Cooney, T. J. Biden, D. R. Laybutt, Differential regulation of adaptive and apoptotic unfolded protein response signalling by cytokine-induced nitric oxide production in mouse pancreatic beta cells. *Diabetologia* **54**, 1766-1776 (2011).

108. M. Garcia-Contreras, A. Tamayo-Garcia, K. L. Pappan, G. A. Michelotti, C. L. Stabler, C. Ricordi, P. Buchwald, Metabolomics study of the effects of inflammation, hypoxia, and high glucose on isolated human pancreatic islets. *Journal of Proteome Research* **16**, 2294-2306 (2017).

109. O. Alcazar, P. Buchwald, Concentration-dependency and time profile of insulin secretion: dynamic perifusion studies with human and murine islets. *Frontiers in Endocrinology* **10**, (2019).

110. J. S. Mohammed, Y. Wang, T. A. Harvat, J. Oberholzer, D. T. Eddington, Microfluidic device for multimodal characterization of pancreatic islets. *Lab on a Chip* **9**, 97-106 (2009).

111. M. Skelin Klemen, J. Dolenšek, M. Slak Rupnik, A. Stožer, The triggering pathway to insulin secretion: functional similarities and differences between the human and the mouse β cells and their translational relevance. *Islets* **9**, 109-139 (2017).

112. J. Pi, Q. Zhang, J. Fu, C. G. Woods, Y. Hou, Corkey B. E. S. Collins, M. E. Andersen, ROS signaling, oxidative stress and Nrf2 in pancreatic beta-cell function. *Toxicololgy and Applied Pharmacology* **244**, 77-83 (2010).

113. Y. J. Chen, T. Yamazoe, K. F. Leavens, F. L. Cardenas-Diaz, A. Georgescu, D. Huh, P. Gadue, B. Z. Stanger, iPreP is a three-dimensional nanofibrillar cellulose hydrogel platform for long-term ex vivo preservation of human islets. *Journal of Clinical Investigation Insight* **4**, e124644 (2019).

114. P. Gilon, M. A. Ravier, J. C. Jonas, J. C. Henquin, Control mechanisms of the oscillations of insulin secretion in vitro and in vivo. *Diabetes* **51**, S144-S151 (2002).

115. P. Bergsten, Glucose-induced pulsatile insulin release from single islets at stable and oscillatory cytoplasmic Ca2+. *American Journal of Physiology-Endocrinology and Metabolism* **274**, E796-E800 (1998).

116. C. S. Nunemaker, J. F. Dishinger, S. B. Dula, R. Wu, M. J. Merrins, K. R. Reid, A. Sherman, R. T. Kennedy, L. S. Satin, Glucose metabolism, islet architecture, and genetic homogeneity in imprinting of [Ca2+]i and insulin rhythms in mouse islets. *PLoS One* **4**, e8428 (2009).

117. H. L. Lanz, A. Saleh, B. Kramer, J. Cairns, C. P. Ng, J. Yu, S. J. Trietsch, T. Hankemeier, J. Joore, P. Vulto, R. Weinshilbourn, L. Wang, Therapy response testing of breast cancer in a 3D high-throughput perfused microfluidic platform. *BMC Cancer* **17**, 709 (2017).

118. E. L. Moreno, S. Hachi, K. Hemmer, S. J. Trietsch, A. S. Baumuratov, T. Hankemeier, P. Vulto, J. C. Schwamborn, R. M. Fleming, Differentiation of neuroepithelial stem cells into functional dopaminergic neurons in 3D microfluidic cell culture. *Lab on a Chip* **15**, 2419-2428 (2015).

119. M. Jang, P. Neuzil, T. Volk, A. Manz, A. Kleber, On-chip three-dimensional cell culture in phaseguides improves hepatocyte functions in vitro. *Biomicrofluidics* **9**, 034113-034113 (2015).

120. S. Bauer, C. Wennberg Huldt, K. P. Kanebratt, I. Durieux, D. Gunne, S. Andersson, L. Ewart, W. G. Haynes, I. Maschmeyer, A. Winter, C. Ämmälä, U. Marx, T. B. Andersson, Functional coupling of human pancreatic islets and liver spheroids on-a-chip: Towards a novel human ex vivo type 2 diabetes model. *Scientific Reports* **7**, 14620 (2017).

121. D. Huh, H. J. Kim, J. P. Fraser, D. E. Shea, M. Khan, A. Bahinski, G. A. Hamilton, D. E. Ingebr, Microfabrication of human organs-on-chips. *Nature Protocols* **8**, 2135-2157 (2013).

122. D. Huh, H. Fujioka, Y. C. Tung, N. Futai, R. Paine III, J. B. Grotberg, S. Takayama, Acoustically detectable cellular-level lung injury induced by fluid mechanical stresses in microfluidic airway systems. *Proceedings of the National Academy of Sciences* **104**, 18886-18891 (2007).

123. H. H. Chung, M. Mireles, B. J. Kwarta, T. R. Gaborski, Use of porous membranes in tissue barrier and co-culture models. *Lab on a Chip* **18**, 1671-1689 (2018).

124. C. G. Sip, N. Bhattacharjee, A. Folch, Microfluidic transwell inserts for generation of tissue culture-friendly gradients in well plates. *Lab on a Chip* **14**, 302-314 (2014).

125. O. T. Guenat, F. Berthiaume, Incorporating mechanical strain in organs-on-a-chip: Lung and skin. *Biomicrofluidics* **12**, 042207 (2018).

126. B. Srinivasan, A. R. Kolli, M. B. Esch, H. E. Abaci, M. L. Shuler, J. J. Hickman, TEER measurement techniques for in vitro barrier model systems. *Journal of Laboratory Automation* **20**, 107-126 (2015).

127. M. A. Saleem, M. J. O'Hare, J. Reiser, R. J. Coward, C. D. Inward, T. Farren, C. Y. Xing, L. Ni, P. W. Mathieson, P. Mundel, A conditionally immortalized human podocyte cell line demonstrating nephrin and podocin expression. *Journal of the American Society of Nephrology* **13**, 630-638 (2002).

128. S. Musah, A. Mammoto, T. C. Ferrante, S. S. F. Jeanty, M. Hirano-Kobayashi, T. Mammoto, K. Roberts, S. Chung, R. Novak, M. Ingram, T. Fatanat-Didar, S. Koshy, J. C. Weaver, G. M. Church, D. E. Ingber, Mature induced-pluripotent-stem-cell-derived human podocytes reconstitute kidney glomerular-capillary-wall function on a chip. *Nature Biomedical Engineering* **1**, 1-12 (2017).

129. W. Lu, E. P. Lillehoj, K. C. Kim, Effects of dexamethasone on Muc5ac mucin production by primary airway goblet cells. *American Journal of Physiology-Lung Cellular and Molecular Physiology* **288**, L52-L60 (2005).

130. A. Olivera, S. Spiegel, Sphingosine-1-phosphate as second messenger in cell proliferation induced by PDGF and FCS mitogens. *Nature* **365**, 557-560 (1993).

131. A. Kaipia, S. Y. Chun, K. Eisenhauer, A. J. Hsueh, Tumor necrosis factor-alpha and its second messenger, ceramide, stimulate apoptosis in cultured ovarian follicles. *Endocrinology* **137**, 4864-4870 (1996).

132. S. Merscher, A. Fornoni, Podocyte pathology and nephropathy - sphingolipids in glomerular diseases. *Frontiers in Endocrinology* **5**, 127 (2014).

133. M. Maceyka, K. B. Harikumar, S. Milstien, S. Spiegel, Sphingosine-1-phosphate signaling and its role in disease. *Trends in Cell Biology* **22**, 50-60 (2012).

134. P. T. Brinkkoetter, C. Ising, T. Benzing, The role of the podocyte in albumin filtration. *Nature Reviews Nephrology* **9**, 328-336 (2013).

135. L. Ewart, E. M. Dehne, K. Fabre, S. Gibbs, J. Hickman, E. Hornberg, M. Ingelman-Sundberg, K. J. Jang, D. R. Jones, V. M. Lauschke, U. Marx, J. T. Mettetal, A. P, ointon, D. Williams, W. H. Zimmerman, P. Newham, Application of microphysiological systems to enhance safety assessment in drug discovery. *Annual Review of Pharmacology and Toxicology* **58**, 65-82 (2018).

136. L. Ewart, K. Fabre, A. Chakilam, Y. Dragan, D. B. Duignan, J. Eswaraka, J. Gan, P. Guzzie-Peck, M. Otieno, C. G. Jeong, D. A. Keller, S. M. de Morais, J. A. Phillips, W. Proctor, R. Sura, Y. Van Vleet, D. Watson, Y. Will, D. Tagle, B. Berridge, Navigating tissue chips from development to dissemination: A pharmaceutical industry perspective. *Experimental Biology and Medicine* **242**, 1579-1585 (2017).

137. D. A. Dunn, I. Feygin, Challenges and solutions to ultra-high-throughput screening assay miniaturization: submicroliter fluid handling. *Drug Discovery Today* **5**, S84-S91 (2000).

138. B. Zhang, A. Korolj, B. F. L. Lai, M. Radisic, Advances in organ-on-a-chip engineering. *Nature Reviews Materials* **3**, 257-278 (2018).

139. A. Junaid, A. Mashaghi, T. Hankemeier, P. Vulto, An end-user perspective on organ-on-a-chip: assays and usability aspects. *Current Opinion in Biomedical Engineering* **1**, 15-22 (2017).

140. B. Zhang, M. Radisic, Organ-on-a-chip devices advance to market. *Lab on a Chip* **17**, 2395-2420 (2017).

141. B. J. O'Grady, J. X. Wang, S. L. Faley, D. A. Balikov, E. S. Lippman, L. M. Bellan, A Customizable, Low-Cost Perfusion System for Sustaining Tissue Constructs. *SLAS Technology* **23**, 592-598 (2018).

APPENDICES

APPENDIX A1. SETUP AND OPERATION OF CNC MILLING MACHINE

This protocol describes how to prepare and run the CNC Milling Machine and Acrylic Workpiece.

METHODS

1) **RECORD YOUR NAME, THE DATE, MATERIAL YOU'RE WORKING WITH, AND TOOLS USED IN THE LOGBOOK LOCATED ON THE TOP OF THE MILLING MACHINE. IN THE NOTES SECTION, RECORD THE AVERAGE THICKNESS OF YOUR MATERIAL.**
2) Turn on the air compressor that is located below the MDX-540S Milling Machine (turn the red switch to the horizontal position).
3) Open the valve on the air compressor, by turning the gold-colored knob.
4) Turn on the MDX-540S Milling Machine using the power switch, found on the front part of the machine, to the right of the red EMERGENCY STOP button.
5) Press ENTER/PAUSE on the Machine's User Interface panel, found hanging on the right side of the machine.
6) Open the program VPanel for MODELA PRO II.
7) Measure the tools:
   a) Click the Magazine icon, found on the top of the program page.

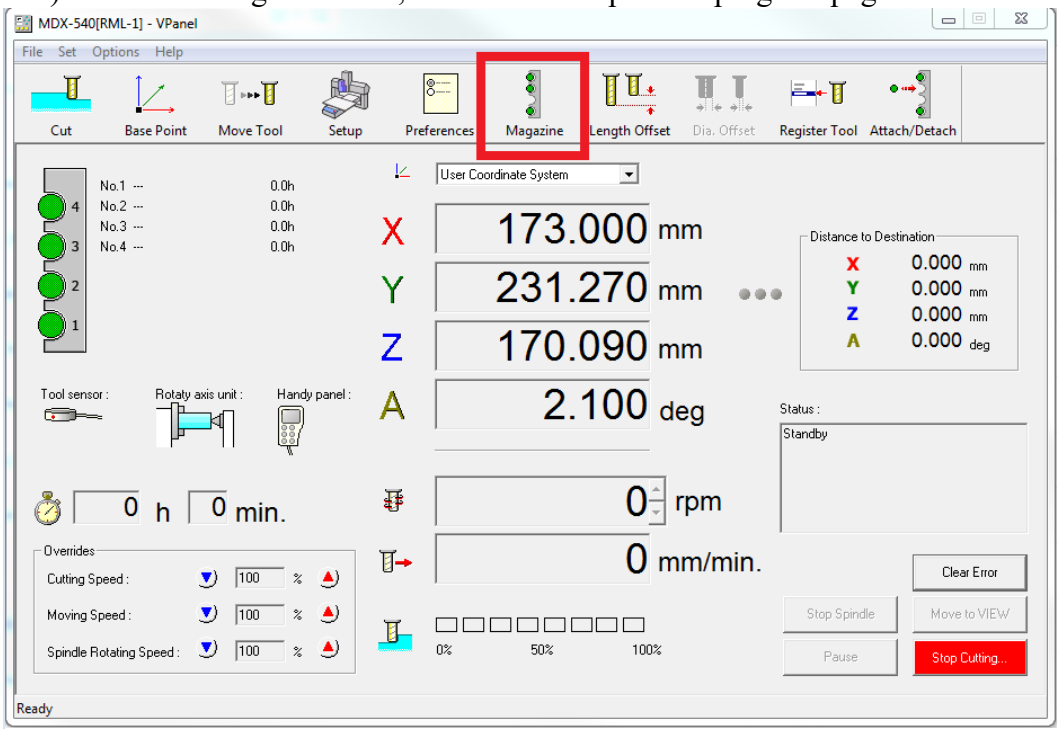

   b) Click on Measure All, found on the bottom part of the screen.

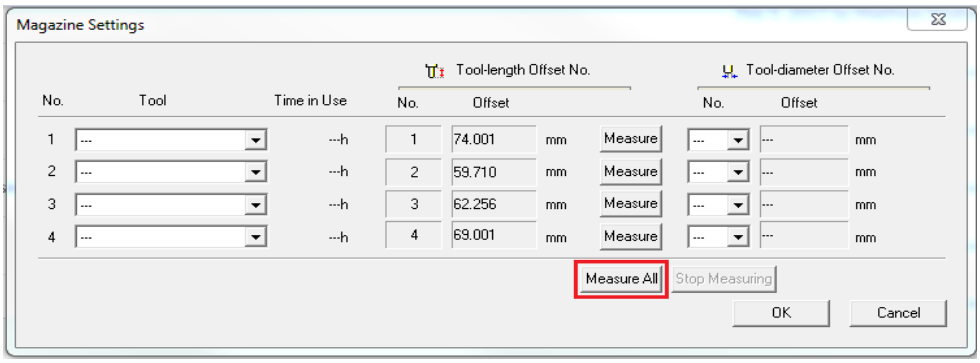

8) Set the Origins.
   a) Setting the A (angle) must be done manually as there is a slight difference between the User and Machine Coordinate Systems.
      i) Select the COORD. SYSTEM button on the top left, until you see that you are in the USER Coordinate System, displayed in the top left of the screen. It will either display USER or MACHINE.

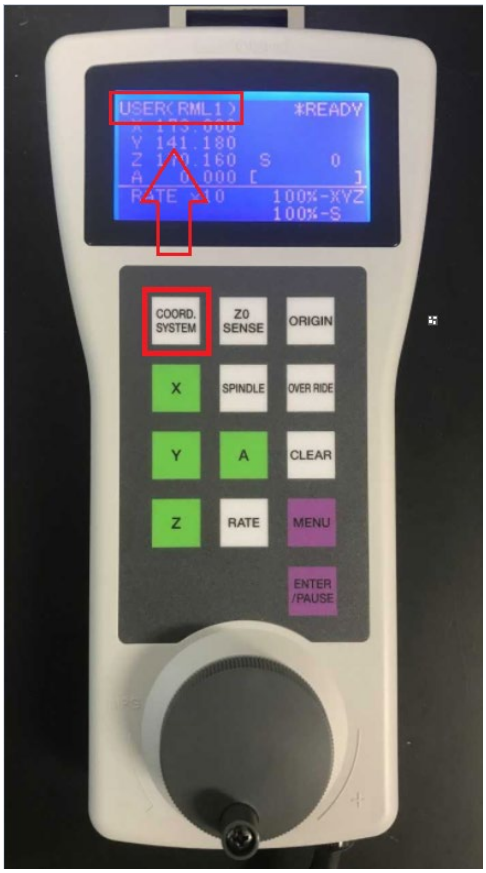

      ii) Click on the A button and rotate the slider to the left until you see that the USER coordinate system next to A reads 0.000. You may have to hit the RATE button (located below the A button) to change how large each step down will be, until you have achieved the desired 0.000.

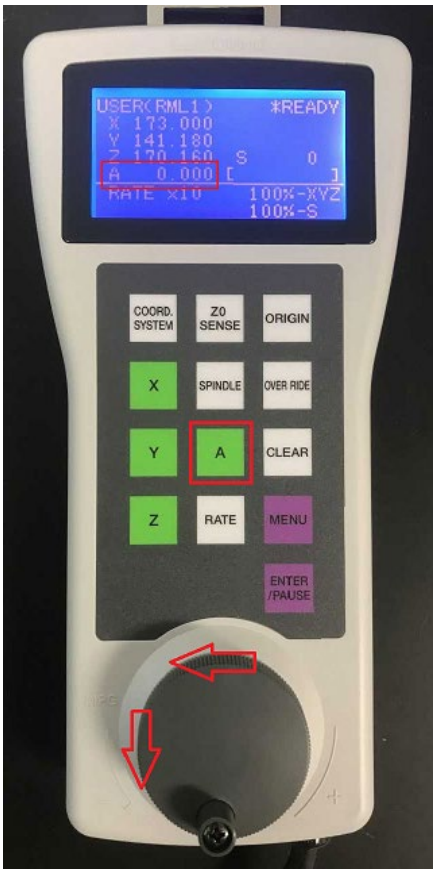

iii) When this is done, you will see that, if you select the COORD. SYSTEM button again, the MACHINE Coordinate System reads A 358.100.

iv) Once this is done, hold down the ORIGIN button until you hear a beep.

b) The Milling Machine will automatically set the X axis.

c) Set the Y axis:

i) Click on Base Point, found at the top-left of the screen.

ii) From the drop-down menu, select Y Origin.

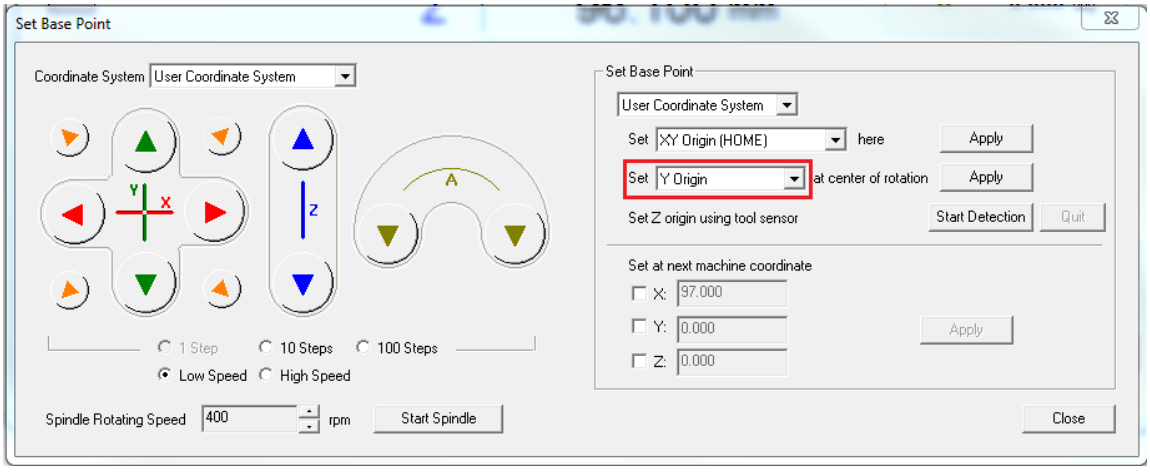

iii) Hit Apply, immediately to the right of this menu.

d) Set the Z axis:
   i) From the same drop-down menu used in the previous step, select Z origin and hit apply.
   ii) A pop-up will appear saying to, “Attach the sensor cable to the Z-origin sensor.” Select OK.
   iii) Attach the tool in position 1 to set your Z origin. To do this, go to Attach/Detach in the top-right corner.

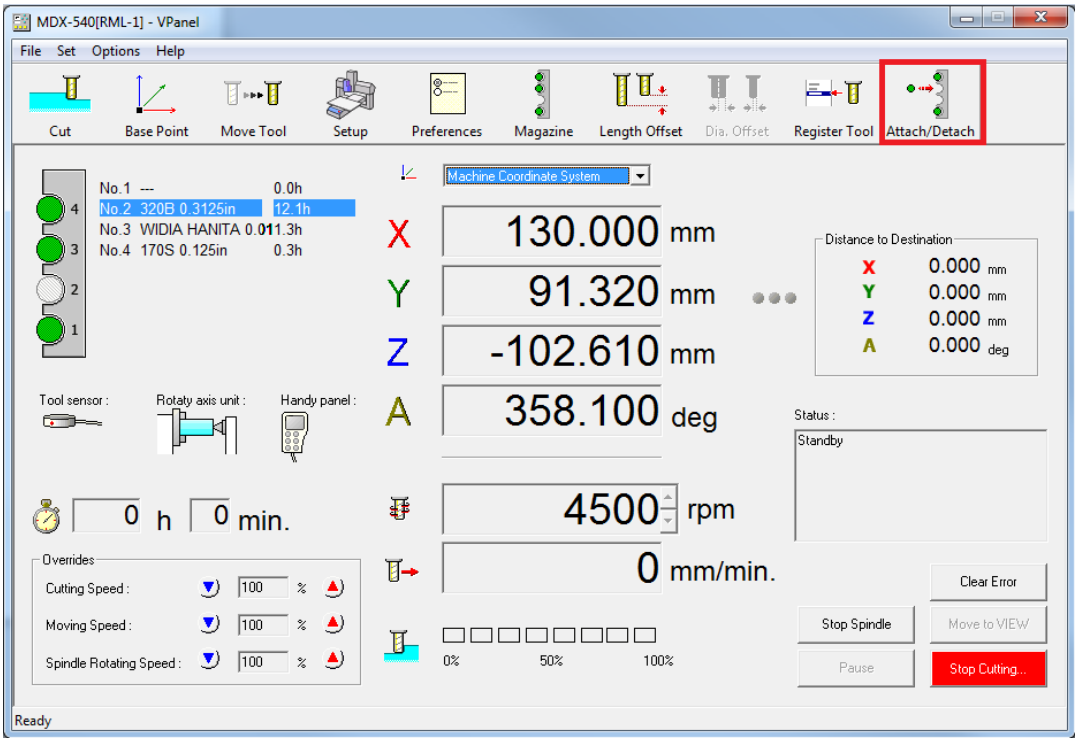

   iv) Make sure to select Stocker No. 1, then hit Replace.

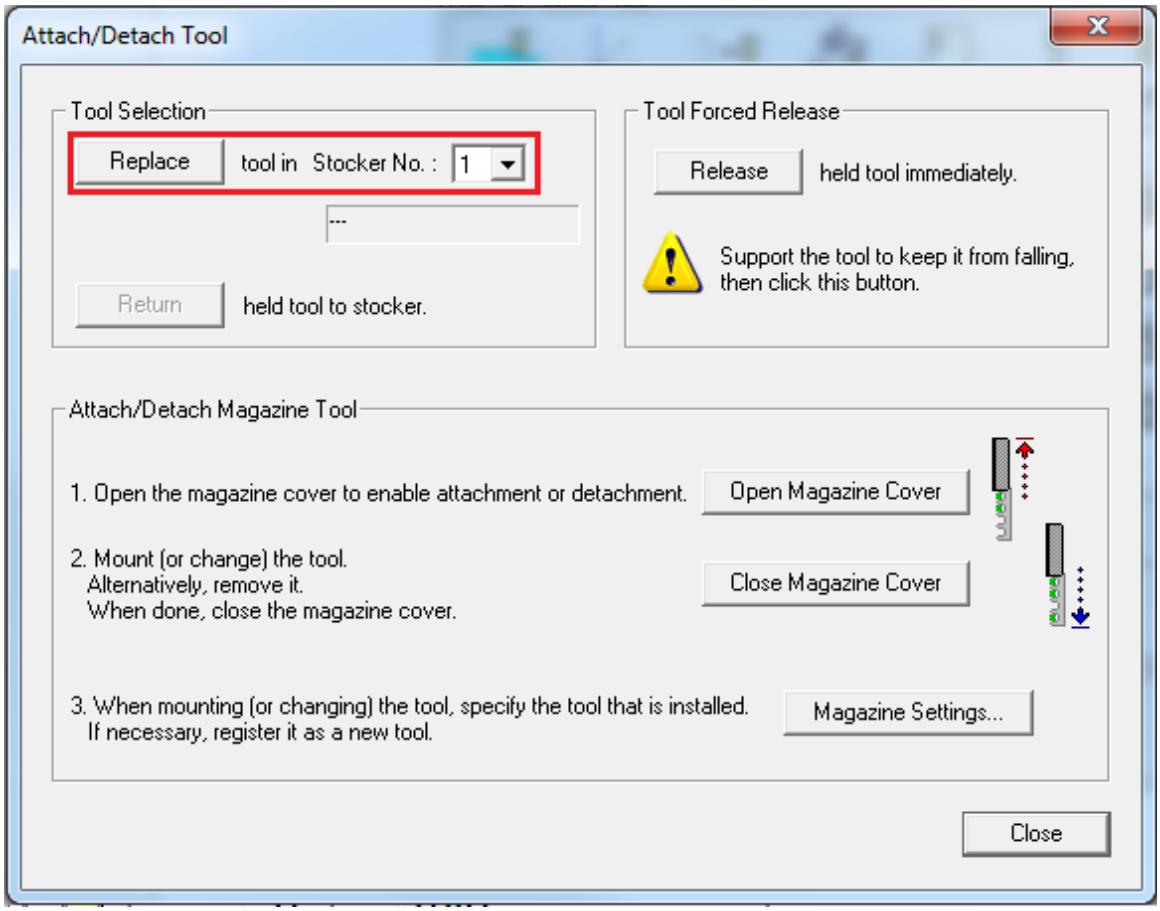

v) Once it has finished setting the Z Origin, go back to Attach/Detach. This time, instead of hitting Replace, select Return.

9) Measuring Acrylic Workpiece.
   a) Measure each of the four corners to see how thick your Workpiece is.
   b) Keeping these measurements in mind, put your workpiece into the Milling Machine.
      i) To do this, you will use a Plastic Holder that helps put the Workpiece uniformly into the Milling Machine each time.
      ii) After you place the Workpiece into the Plastic Holder, place the Plastic Holder into the Milling Machine making sure that the back of the Plastic Holder is flush with the with the area designated in the Milling Machine.

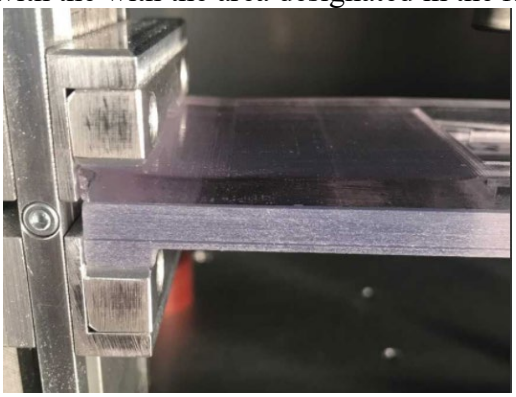

(1) Note the orientation of the Plastic Holder in the Machine.

(2) On the left side of the holder, the clearest piece of plastic should be on the top.

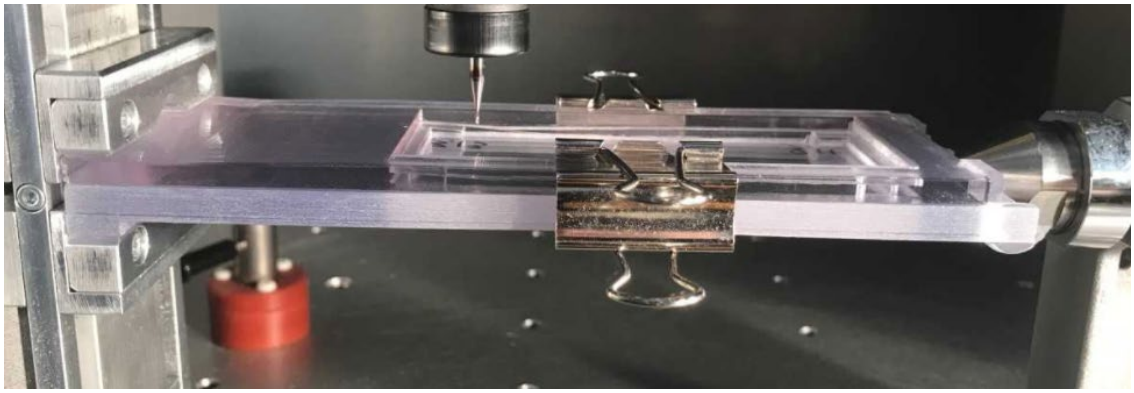

(3) Another way to check for proper orientation, is to make sure that on the right side of the holder, the hemisphere looking pieces are facing the bottom.

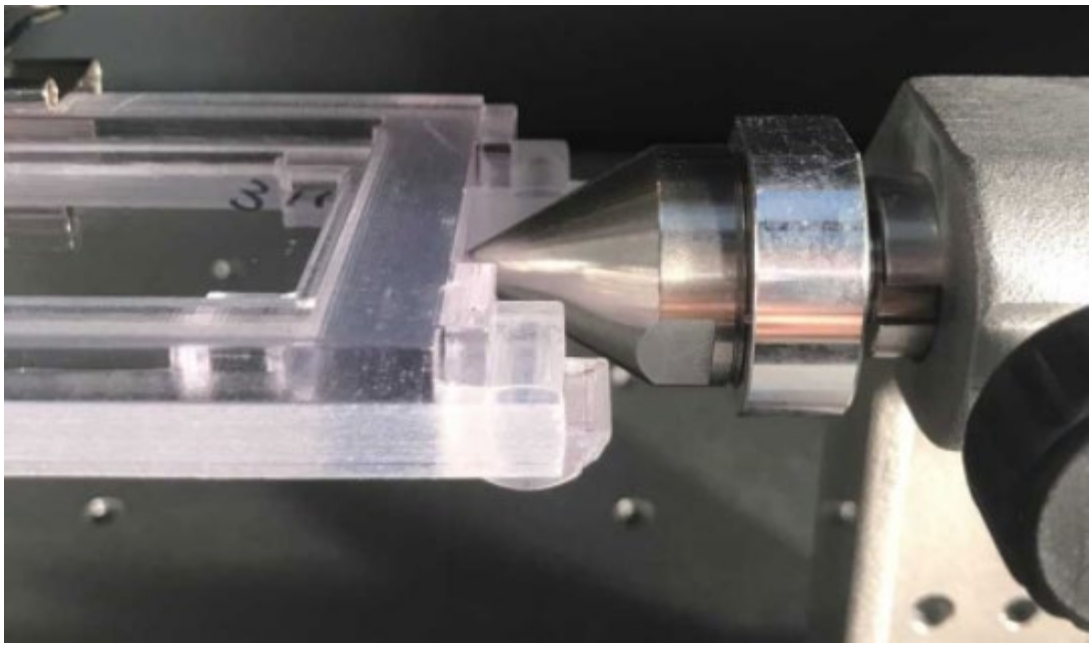

iii) Tighten each of the three different knobs around the Plastic Holder with nothing more than finger weight. This means that you should not be gripping too tight while trying to tighten the Plastic Holder in place, as this can cause discrepancies later in the measuring process and damage the pieces in the Milling Machine.

c) Attach the tool (Attach/Detach) in Stocker No. 2.

d) Set the speed of the Milling Machine to 4,500RPM by selecting SPINDLE and rotating the slider to the right to increase speed until the number next to S is 4,500.

e) **CAREFULLY** lower the Milling Tool down to the very top of the workpiece, on the right side of the workpiece (you lower the Milling Tool by rotating the slider to the left).
   i) The X axis should be somewhere near -19.000.
   ii) The Y axis should be 0.000
   iii) The Z axis (height) is what you are trying to measure. It should be at approximately half the total height of the measured acrylic.

f) As you near the Workpiece, select Rate to lessen the amount that you decrease with each step (making you more precise).

g) Once the Milling Tool barely makes contact with the top of the Workpiece, as seen by a small buildup of acrylic around the tip of the tool, note the height of the Z axis.

h) Repeat steps e, f and g on the left side of the Workpiece.
   i) The X axis should be at -97.000 (it will not go any farther).
   ii) The Y axis should be at 0.000.
   iii) The Z axis (height) is what you are trying to measure. It should be at approximately half the total height of the measured acrylic.

i) Insert pieces of paper (approximately 80 microns in height) to the bottom of the apparatus (on whichever side it would be appropriate) to make up for discrepancies in height.

j) Repeat this process as necessary until the different in height between the left and right sides is less than 50 microns.

i) Keep in mind that as you continue to do this, you should change your X and Y axis to make sure that you are not lowering the Milling Tool into formerly drilled holes.

10) Loading the Steps.

a) Select Cut, at the top left of the screen.

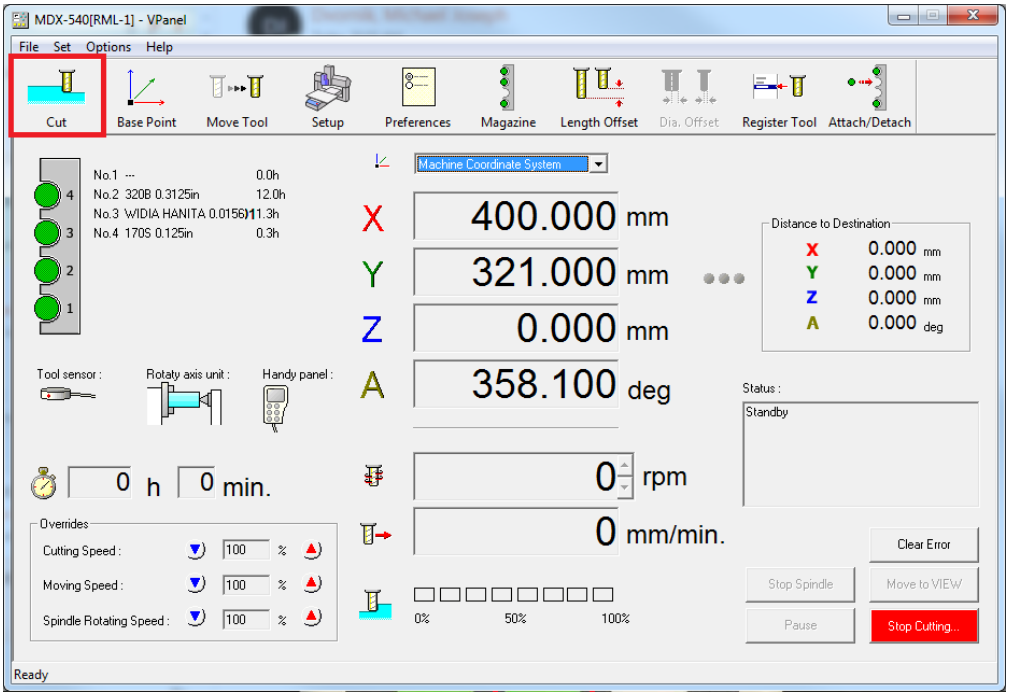

b) Select Open, on the following screen to decide what files you would like to output to the Milling Machine.

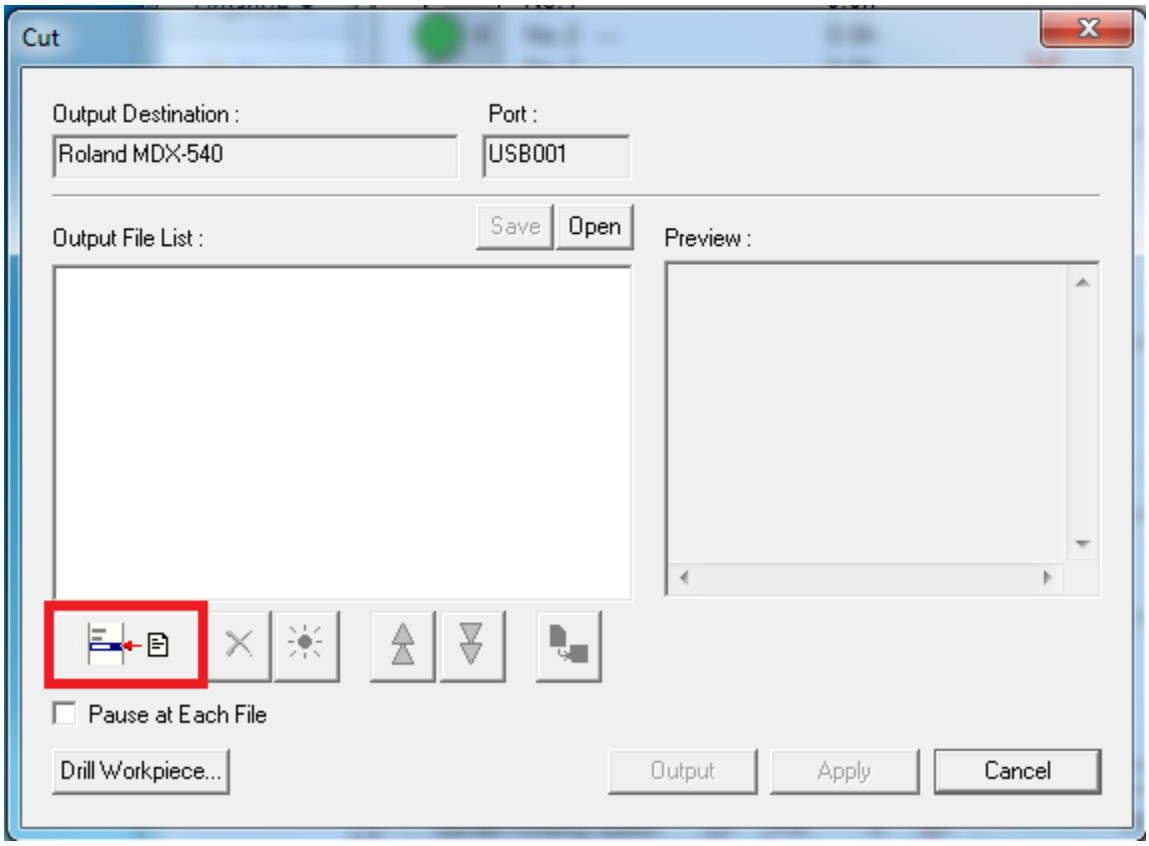

i) These files can be found from in Box.com (PML>Islet Microdevice>Design & Fabrication>Current Design>CNC CAD) you are shared with, or on the computer itself.
ii) You will see multiple files named with varying heights. Select the file whose name is closest to the height measured with the use of the Milling Machine (twice the measured Z axis).
iii) Copy and paste these files into the Output File List. Ensure that while copying these files over, they still appear in number order. Then select Apply.

11) The Milling Process.
   a) Occasionally during the Milling Process, use the vacuum located below the Milling Machine to vacuum up the acrylic waste that results from the Milling Process. Be careful not to hit the Workpiece or the Milling Machine in this process.

12) Extraction of the Workpiece.
   a) If the Milling Machine was fabricating the top piece of the Fluidic Chip, the estimated time of completion would be around 1 hour and 45 minutes.
   b) If the Milling Machine was fabricating the bottom piece of the Fluidic Chip, the estimated time of completion would be around 2 hours and 30 minutes.
   c) Before extracting the Plastic Holder from the Milling Machine, vacuum all of the residual acrylic from the Milling Process.
   d) Using the User Interface Panel on the right side of the Milling Machine, select A (Angle) and rotate the Plastic Holder by 180 degrees, as the Milling Machine will finish the Workpiece on the bottom side.

e) Untighten the Plastic Holder from the Milling Machine by twisting each of the three knobs that keep the Plastic Holder in place.
f) Remove the Workpiece from the Plastic Holder, and the Workpiece is now ready to be laser cut to the dimensions of the Fluidic Chip.
g) **ENSURE YOUR NAME, MATERIAL YOU WORKED WITH, AND DURATION OF MILLING MACHINE RUN TIME ARE RECORDED IN THE LOG LOCATED ON THE TOP OF THE MILLING MACHINE.**

APPENDIX A2. ANALYSIS OF CONFOCAL μPIV DATA

This protocol describes how to perform micro-particle image velocimetry (μPIV) analysis on a sequence of images using the PIVLab App for MATLAB.

Generate Image Sequences

Download and Install Fiji: ImageJ

Save Image Sequence

1. Open video recorded from microscope in ImageJ.
2. Click “Analyze” > “Tools” > “Scale Bar”
    a. Set the width in microns to 100, the color to Red, and check the “Label all slices” box, click OK.
3. File > Save As > Image Sequence… (Save as .tif)

PIVLab Analysis

Download and Install PIVLab

Import Image Sequence

1. Run “PIVlab_GUI.m”
2. (This depends on the format you saved your files, if you saved as .tif you can skip) Click on the “Load Images” button and under “Reg. Exp. Filter” replace one of the image formats to “.png”
    a. For example: “\.bmp$|\.jpg$|\.png$|\.jpeg$|\.tiff$”
3. Change the current directory to where you saved your frames and select the folder of frames you want to use.

4. A list of frames should appear now. Select all the frames using shift + arrow keys. Once selected click ADD →. Then select import.

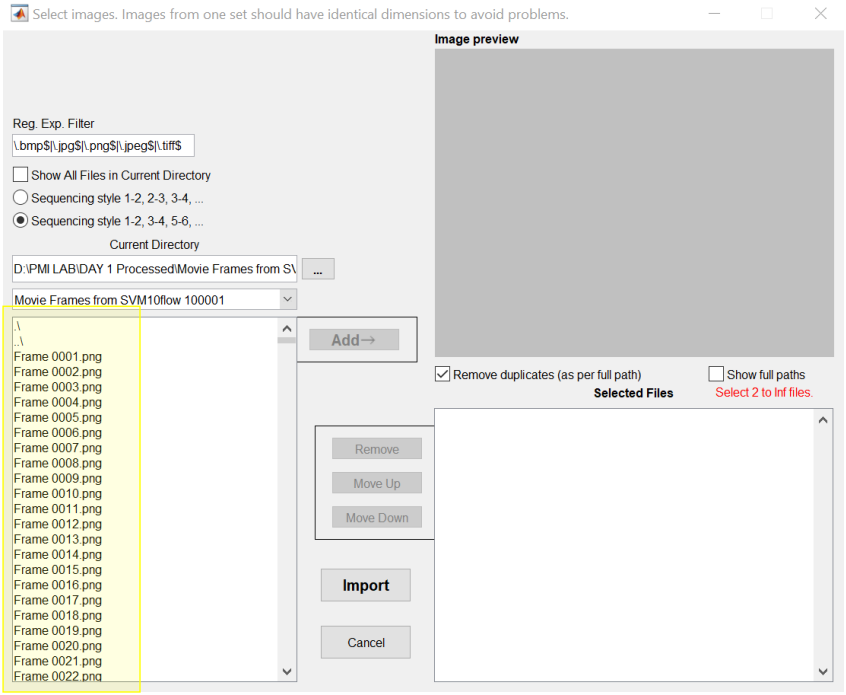

PIV Analysis Setup

1. Before analyzing, go to “Image Settings” at the top, and select “Exclusions (ROI, mask)”.
    a. Here you can select your ROI and draw it on the image.
    b. If you have an area that is in the ROI and you want to exclude data from there, select “Draw mask(s) for current frame”, draw the mask(s) on the area, and then select “Apply current mask(s) to frames…”
2. Click on the “Analysis” tab at the top and select “PIV settings”
    a. Here you set the “PIV algorithm” to “FFT window deformation”
        i. The passes is as follows. The first pass should be 4 times the distance of your displacement therefore you usually will get passes of:
    b. Set the passes to the following:

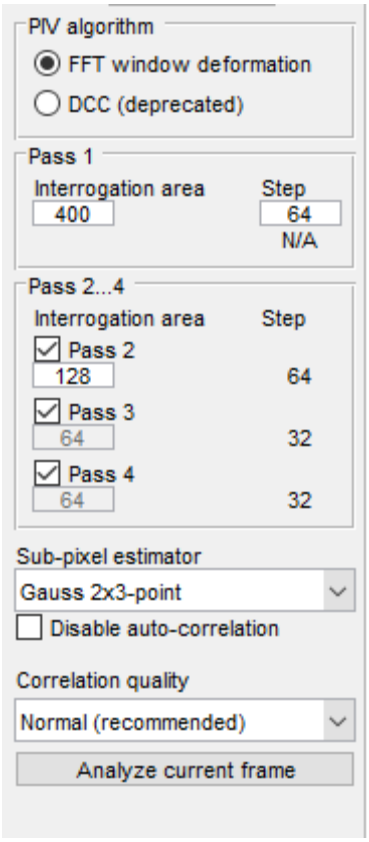

3. Click on the “Analysis” tab at the top, select “ANALYZE!”, and select “Analyze all frames”.

Calibration and Post-Process

1. After the analysis is complete, click the “Calibration” tab and select “Calibrate using current or external frame”.
    a. Use a fixed point that you know the length of. In our case we know the red scale in each pictures’ measurement so we can use that. The step interval (FPS) depends on the period divided by the amount of the frames extracted. We set the parameters and use the “Select reference distance” to measure the red scale.
    b. Hit “Apply Calibration” once you measure the bead.
2. After Calibration, go to the “Post-processing” tab and select “Vector validation”.
    a. Click on “Select velocity limits” and draw a square around the data, excluding outliers that could be caused by noise.
    b. Note: Do not exclude negative values.
3. After Calibration we will go into the “Plot” tab and select “Derive parameters / modify data”
    a. Check on the “Smooth data” box and Apply to all frames.

Export Data

1. Go to “Extractions” tab:
    a. Change “type” to “Area mean value”
    b. Change Parameter to “Velocity magnitude [m/s]”
    c. Click the check on both “save result as test (ASCII)…” and “Do and save extractions for all frames.”
    d. “Draw area” the size of the ROI.
    e. Click enter and save your file in desired location. Filename should be: '30ul ZXXXX vel.txt'
2. Go to “File” tab:
    a. Go to “Save” and click “PIVlab session”; save in desired location. (This file will be used to construct Velocity and Shear Stress plot)
    b. Go to “Save” and click “Text file (ASCII)” (This file will be used to conduct 3D plot)
        i. Check “Add file information” and “Add column headers”
        ii. Change Delimiter to “space”
        iii. Export current frame. Save in desired location. Filename should be: '30ulZXXXX.txt'

APPENDIX A3. qPCR ANALYSIS OF KIDNEY ORGANOIDS

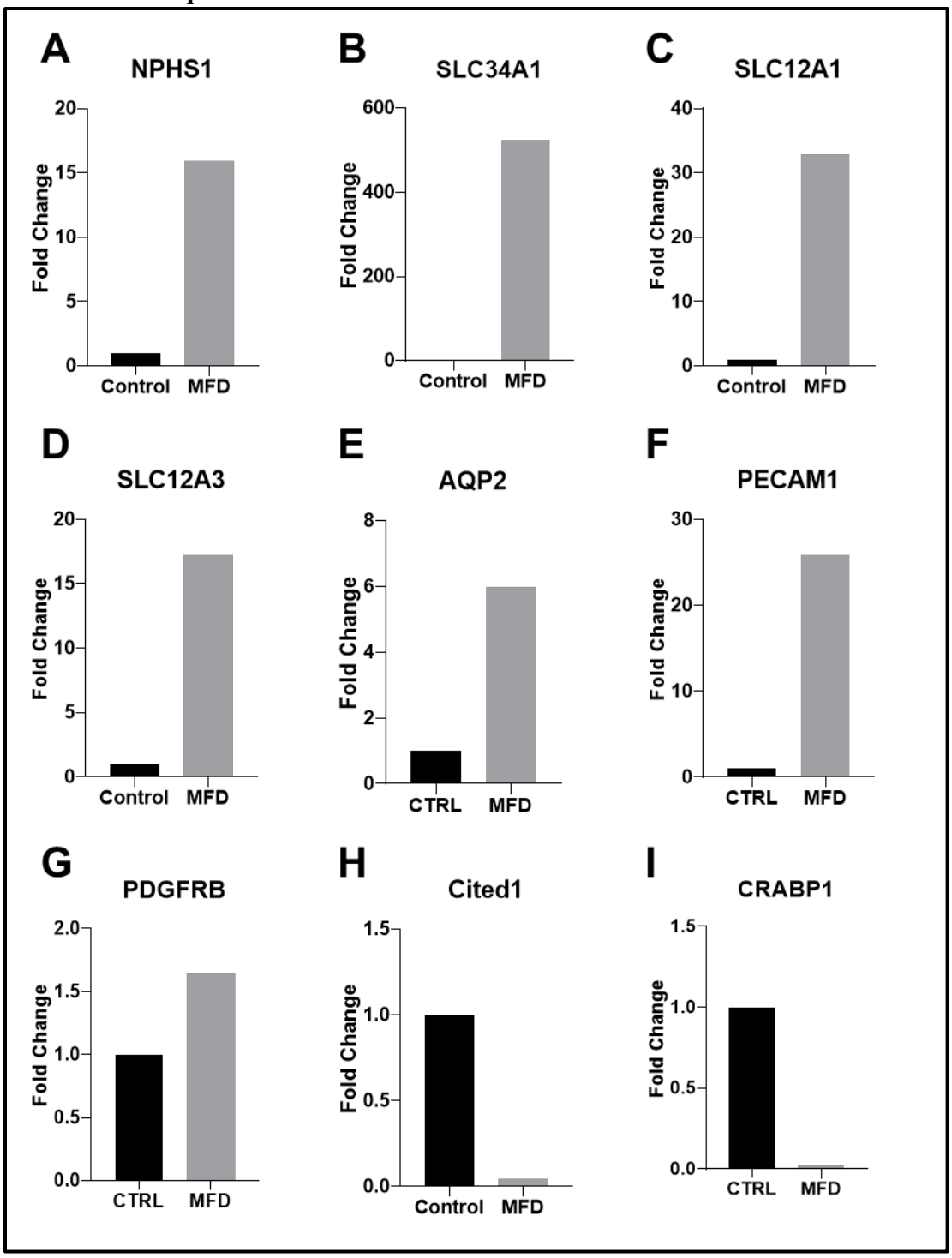

Fold change in expression of various differentiation and maturation markers after generating kidney organoids in static culture (CTRL) and the microfluidic device with a flow rate of 100 µL/min (MFD). (A) Glomerular marker, Nephrin (NPHS1) (B) Proximal

tubule sodium transporter, SCL34A (C) Loop of Henle marker, SLC12A1 (D) Distal tubule marker, SLC12A3 (E) Collecting duct aquaporin 2, AQP2 (F) Endothelial marker, PECAM1 (G) Pericyte marker, PDGFRB (H) Developing kidney marker, Cited1 (I) Neuronal marker for off-target differentiation, CRABP1 ; n=1. *PCR was performed and analyzed by the Humphreys Lab at Washington University in St. Louis.*

APPENDIX A4. CALCIUM IMAGING VIDEOS

Video 1 – Calcium imaging of hM3Dq Pseudoislet in response to glucose

Download Here:

https://miami.app.box.com/file/627401551564

Video 2 – Calcium imaging of hM3Dq Pseudoislet in response to glucose and CNO

Download Here:

https://miami.app.box.com/file/627428742282

APPENDIX A5. COMSOL MODELING PARAMETERS

	Parameter	Static Culture	Acry-Chip	Oxy-Chip
Geometry	Islet Radius		7.5×10^{-5} m	
	Culture Well Width	0.011 m	0.004 m	0.004 m
	Culture Well Height	0.002 m	0.0015 m	0.0015 m
	Hydrogel Width	0.00264 m	0.004 m	0.004 m
	Hydrogel Height	0.00158 m	0.00149 m	0.00149 m
	Device Length	n/a	0.014 m	0.014 m
	Device Height	n/a	0.002 m	0.002 m
	Channel length	n/a	0.005 m	0.005 m
	Obstacle length	n/a	0.003 m	0.003 m
	Obstacle height	n/a	0.0005 m	0.0005 m
	PFA Membrane Thickness	n/a	n/a	2.5×10^{-5} m
	Chamfer	n/a	0.0005 m	0.0005 m
Mass Transport	Inlet Velocity	n/a	0.0016667 m/s	
	Diffusion Coefficient, Glucose in Fluid		9×10^{-10} m^2/s	
	Diffusion Coefficient, Glucose in Islets		3×10^{-10} m^2/s	
	Diffusion Coefficient, Glucose in Hydrogel		6x10-10 m2/s	
	Diffusion Coefficient, Oxygen in Fluid		3×10^{-9} m^2/s	
	Diffusion Coefficient, Oxygen in Islets		2×10^{-9} m^2/s	
	Diffusion Coefficient, Oxygen in Hydrogel		2.5×10^{-9} m^2/s	
	Diffusion Coefficient, Oxygen in PFA	n/a	n/a	5.6×10^{-11} m^2/s
	Diffusion Coefficient, Insulin in Fluid		1.5×10^{-10} m^2/s	
	Diffusion Coefficient, Insulin in Islets		0.5×10^{-10} m^2/s	
	Diffusion Coefficient, Insulin in Hydrogel		1×10^{-10} m^2/s	
	Glucose Concentration in Media		5.5 mol/m^3	
	Oxygen Concentration		0.18 mol/m^3	
Islet Physiology	Maximum Oxygen Consumption Rate		-0.034 $mol/s/m^3$	
	Maximum Glucose Consumption Rate		-0.028 $mol/s/m^3$	
	Insulin Release Rate Constant		3×10^{-3} 1/s	
	Maximum First Phase Insulin Secretion Rate		10×10^{-5} $mol/s/m^3$	
	Maximum Second Phase Insulin Secretion Rate		1.8×10^{-5} $mol/s/m^3$	

APPENDIX A6. PART LIST AND PRICE BREAKDOWN FOR INTEGRATED PLATFORM

Part	Description	Supplier Part #	Supplier	Quantity	Size	Price	Units	Unit Price
XY Stage								
Stepper Motor	NEMA17 Stepper Motor Hybrid Bipolar 12V	1568-1105-ND	Digikey	1	each	$ 14.95	2	$ 29.90
Motor Bracket	3PCS Alloy Steel L Bracket for Nema 17		Amazon	3	pack	$ 10.99	2	$ 7.33
Shaft Coupler	FYSETC Coupler 5mm to 8mm Nema 17 Motor Shaft	Coupler 5-8mm	Amazon	1	each	$ 10.99	2	$ 21.98
Lead Screw	Ultra-Precision, Alloy Steel, M8 x 1.5mm Thread, 300mm Long	7549K57	McMaster	1	each	$ 71.05	2	$ 142.10
Nut	Acetal Plastic M8 x 1.5mm Pitch Flange Nut	7549K64	McMaster	5	pack	$ 14.48	2	$ 5.79
Rail	Carriage Guide Rail (250 mm)	9867K124	McMaster	1	each	$ 17.50	2	$ 35.00
Rail	Carriage Guide Rail (500 mm)	9867K122	McMaster	1	each	$ 35.00	1	$ 35.00
Carraige	Sleeve Bearing Carriage for 15 mm Wide Rail, 47 mm Wide	9867K2	McMaster	1	each	$ 51.11	3	$ 153.33
Limit Switch	Precision Snap Acting Switch	480-2324-ND	Digikey	1	each	$ 9.36	2	$ 18.72
Power Supply Circuits								
Power Supply	AC/DC Desktop Adapter 24V 160W	1866-2047-ND	Digikey	1	each	$ 59.66	1	$ 59.66
Power Port	4 (Power) Position Circular Connector Jack	2092-KPJX-PM-4S-S-ND	Digikey	1	each	$ 2.64	1	$ 2.64
Barrel Connector	Power Barrel Connector Plug 2.5X5.5MM	CP3-1001-ND	Digikey	1	each	$ 1.04	1	$ 1.04
Converter	DC DC CONVERTER 12V 12W	1951-2251-ND	Digikey	1	each	$ 37.30	1	$ 37.30
Converter	DC DC CONVERTER 5V 7.5W	1951-2714-ND	Digikey	1	each	$ 30.30	1	$ 30.30
Power Switch	Rocker Switch SPST 20A (AC/DC) 250V Panel Mount, Snap-In	1091-1139-ND	Digikey	1	each	$ 4.02	1	$ 4.02
Relay	RELAY GEN PURPOSE DPDT 5A 24V	255-1118-ND	Digikey	1	each	$ 3.94	1	$ 3.94
Transistor	Bipolar (BJT) Transistor NPN 40V 200mA 300MHz 625mW	2N3904FS-ND	Digikey	1	each	$ 0.21	3	$ 0.63
Diode	DIODE GEN PURP 250MA SOD323	BAS316RRGCT-ND	Digikey	1	each	$ 0.11	1	$ 0.11
OpAmp	IC OPAMP GP 1MHZ 8DIP	LM358NNS/NOPB-ND	Digikey	1	each	$ 0.84	1	$ 0.84
Resistor	RES 0.1 OHM 20W 1% TO220	PWR220T-20-R100F-ND	Digikey	1	each	$ 4.20	1	$ 4.20
Resistor	RES 1K OHM 1% 1/2W 1206	RNCP1206FTD1K00CT-ND	Digikey	1	each	$ 0.10	2	$ 0.20
Resistor	RES 10K OHM 1% 1/2W 1206	RNCP1206FTD10K0CT-ND	Digikey	1	each	$ 0.10	4	$ 0.40
Resistor	RES SMD 100K OHM 0.1% 1/4W 1206	P100KBCCT-ND	Digikey	1	each	$ 0.54	3	$ 1.62
Resistor	RES SMD 100 OHM 0.1% 1/4W 1206	P100BCCT-ND	Digikey	1	each	$ 0.10	1	$ 0.10
Resistor	RES SMD 50 OHM 5% 2.4W 1206	541-2477-1-ND	Digikey	1	each	$ 0.59	3	$ 1.77
Resistor	RES SMD 5K OHM 0.1% 1/4W 1206	YAG5090CT-ND	Digikey	1	each	$ 0.10	1	$ 0.10
LED	LED GREEN CLEAR 1206 SMD	160-1404-1-ND	Digikey	1	each	$ 0.25	1	$ 0.25
Transistor	TRANS NPN 40V 0.2A TO-92	2N3904FS-ND	Digikey	1	each	$ 0.21	1	$ 0.21
Thyristor	SCR 0.8A 200V TO-92	2N5064CS-ND	Digikey	1	each	$ 0.62	1	$ 0.62
Jumper Wires	JUMPER WIRE M TO M 3" 28AWG	1528-1966-ND	Digikey	20	pack	$ 1.95	27	$ 2.63
Wire Connector	Socket Contact Gold 24-30 AWG Crimp	WM1128CT-ND	Digikey	2	each	$ 0.18	1	$ 0.18
Wire Connector	10CKT CRIMP RCPT HOU W/LOCKING	WM3341-ND	Digikey	1	each	$ 0.49	1	$ 0.49
Wire Connector	CONN HOUSING 2POS .100 W/LATCH	WM2900-ND	Digikey	1	each	$ 0.27	1	$ 0.27
Wire Connector	CONN SOCKET 24-30AWG CRIMP TIN	WM2562CT-ND	Digikey	1	each	$ 0.11	4	$ 0.44
Printed Circuit Board	Custom PCB for Power Distribution and Over-current Protection		OSH Park	3	set	$ 38.65	1	$ 12.88
Communication Electronics								
USB Hub	D-Link® DUB-H7 USB Hub, 7 Port	773207	Staples	1	each	$ 35.99	1	$ 35.99
UBS Port	Adapter Connector USB-B, Receptacle To USB-A, Receptacle	SAM8637-ND	Digikey	1	each	$ 8.74	1	$ 8.74
USB Cable	USB 2.0 Cable A Male to B Male 1.64' (500.0mm) Shielded	A128023-ND	Digikey	1	each	$ 8.28	1	$ 8.28
USB Cable	USB 2.0 Cable A Male to B Male 0.52' (160.0mm) Shielded	A142582-ND	Digikey	1	each	$ 5.77	1	$ 5.77
USB Cable	CABLE USB 2.0 A-MINI A M-M 1'	380-1427-ND	Digikey	1	each	$ 3.03	2	$ 6.06
USB Serial Converter	MOD USB SERIAL 5V EMBEDDED PCB	768-1017-ND	Digikey	1	each	$ 15.63	1	$ 15.63
USB Cable	Male A to Male B Usb Cable - 2m	WM17103-ND	Digikey	1	each	$ 3.28	1	$ 3.28
Microcontroller	Arduino MEGA2560 (ATMEGA2560)	1050-1018-ND	DigiKey	1	each	$ 38.50	1	$ 38.50
Driver	Adafruit MotorShield Kit V2.3	1528-1187-ND	DigiKey	1	each	$ 19.95	1	$ 19.95
Driver	CoolDrive® ONE Single Valve Driver	161D1X1K0	Nresearch	1	each	$ 19.50	3	$ 58.50
Fluidic Components								
Pump	Ismatec OEM REGLO ICC Digital Peristaltic Panel Mount Pump; 3-Channel, 8-Roller	EW-78001-45	Cole-Parmer	1	each	$ 1,809.00	1	$ 1,809.00
Valve	TitanEX™ 10 Position/11 Port With PCB (IDEX-HS; MLP778-606)	00420MV	Cole-Parmer	1	each	$ 983.18	1	$ 983.18
Valve	PEEK Manifold Assembly 5 Port, for 1/16" OD (IDEX-HS; P-154)	02023-10	Cole-Parmer	1	each	$ 104.40	1	$ 104.40
Valve	3-way Isolation Standard, 24VDC; 10-32 Porting	HP161T032	Nresearch	1	each	$ 73.48	3	$ 220.44
Tubing Connector	Peristaltic Pump Clips	EW-78016-98	Cole-Parmer	1	each	$ 58.00	3	$ 174.00
Tubing Connector	Two Piece Fitting Sets for 3-way Valves (set of 10)	10239109-10	Nresearch	10	pack	$ 31.09	9	$ 27.98
Tubing Connector	One-Piece Fingertight 10-32 Coned, for 1/16" OD (IDEX-HS; F-120X)	02013-41	Cole-Parmer	10	pack	$ 56.66	6	$ 34.00
Tubing Connector	Conical Adapter Assembly, for Rigid Tubing to Soft Tubing (IDEX-HS; P-794)	02014-54	Cole-Parmer	1	each	$ 19.80	6	$ 118.80
Tubing Connector	Flangeless Fitting Blue Delrin®, 1/4-28 Flat-Bottom, for1/16" OD (IDEX-HS; XP-206)	EW-00414-LW	Cole-Parmer	25	pack	$ 55.77	6	$ 13.38
Tubing	Ismatec SC0053T 3-Stop LMT-55 Tubing, 0.51mm ID, 12/pk	EW-97619-18	Cole-Parmer	12	pack	$ 88.40	3	$ 22.10
Tubing	Idex 1527L Chromatography Tubing, Natural FEP, 1/16" OD x 0.010" ID x 50 ft L	EW-02015-05	Cole-Parmer	50	feet	$ 113.00		$ -
Screws								
Screws	18-8 Stainless Steel Low-Profile Socket Head Screws; M3 x 0.5 mm Thread, 6 mm Long	92855A307	McMaster	25	pack	$ 5.75		$ -
Screws	18-8 Stainless Steel Low-Profile Socket Head Screws; M3 x 0.5 mm Thread, 10 mm Long	92855A310	McMaster	25	pack	$ 2.63		$ -
Screws	18-8 Stainless Steel Low-Profile Socket Head Screws; M3 x 0.5 mm Thread, 16 mm Long	92855A316	McMaster	25	pack	$ 3.20		$ -
Screws	18-8 Stainless Steel Low-Profile Socket Head Screws; M4 x 0.7 mm Thread, 16 mm Long	92855A416	McMaster	25	pack	$ 4.22		$ -
Screws	18-8 Stainless Steel Low-Profile Socket Head Screws; M5 x 0.8 mm Thread, 10 mm Long	92855A510	McMaster	50	pack	$ 12.72		$ -
Screws	Alloy Steel Low-Profile Socket Head Screw; Black Oxide, 2-56 Thread Size, 0.25" Long (2Switch)	92220A311	McMaster	10	pack	$ 14.80		$ -
Screws	Alloy Steel Low-Profile Socket Head Screw; Black-Oxide, 4-40 Thread Size, 1/2" Long (MSwitch)	92220A123	McMaster	10	pack	$ 7.93		$ -
Screws	Passivated 18-8 Stainless Steel Pan Head Phillips Screws; M2.5 x 0.45mm Thread, 10mm Long	92000A106	McMaster	100	pack	$ 4.03		$ -
Nut	High-Strength Steel Hex Nut; Class 10, M3 x 0.5 mm Thread	90685A037	McMaster	25	pack	$ 8.49		$ -
Nut	High-Strength Steel Hex Nut; Class 10, M4 x 0.7 mm Thread	90685A039	McMaster	100	pack	$ 9.68		$ -
Nut	Zinc-Plated Steel Hex Nut; Medium-Strength, Class 8, M2.5 x 0.45 mm Thread	90591A270	McMaster	100	pack	$ 2.22		$ -
Bracket	Zinc-Plated Steel Corner Bracket, 7/8" x 7/8" x 5/8"	1556A24	McMaster	1	each	$ 0.43	11	$ 4.73
Standoff	Female Threaded Hex Standoff; 18-8 Stainless Steel, 10mm Hex, 16mm Long, M4 x 0.7mm Thread	94868A631	McMaster	1	each	$ 2.09	8	$ 16.72
Standoff	Rubber Bumper with Unthreaded Hole	9540K743	McMaster	10	pack	$ 6.93		$ -
PML Fluidic Chip								
Chip Holder	Fluidic Connect PRO Chip Holder with 4515 Inserts	FC_PRO_CH4515	Micronit	1	each	$ 1,530.00	1	$ 1,530.00
Ferrules	5 Fluidic PRO Ferrules	FC_PRO_FFKM_KIT.05	Micronit	5	pack	$ 113.00	6	$ 135.60
Debubbler	Debubbler		DarwinMicrofluidics	1	each	$ 149.00	3	$ 447.00
Chip	Fluidic Chip for Spheroid Culture and Interrogation	FP-3W	PMLab/Bio-Vitro					
In-House Fabrication								
Acrylic	Clear Scratch- and UV-Resistant Cast Acrylic Sheet; 12" x 24" x 1/4"	8560K355	McMaster	1	each	$ 29.77		

APPENDIX A7. VIDEO OF AUTOMATED PROTOCOL

Download Here:

https://miami.box.com/s/ph9rj6t3aouf8yjqq6hjqi7pj127ja38

APPENDIX A8. ENGINEERING DRAWINGS OF CHIP DESIGNS

Chip v01 (Acry-Chip)

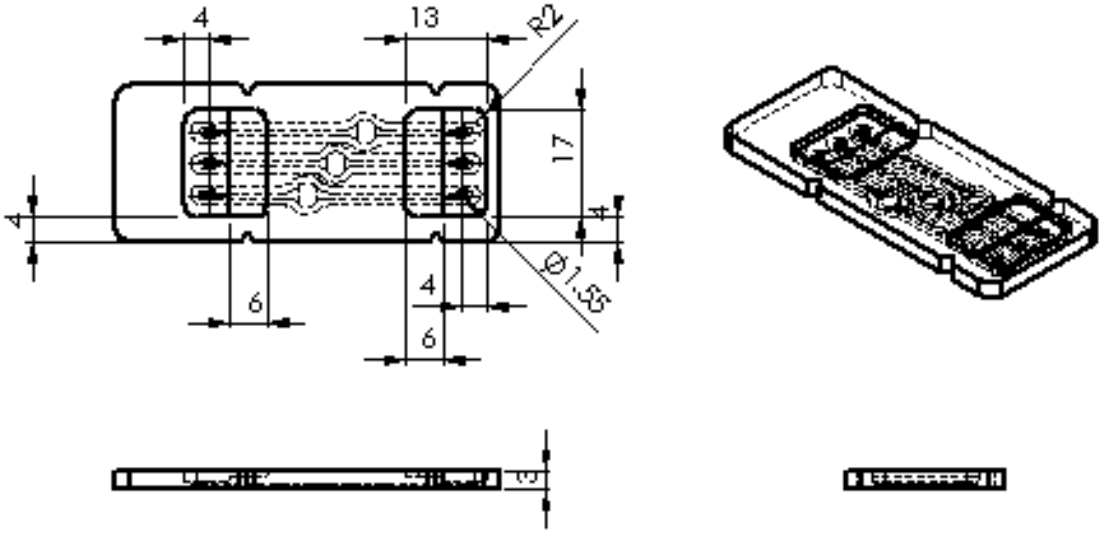

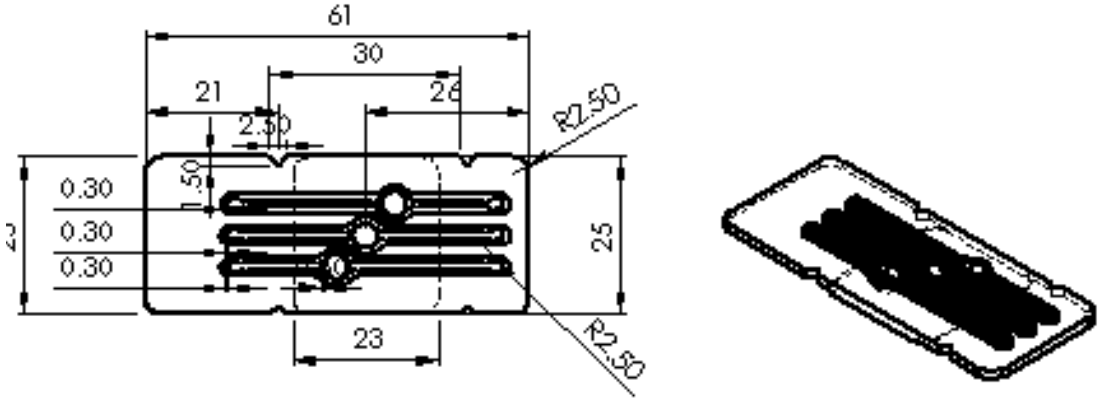

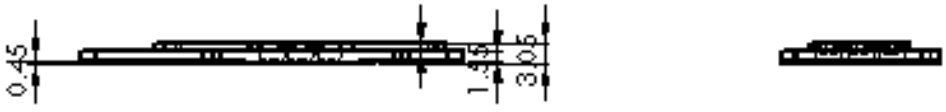

Chip v02 (Oxy-Chip): Bottom

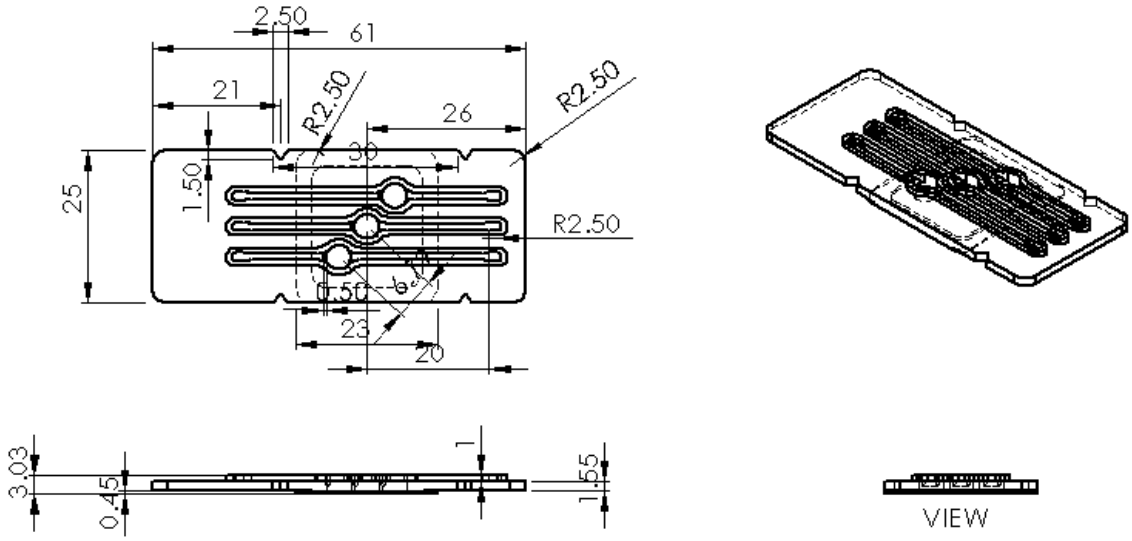

Chip v03 (Membrane Chip)